ABSTRACT

Title of Dissertation:	3D-PRINTED POLYSTYRENE FOR CELL CULTURE
	Max Jonah Lerman Doctor of Philosophy, 2019
Dissertation directed by:	Fischell Family Distinguished Professor & Department Chair John P. Fisher, Fischell Department of Bioengineering Department of Materials Science and Engineering

Efficient methods to expand stem cells *ex vivo* hold significant promise in many clinical applications. For example, hematological malignancies account for nearly 10% of cancer related deaths in the United States of America and frequently require a transplant to successfully treat the disease. *Ex vivo* expanded hematopoietic stem cells (HSCs) could help narrow treatment gaps; however, generating viable dosages of HSCs currently fall short of expectations with difficulties in expanding HSCs and the loss of cellular multipotency. Coculture with mesenchymal stem cells (MSCs) aims to provide the necessary intercellular signaling to counteract monoculture deficiencies. Typically, achieving these and other clinical goals have relied on 2D polystyrene (PS) as the

fundamental substrate for cell culture. With the emergence of 3D printing, improved biomimicry with 3D culture models are becoming widely available. In this dissertation, we develop a 3D PS culture substrate for adherent and non-adherent cells, working towards a model for the bone marrow niche. To achieve this goal, the objectives of the work were to: (1) develop a 3D printing method for PS and surface functionalization strategy to facilitate extracellular matrix protein and MSC adhesion, (2) assess the effects of the underlying surface functionality on osteogenic differentiation under static and dynamic conditions, and (3) validate the culture model successfully cultures multiple cell types with a model non-adherent cell line, demonstrating validity and translatability as a bone marrow niche model. In converting PS from a 2D culture platform to a 3D printed one, we take steps to increase the biomimicry of *in vitro* cell culture without sacrificing fundamental PS properties (e.g. optical clarity, cost-effectiveness, disposability). Continued development and of the model would see an efficient method for studying the complex bone marrow niche with applications in pharmacology and cancer diagnostics.

3D-PRINTED POLYSTYRENE FOR CELL CULTURE

by

Max Jonah Lerman

Dissertation submitted to the Faculty of the Graduate School of the
University of Maryland, College Park, in partial fulfillment
of the requirements for the degree of
Doctor of Philosophy
2019

Advisory Committee:
Professor John P. Fisher, Chair
Dr. Greg Gillen, Co-chair
Professor Robert Briber
Associate Professor Isabel Lloyd
Associate Professor Helim Aranda-Espinoza
Associate Professor John Cumings, Dean's Representative

Acknowledgements

I would like to thank my advisors, Dr. John P. Fisher and Dr. Greg Gillen. Thank you for the mentorship, guidance, and opportunity to work collaboratively between the Tissue Engineering and Biomaterials Lab and the National Institute of Standards and Technology. My appreciation goes out to my committee: your suggestions and guidance helped to improve this work and its ultimate presentation. To my lab mates and friends in the Department of Materials Science and Engineering and Fischell Department of Bioengineering: thank you for helping to make this a success and forcing me to laugh and learn along the way. Thank you to the undergraduates who helped with this work, particularly Anthony Chiu, James Fookes, Anushka Gerald, and Maddie Golding. Thank you, Mom, Dad, Barbara, and Henry. Your support and encouragement helped all this become a reality. Lastly, and certainly not least, thank you Paulina. There are no words for my debt of gratitude for all you have done, continue to do, and will do to ensure everything will just be OK.

Table of Contents

List of Tables

List of Figures

Chapter 1: Introduction to Stem Cells Culture and Clinical Motivation

As of 2014, leukemia and non-Hodgkin lymphoma represent two of the top ten leading causes of cancer-related deaths in the United States of America.[1] Patients suffering from these and other hematological malignancies often undergo treatment with a transplant based therapy, provided a satisfactorily matched donor is found. Both human mesenchymal stem cells (hMSCs) and hematopoietic stem cells (HSCs) have clinical applications in treating hematological cancers.[2,3] However, these cells are scarce in donated tissues: hMSCs are estimated to account for up to 0.01% of the cells isolated from bone marrow[4] and approximately 10^7 HSCs are present in a unit of umbilical cord blood[5]. However, to successfully transplant these cell populations, often at least 10^6 cells/kg of body weight are needed, potentially relegating traditional umbilical cord blood or bone marrow donations to young people.[6,7] Additionally, these potentially life-saving therapies often remain out of reach for patients of non-European ancestry, who may have as low as a 1% chance of finding an ideal donor.[8] To achieve clinical and research objectives, these cells may require expansion *ex vivo*.[9] Treatment of hematological disorders could serve with an efficient means of expanding cell populations *ex vivo*, potentially eliminating the need for perfectly matched donors or facilitating autologous donation, providing access to life changing therapies to people of all ages and races.

More than 1000 active clinical trials and thousands of published papers on the tissue engineering potential of hMSCs and HSCs demonstrates the active interest in these

populations.[10] Where hMSCs can differentiate into cells across the mesoderm (e.g. cartilage, fat, and bone)[11] and HSCs support hematopoiesis,[12] together they interact within the bone marrow niche to facilitate regenerating tissues.[13] The coculture of hMSCs and HSCs likely increases the functionality and number of HSCs by providing necessary intercellular signaling.[5,14] Without the proper signaling, HSCs lose their self-renewal characteristics, diminishing their clinical applicability.[15–17] As well, co-transplantation of hMSCs and HSCs may aid in preventing graft versus host disease by modulating host immune response and promoting transplant engraftment.[18] A significant need exists to develop hMSC and HSC based therapies to combat cancer incidence. However, expanding these populations *ex vivo* remains difficult, limiting their applicability as a clinical therapy.[15] Development of these and other cell based therapies necessitates an efficient mechanism for *ex vivo* expansion and tissue modeling.

To better understand the intricate functioning of these, and other, cell environments, researchers turn to tissue models. These provide a mechanism to investigate complex biological functions without the need of live subjects. Increasing the complexity of these culture models, such as moving from 2D to 3D, has been shown to better match results found *in vivo*.[19] In this dissertation, we propose a 3D-printed, plasma treated, polystyrene (PS) scaffold to increase the biomimicry of this universal culture material and work towards developing a meaningful model of the bone marrow niche. Ultimately, the goal and continued pursuit of this project seeks to better understand the HSC-MSC relationship with methods of controlling expansion, differentiation, and intercellular signaling. The use of enabling technologies, like 3D printing, aim to provide better

mechanisms to research complex biological interactions and increase the clinical relevance of discoveries.[20] As a non-adherent cell, HSCs are believed to migrate through the bone marrow niche, but spend some time sequestered in the vicinity of hMSCs.[21] A culture method, particularly a bioreactor, which can support both actively circulating and targeted localization of HSCs may best facilitate their long-term viability. However, surface chemistry and shear stress on bioreactor scaffolds must be considered to prevent adherent hMSCs undergoing unwanted phenotypic shifting (e.g. osteogenesis).[22,23] This dissertation investigates these competing mechanisms which lead to the bone marrow niche development, leading toward a functional research model.

The improvements discussed in this dissertation seek to build on the universality of 2D tissue culture polystyrene (TCPS) as an effective culture substrate. TCPS is widely accepted for cell culture and adhesion to TCPS is included as a criterion for identifying hMSCs.[24] TCPS utilize a highly oxidized surface, aiding in the adhesion of cells and proteins, to build a culture environment where a variety of cells can thrive.[25] (The evolution of PS as a culture substrate is more thoroughly discussed in Chapter 2). Investigating the impact of specific surface chemistries on adhesion morphology and expansion of hMSCs aids in determining a means to control hMSC differentiation and facilitate long term hMSC *in vitro* culture for clinical applications or to support HSCs.[5,11]

Building further biological relevance is gained by transforming from a 2D to a 3D construct. (Chapter 3 details 3D printing approaches for cell culture and medical applications). For hMSCs, a 3D printed construct need not replicate the exact bone

geometry. Various designs have been investigated, where modeling the interactions of the numerous cells populations in the bone marrow environment and being able to observe the interactions is the primary objective.[26] Additionally, placing these models under flow and using computational modeling to interrogate multiple geometries rapidly can evaluate shear stress characteristics.[27,28] Bioreactors containing 3D printed, cell-laden, scaffolds provide a means to expand clinically relevant numbers of cells by creating dense culture volumes (growth surface area/total scaffold volume), efficiently exchanging nutrients, and providing biomimetic shear stress.[29–31] Bioreactor technologies are widely used to model hMSC proliferation, differentiation, and to investigate their applicability in tissue engineering and regenerative medicine.[22,32] A combination tubular perfusion bioreactor with computationally designed, 3D printed scaffold is utilized to control flow rate and shear stress experienced by the adherent cell population, thereby creating a self-contained platform for cell growth.[33] Utilizing this dynamic environment for a mechanically sensitive population, like hMSCs, lends itself well to investigating cell growth mechanisms and increasing population sizes[34] and directing differentiation.[35] The potential exists to revolutionize cell culture and move away from the standard 2D approach, even fabricating geometry tailored to specific cell environments.[36]

This dissertation aims to transition PS from the ubiquitous 2D culture material of the past half century, to a more biologically relevant 3D construct, with an eye on expanding cell populations for hematological malignancies. First, we sought to understand how the surface properties impact the adhered proteins and ultimately the adhered cell population. Then we looked at transforming the culture substrate from 2D, to 3D, to a 3D dynamic

culture environment. Over the course of this work, we investigated how our functionalization method translated from 2D to 3D, to ensure no loss of desired cell outcomes occurred when moving to 3D. Ultimately, this dissertation sought to build a bone marrow niche model where multiple cell populations could be simultaneously investigated and easily separated, allowing rapid and easy isolation and visualization of the confined populations. Specifically, the aims of the work are:

1) Develop a 3D printing method for PS which preserves known 2D surface properties
    a. Characterize the surface properties of plasma treated PS and protein interactions with the surface
    b. Characterize hMSC response to the treated surfaces to demonstrate expected interaction with the treated surfaces
    c. Utilize the treatment platform to functionalize PS for 3D culture
2) Use surface functionalization strategies and 3D printing to direct hMSC response and direct interactions with non-adherent cells
    a. Develop a means to enhance osteogenic differentiation on the 3D printed construct
    b. Translate the 3D scaffold approach to a bioreactor model for hMSC expansion and demonstrate extended culture without osteogenic differentiation
    c. Demonstrate the viability of culture system for coculture with a model non-adherent cell population

In this dissertation, we have successfully used 3D printing and plasma functionalization to direct hMSC response, a step towards making 3D culture a widely accepted practice. As well, the presented 3D culture approach easy integrates with dynamic culture. We demonstrate the developed culture system is well suited for use with these interrelated and complex culture influences. By moving away from 2D models, we seek to improve the biomimicry of the culture system while using a well-studied and accepted culture substrate to investigate hMSC response. Further development of the culture approach could see a cost effective, self-contained expansion culture system for autologous HSC transplant using MSCs as a feeder-cell source, working to bring needed therapeutics to patients globally and provide realistic avenues for clinical, diagnostic, and implantable cell populations.

Chapter 2: The Evolution of Polystyrene as a Cell Culture Material[i]

This chapter discusses the development of PS as the modern universal culture substrate. The development of the material, transition to culture, and approaches to improving the culture material are discussed. PS has largely become the culture material of choice, though its widespread adoption took significant time. Several methods to functionalize the culture surface and manufacture growth substrates are surveyed. This chapter concludes with a description of the next steps for stable PS culture surfaces and specific means to target cells, suggesting a need to improve the culture surface whether through targeted surface functionalization or improved biomimicry in the culture geometry.

2.1 Introduction: How PS became the Basis of in vitro *Cell Culture*

Polystyrene (PS) has served as the fundamental substrate for adherent animal and human cell culture for more than 50 years.[37] Due to its optical clarity, relative ease of manufacture, and low production cost, PS has largely replaced glass for cell-based work,[25,38] while glass remains the choice for imaging due to its lower refractive index.[39] On the other hand, mass-production of PS through injection molding has produced a low-cost, high-culture volume, alternative to glass which is compatible with many cell strains and contrast agents. All these reasons have driven 2D tissue culture polystyrene (TCPS) to become the basic platform for adherent cell culture.

[i] Adapted and reprinted with permission from: MJ Lerman, J Lembong, S Muramoto, G Gillen, and JP Fisher. The Evolution of Polystyrene as a Cell Culture Material. Tissue Engineering Part B: Reviews. 24, 2018, (359).

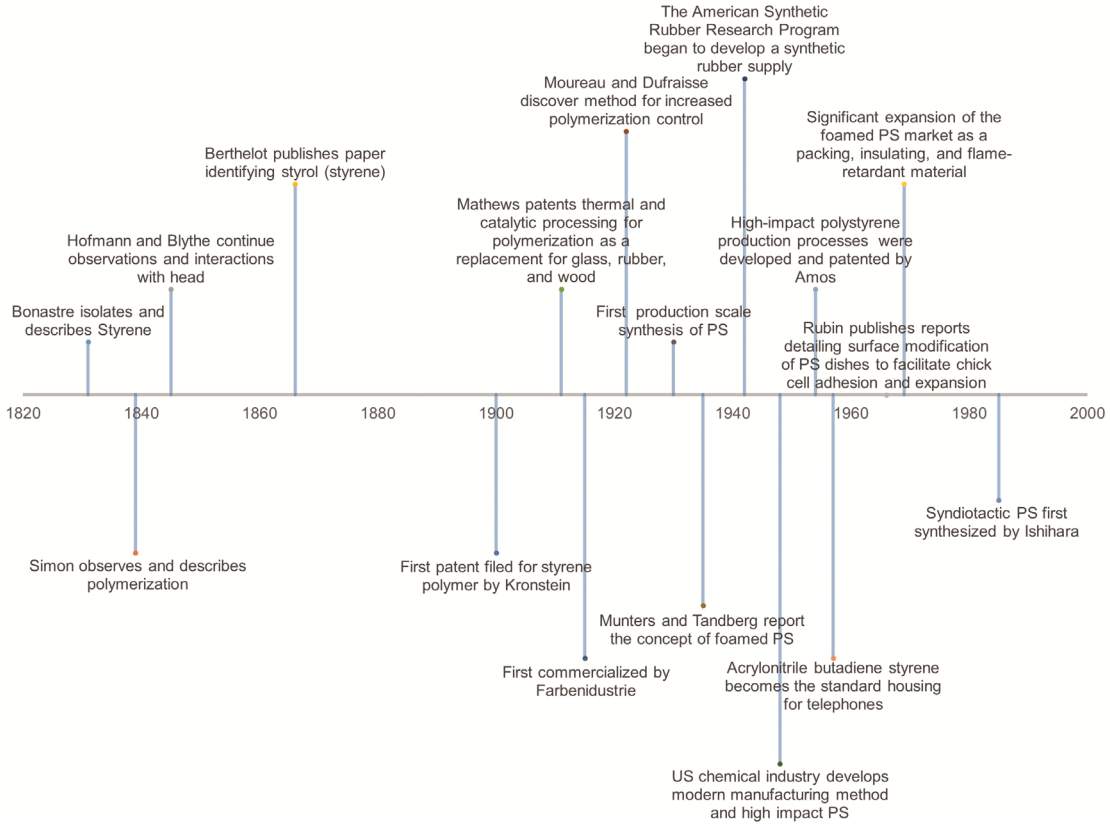

Figure 2.1 Timeline summarizing major developments of PS, from the initial discovery to custom compounded polymers. Major development of the plastic occurred during and after World War II with the need for a consistent synthetic rubber supply. PS has played a pivotal role in many industries, with nearly 200 years of research attributed to this single material.

PS development began in the 1830s with the discovery of styrene and the first documented observations of polymerization (Figure 2.1).[40,41] Development of styrene containing polymers continued, with major advances occurring along with the advent of large-scale plastics processing, spurred by World War II.[41,42] Modern applications bridge multiple industrial areas from cell culture to synthetic rubber, with material development constantly on-going. Modern applications for PS harness the inherent material properties, largely as highly recyclable injection molded or thermoformed plastic, to achieve consumer and research goals.[40,43] With a second-order glass transition temperature near the boiling point of water (95 °C - 105 °C, with some molecular weight dependence),[44–47]the formability of the material eases manufacturing constraints, both as a compounded and pure material. The use of PS in bio-manufacturing and cell-based research activities as an injection molded, embossed, cast, electrospun and, more recently, 3D printed polymer can all be attributed to the business drive to mass-produce culture plastics and move away from glass. However, the simple homopolymer lacks appropriate surface chemistry for cellular recognition: phenyl groups do not readily provide anchoring points for cells (Figure 2.2).[37] This has dictated the need to modify and develop PS-based surfaces to facilitate cell anchorage *in vitro* by incorporating surface functionality which cells will bind to and grow on, a major theme of this chapter.

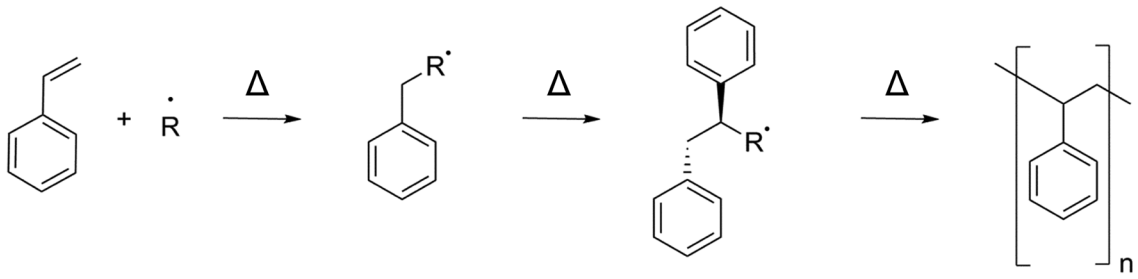

Figure 2.2 The free-radical polymerization process for PS synthesis. The free-radical incorporates into the styrene monomer and continues to increase the polymer length by breaking the *pi-pi* on the vinyl group, forming a new *sigma* bond.

Five decades of 2D PS spearheading *in vitro* cell culture approaches has built a foundation of knowledge, understanding mechanisms to expand cells generally. This chapter focuses on the basics of 2D culture platforms and emerging 3D PS approaches researchers are embracing for cell culture, summarizing the mechanisms to transform PS surfaces to facilitate cell adhesion, growth, and *in vitro* expansion. We discuss the liquid, plasma, and next generation treatment methods used to alter PS surfaces to improve cell growth and how these methods allow for the incorporation of moieties containing oxygen and nitrogen, thereby presenting surface chemistry for cells to anchor and grow. As the importance of 3D surfaces is becoming widely accepted, we dive into the role 3D PS fabricated through casting, electrospinning, and 3D printing seeks to increase our understanding of cell growth *in vitro* and how the complex growth platforms can better replicate *in vivo* environments. As well, we present a focus on PS microbeads, and the void they fill as a suspended-adherent growth substrate. Overall, this chapter details the approaches garnered for PS as both a basic and targeted growth substrate.

2.2 2D PS: The Basis of in vitro *Cell Culture*

Fabricating mass-produced flat and finely topographically detailed 2D tissue culture surfaces both employ the same basic technologies: casting, embossing, or molding. With the fewest technical and equipment challenges, industrial scale injection molding has served to fabricate parts with features traditionally at the hundreds of micron scale and above, where improvements continue to push these boundaries.[48,49] Since the 1970s, injection molded PS, followed by an oxygen plasma treatment, has remained the most prolific method for manufacturing TCPS culture surfaces.[50] However, custom in-house injection molding equipment is generally unavailable to research groups and mass-

produced TCPS may not possess surface characteristics of interest. This is not to say lab-bench embossing is out of reach. Imprinting fine channels, through holes, and other microfluidic features have been demonstrated for cell-based assays, though it may require a fifteen-ton hydraulic press with heating plates capable of reaching 125 °C.[51] Such equipment may aide in embossing PS surfaces, but is not necessary to achieve anisotropic surface behavior. Using a silicon template, nanoimprinting has been used to align osteoblasts, finding that deeper grooves improved cell alignment along the channels, and increased migration rate along 150 nm grooves by a factor of 1.46.[52–55] Hot embossing has been used to create many fine features, including pillars, grooves, and microwells, which successfully spatially segregated cells by patterning the surface chemistry and topography.[56] As well, micropattern width has been seen to influence differentiation of human mesenchymal stem cells to vascular smooth muscle cells, where finer widths aid in cell alignment.[57] As the cells adhere to the micropattern, internal mechanical stresses likely act to differentiate the cell, working to match features to function.[58,59] However, while sequestering the cells with microchannels may be beneficial to guide cells, the reduction in cell spreading and change in morphology may also generate genetic abnormalities (such as forming micronuclei),[60,61] making cell culture platforms with relevant length scales larger than the cells still more desirable. With this quality in mind, casting and embossing remain two of the more reproducible means to produce PS parts, especially on the industrial scale with injection molding equipment, and remain the method of choice for consumer and industrial parts. The major drawback to casting is the prohibitive cost of the tooling and equipment, limiting the most practical uses to large volume part production. On the lab bench, the lack of specialized tooling or standardized

technique can result in poor part resolution and high cycle times. Other fabrication methods, such as electrospinning and 3D printing, provide alternate ways to achieve resolution that cannot be accomplished by casting and embossing with the advantage of developing complex 3D structures. Following fabrication, PS must be surface treated to facilitate cell adhesion. Over time, these approaches have evolved and are discussed next.

2.3 The Transformation of PS to TCPS

With respect to *in vitro* cell growth, biocompatible surfaces need to incite cell adhesion, spreading, and potentially induce differential cell function, based on the application. To facilitate cell adhesion, the PS surfaces are functionalized to introduce biologically relevant chemistry (e.g. carbonyl, amine groups). Transforming native PS surfaces to include chemistry other than phenyl groups can increase the hydrophilicity and surface charge, modulating the deposition of extracellular matrix, cells, and proteins.[62–64] The complex mechanisms for cell deposition in *in vitro* models warrants further investigation, potentially developing a means to develop custom growth surfaces, therefore promoting large expansion of cells. As researchers seek to develop active linking mechanisms, growth surfaces functionality continues to evolve, sequestering specific cell types and using material properties to modulate adhesion.

Functionalization methods can be broadly divided into two groups: liquid phase and plasma-based treatments. Liquid treatments provide an easy avenue to treat large surfaces quickly, but the functionality gained is often limited to surface oxidation and often requires highly corrosive substances. Plasma functionalization, most commonly used to manufacture TCPS in bulk, broadens the surface chemistries achievable, but requires

ionizing energy to modify the surface (which can pose some safety concerns as well). Emerging surface modification techniques provide targeted cell interaction mechanisms, by grafting specific binding regimes such as DNA and proteins but may have long-term stability issues and higher costs limiting their broad appeal. Discussion of each of these techniques, along with treatment fluid choices will address mechanisms for depositing specific chemistry, modulating contact angle, and roughening surfaces to facilitate cell adhesion, extracellular matrix deposition, and cell expansion.

2.3.1 Surface Functionalization: Liquid Treatment

The first proposed mechanism for modifying the surface of PS to facilitate cell adhesion was introduced in 1966 by sulfonating the surface, with subsequent neutralization with sodium carbonate and water (Figure 2.3).[37] By the mid-1970s, the mass-produced TCPS dishes accepted today and were becoming abundant in research with much interest in optimizing and upgrading the surfaces towards a general cell culture surface.[65–67] Surface oxidation with strong acids began and continued to be used. Sulfuric acid treatment (20% v/v) not only aids in cell binding, but can potentially facilitate adhesion of proteins, such as fibronectin and vitronectin.[68] The deposition of these proteins can mediate cell adhesion, spreading, and growth, primarily due to the surface receptors on cells present to bind certain proteins and act as adhesive agents.[62,69] Other acids (e.g. nitric, hydrochloric) may show these benefits as well, but may tend to degrade surfaces, reducing the optical clarity.[68]

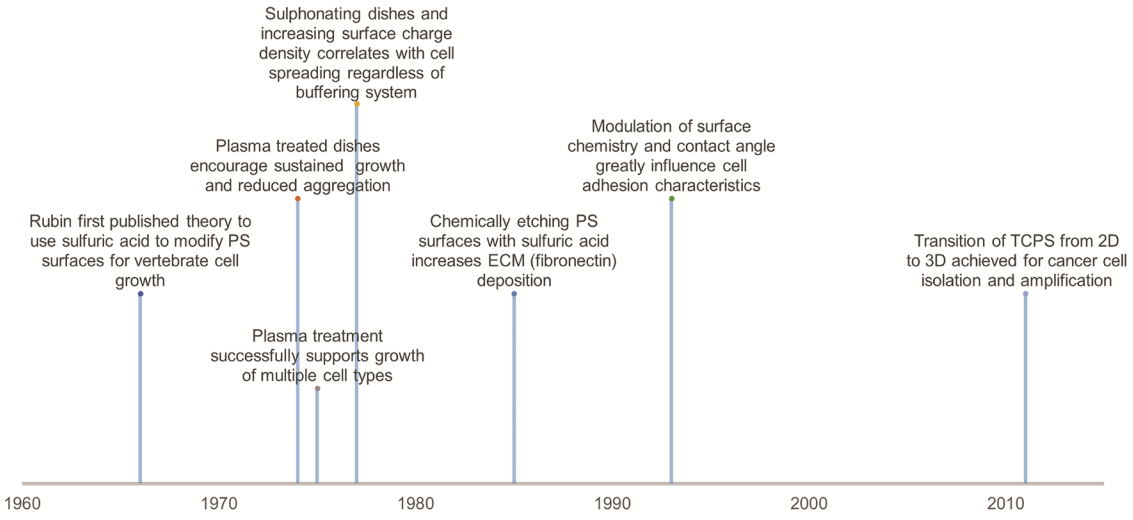

Figure 2.3 A brief history of the progression of TCPS. Initial papers described significant advances in PS as a culture material, with the basis for culture techniques largely occurring in the 1960s-1970s.

Although working with concentrated acids may not be desirable in a laboratory setting due to inherent safety concerns, safer liquid coatings are not preferable for creating uniform, stable, and permanent functional changes to the growth surfaces. For example, simulated body fluids can be used to facilitate growth of hydroxyapatite crystals on PS surfaces, with the goal of inducing osteogenic differentiation of mesenchymal stem cells.[70] However, the surface density can be difficult to control, and they can be easily removed from the surface with applied force. As well, a protein coating or plasma activated PS surface is required to deposit acidic residues and coordinate nucleation of hydroxyapatite crystals.[71] Stable functional changes to the surface thus requires modification of surface chemistry using treatments that can enable oxidation or form stable covalent bonds. Full liquid immersion provides a technically direct method to introduce a number of surface chemistries (e.g. $-CH_3$, $-NH_2$, -SH, -OH, -COOH) by selecting modifying liquids.[72] Although this method may erode complex surfaces and printed geometry during modification, complete internal surface coverage is ensured. However, the use of plasma to enhance cell-adhesion surface chemistry has become the convention for mass 2D TCPS production and remains popular in academic research. Liquid functionalization methods may reduce the optical clarity of surfaces, where plasma-based methods maintain translucency and provides chemical functionalization flexibility relatively easily.

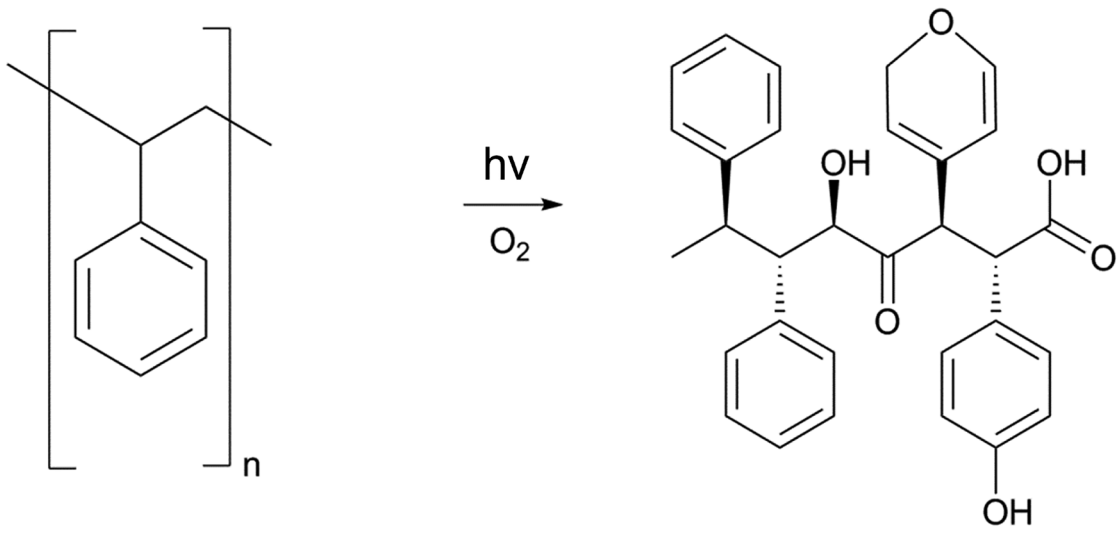

Figure 2.4 An example reaction demonstrating how oxygen can incorporate into polystyrene following a plasma treatment. The high potential of the reactive oxygen ions may break phenyl rings, or replace functional groups, changing the surface properties.

2.3.2 Surface Functionalization: Plasma Treatment

Plasma surface modification occurs as current is passed across a gas, creating ionized species. Energetic ions may interact with the presented surfaces and incorporate or provide further functionality. Modifying the source gas effectively modifies the plasma composition and surface chemistry (Figure 2.4).[73] Plasma treatment, along with reactive ions, can produce electrons, free radicals, metastable species, UV light, and heat, all of which can work to deposit, etch or chemically modify the surface of interest.[74] The Falcon Plastics Company accidentally discovered the benefit of plasma treating PS for cell culture while attempting to prepare the surface for glass coating, however; it was found that the oxygen containing plasma efficiently oxidized the surface and facilitated cell adhesion, ultimately leading to the preparation method for TCPS still used to this day.[25] Early development of this approach looked at using glow discharge in vacuum and evaluating its effect on a number of cell types, where it was found that the surface treatment increased cell spreading and growth rates compared to untreated surfaces.[66] Native PS surfaces are associated with early growth rate plateauing, likely due to reduced metabolic activity for self-adhered populations.[65] Additionally, the negative surface charge encourages non-specific surface absorption of serum proteins contained within the media, potentially mediating cell adhesion.[65] There remains a number of confounding factors which make direct correlation of surface chemistry and cell interaction difficult, as surface charge, surface strain, media formulation, and cell type can all influence cell adhesion to surfaces. Even with these limitations, however; researchers have evaluated many excitation and functionalization gas combinations that have led to successful modification of PS surfaces.

Table 2.1 Plasma effects on PS. Significant work has been performed to understand the link between surface chemistry and cellular response. It is difficult to state a unifying theory for all cell types, however; providing surface chemistry with a high degree of biomimicry (e.g. carbonyl, carboxyl, amine) appears to improve cellular response during *in vitro* culture.

Plasma	Surface Chemistry	Cellular Impact	Refs.
Air	C1s 86.2% O1s 12.0% N1s 1.8%	Facilitated attachment under rotary conditions of L929 Mouse Fibroblasts	[75]
Ammonia (Low Pressure)	C1s 65% O1s 5% N1s 9.4%	Increased viability of human mesenchymal stem cells (122.7% increase in metabolic activity), human dermal microvascular endothelial cells (150.4% increase in metabolic activity) as compared to TCPS	[76]
Acrylic Acid (Low Pressure)	C1s 39.6% O1s 31.8% C=O 17.0%	Similar metabolic activity as compared to TCPS	[76]
Carbon Dioxide (Low Pressure)	C1s 70% O1s 12.3%	Reduced enzymatic activity vs TCPS (86.9%)	[76]
Argon (Low Pressure)	Not Specified	Mouse Fibroblasts founds to have peak attachment density with short (<10 seconds) treatment times, and no difference between 10-30 seconds	[63]
Acetone, Methane, Methanol, Formic Acid, and Oxygen	Varied	Hydroxyl groups do not correlate with cell growth of bovine aortic endothelial cells (R^2 = 7.6%), carbonyl groups correlate better (R^2 = 57%) Human umbilical veil endothelial cells found to adhere and grow on PS only with higher than 17.7% oxygen content, matching TCPS	[77]
Nitrogen or Ammonia (10%), Argon or Helium (Balance)	91% C1s 9% O1s or N1s	Find greatest cell attachment efficiency BCP-K1 cells with both ammonia and nitrogen dopant gasses using helium plasmas. Greatest proliferation found for nitrogen/helium and ammonia/argon plasma treated surfaces	[78]
Ultraviolet Ozone	O1s 36% Find washing with water reduced the surface oxygen.	Chinese Hamster Ovary cells. See more than 80% of seeded cells attach under 3-hour incubation under three minutes of surface treatment, better than TCPS	[79]
Ammonia	Varied	High cell affinity of human fibroblasts onto PS surfaces. Good amination of the surfaces with 15-20% of the total nitrogen content detected on the surfaces, with total amines presented increasing with increasing plasma intensity.	[80]

The composition of the process gas and the plasma source configuration used to carry out plasma modification dictate the ultimate surface chemistry (Table 2.1), with gas combinations usually determined by the vacuum system chosen, power supply, level of purity required, and gases obtainable. The majority of research has involved modifying surfaces to incorporate oxygen and nitrogen containing species, with the objective of creating surface chemistry that encourages cell adhesion, proliferation, and functionality.[75,76] Several studies have shown that increased plasma treatment time led to a higher oxygen concentration on the surface (i.e., increased wettability),[81,82] but this alone was not a very strong determinant for cell adhesion and spreading.[83] Interestingly, hydrophilic surfaces that displayed water contact angles between 40° and 60° appear to facilitate *in vitro* cell adhesion for human umbilical cord vein endothelial cells (HuVEC) and HeLa cells,[84] with the incorporation of carbonyl groups demonstrating the best adhesion characteristics.[63] The breadth of process gases investigated, including a selection of organic compounds (e.g. acetone, methane, methanol, and formic acid) incorporated into an oxygen plasma have revealed some correlation between surface chemistry and cell adhesion rates.[77] However, the mechanism of cell adhesion is a complex process, and variables are difficult to isolate. It is believed that the contributions other than surface chemistry are playing important roles in *in vitro* cell adhesion, for example the bulk polymer chemistry and presence of organic molecules[77] such as extracellular matrix proteins and serum components that may be inherently present in cell cultures.[78]

The absence of clear trends indicates numerous pathways for cell adhesion and spreading, and the selection of chemistries incorporated on the surface (e.g. carbonyl, hydroxyl, or carboxyl) may be necessary but insufficient for *in vitro* cell growth. For instance, one mechanism may require matrix proteins to absorb first through the interaction with the surface which in turn allows cells to anchor down.[77,85] One example of this phenomenon is thought to be initiated through the binding of extracellular matrix to a plasma-deposited amine surface, which then regulated the interaction and subsequent attachment of human mesenchymal stem cells.[78] Though the mechanism remains unclear, cells may better recognize randomly adsorbed and often denatured proteins on plastic surfaces than the surface chemistry provided by plasma treatment, allowing cells to modify the surfaces and deposit their own extracellular matrix.[86]

An interesting effect of plasma treatment is the interaction of gas-phase ions with the PS surface, which has been reported to influence more than just the final surface chemistry. Plasma ion implantation and incorporation of free electrons can induce charging on the surface,[87,88] which may influence efficiency and extent of cell adhesion and spreading. This may also influence the type of serum proteins that absorb to the surface, which may subsequently regulate the type of cells that attach.[64,67] In addition to the ion interaction with the surface, it has been demonstrated that the length of time the surface is exposed to the plasma, as well as the power applied, can have a significant effect on the surface chemistry and topography. For example, longer treatment times are associated with lower contact angles and higher surface free energy due to the attachment of oxygenated functional groups and breakdown of phenyl groups,[83] which may be facilitating cell

adhesion through enhanced oxygen or electron incorporation on the surface.[89,90] As well, increasing the plasma source power tends to create more complex surface chemistry owing to the kinetic energy available for increased bond breaking and formation.[55] The increased voltage can be accompanied by roughened the surfaces, which have been shown to increase cell attachment, growth, and viability.[91–93]

Native PS surfaces are considered smooth (root-mean-square roughness of approximately 1.7 nm).[79] Plasma treatment tends to break substrate surface bonds and induce surface roughening.[94] Ultraviolet ozone exposure has been shown to leave surface pillars between (20 - 400) nm tall,[79] which can possibly influence focal adhesion location and spreading.[95] Surface wrinkling has also been observed with scanning electron microscopy and atomic force microscopy, with surface roughness generally increasing with increased energetic source exposure time.[94] Additionally, exposing these polymer surfaces to energetic plasmas could act to degrade the surface, depending on plasma energy and exposure time, and could potentially impact overall mechanical properties of the surface or bulk.[96] Aside from disrupting the otherwise pristine surfaces, the potential advantages of plasma treatment may be tempered by the longevity of treatments. Atmosphere or water exposure has caused some prepared samples to deteriorate over time (potentially removing up to half of the bioactive residues), necessitating sample storage under non-reactive gasses (e.g. Argon) prior to use.[97] Though the functionality on the surface is preserved, shelf stability is necessary to appeal to a mass-production environment. Oxygenated surfaces appear to be the exception, as samples have been shown to maintain surface chemistry for more than a year.[77]

In cases where site-specific surface modification is required, plasma jets can be directed through a shadow mask[98,99] or surfaces can be patterned with photoresist resin[100] to provide distinct regions for surface modification. Another approach is to use focused plasma treatment from a dielectric barrier discharge jet, by confining the jet with glass capillaries as small as 100 μm in diameter, modifying regions up to 1.5 mm in diameter, even when using atmospheric low-flow-rate plasma.[101] This approach effectively localizes cell growth, which is beneficial for isolating and patterning cell populations.[102] The area modified by the plasma beam is not limited to the size of the striking plasma jet, as reactive species follow the gas flow profile away from the impingement point and modify the PS surface for some distance. Given these limitations, oxygen plasma has been used to route and pattern cell constructs, localizing cell adherence.[103,104] Further effective means of localizing plasma treatment for cell culture requires modifying the characteristics or geometry of the substrate. For example, treating 3D objects in a layer-by-layer fashion or treating fully fabricated objects at the completion of fabrication could both effectively modify complex objects and deposit custom surface chemistry.

Treating 3D objects with plasma remains a challenge. It is established that the initial exposure to plasma treatment works to clean the surface of contaminant, while continued exposure works to incorporate greater quantities of ionized species.[105] Routing the plasma to treat the bulk of objects can be a concern. To confine the treatment, immersion ionization or a confinement chamber at low (< 100 Pa)[100,106], medium (~ 1 kPa),[107] and atmospheric (~ 100 kPa) pressures[90,101,108] have been used (Figure 2.5), reducing safety

concerns brought with corrosive components. By controlling the atmospheric pressure, one better controls the treatment environment, but this method requires additional equipment. The use of a closed vacuum system does allow the introduction of corrosive or harmful test gasses by better allowing for environmental control and dispersion of the unreacted species. To route plasma directly into objects, custom made low-temperature dielectric discharge setups can be assembled to allow routing of the plasma jet. Increasing the flow rate of the inlet gas or the back pressure can help create larger plasma plumes and aid in ionizing greater depths into 3D objects. Additionally, to create large porous printed objects, a combination 3D printing-plasma generation system may be the best course yet to fully modify an interconnected substrate. However, this would be accompanied by significant safety and cost considerations.

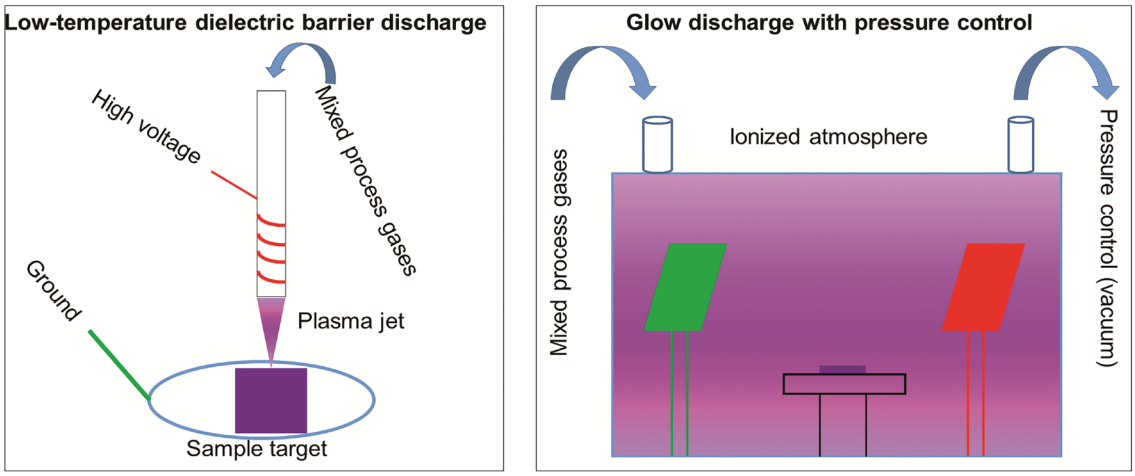

Figure 2.5 Major division of plasma treatment apparatuses. Left) A dielectric barrier discharge system is described, where gas is ionized and directed towards a target substrate. Incorporation of this approach with a 3D printing or electrospinning technique could see directed functionalization on individual fibers within a larger construct. Right) The use of a chamber in a glow-discharge system allows for greater pressure and gas composition control, as the reactive species are fully contained. Ionizing the entire atmosphere may better treat the target as well.

2.3.3 Surface Functionalization: Future Methods

Passive means to facilitate cell adhesion have laid the foundation for cell culture. The means to provide specific chemical functionality to the PS surfaces is well investigated, and the variety of applications continues to be explored. With the range of functional moieties possible, the next steps should look at mechanisms to target specific cell types and means to sequester and expand these cells. The same mechanisms which functionalize PS surfaces can be used as a base for advanced grafting techniques (such as self-assembled monolayers[109] or polymer brushes[110]). Grafting of poly(N-isopropyl acrylamide) to TCPS surfaces has successfully released adherent-culture cells, without introducing additional enzymes, by inducing a conformational change in the polymer brushes as the culture temperature passes below the lower critical solution temperature.[111] Multilayered rabbit epithelial corneal[112] and neonatal rat cardimyocytes[113] tissues have been grown *in vitro* and transplanted back into their host species, maintaining cell-cell junctions, deposited extracellular matrix, and functionality of the tissue. Plasmas containing argon and/or oxygen have been used to aid in the grafting of additional chemical species, such as N-vinyl-2-pyrrolidone, to improve biocompatibility, adhesion, and proliferation of L929 cells.[114] By selecting modifications which target or bind specific cells, successful coculture or filtration could be possible. DNA has been grafted to PS surfaces using secondary amines,[115] a technique that could be translated to antibodies as well[116–118]. Additionally, glucose has been sequestered to PS surfaces using thiol-ene 'click' chemistry,[119] a mechanism which could be further investigated for advanced surface functionalization. These approaches open the possibility for selective growth surfaces and localized coculture on single dishes, but the stability of such surfaces

must be investigated to enable large scale acceptance and adoption. Plasma preparation of surfaces can more efficiently prepare surfaces to accept patterning, without the need of stamps,[120] extensive photolithography preparation,[121] and the ability to treat large surfaces and 3D objects, something difficult to achieve with microcontact printing.[122] Selecting copolymers can also aide in effective cell and protein adhesion regulation. Further exploration of 'smart' surfaces is warranted to enhance tunable and selective culture techniques and to develop niches for specific cell types and interactions. Inkjet printing has been used to sequester cells to specific locations on PS surfaces, a step towards direct spatial patterning on proven *in vitro* growth surfaces.[51] Combinatorial screening of bioactive molecules printed or conjugated to surfaces could be used to investigate complex cellular pathways by decoupling and determining how multiple proteins impact cellular processes.[123,124] All the chemical changes possible necessitate taking advantage of the numerous means to create complex growth platforms, looking at methods to mimic the body. While chemical cues are often necessary to elicit a functional response in a tissue or target cell population, the geometry presented to the cells are often just as important and warrant discussion as well.

2.4 Fabrication Methods of 3D PS Growth Platforms

2.4.1 Motivation for 3D Platforms

The widespread adoption of standard flat cell culture dishes over the last half century has driven *in vitro* cell culture and research. TCPS dishes certainly serve their purpose, and biologically based research would not be developing cutting-edge technologies without them. However, transitioning culture from a 2D to 3D substrates could improve the biomimicry, thus improving cell-cell interactions and increasing the efficiency of *in vitro*

cell culture. Fabrication techniques, specifically casting, electrospinning, and 3D printing, seek to solidify this transition (Figure 2.6). As discussed earlier, casting is often the easiest method to produce cell scaffolding, however the production of complex 3D microstructures is limited.[51] Electrospinning can create highly porous, interconnected objects, but they are difficult to control, produce, and manufacture reproducibly.[125] 3D printing balances casting and electrospinning approaches, however; often requires expensive or custom fabrication equipment to achieve research goals.[126,127] Recently, 3D printing technology maturation continues to decrease equipment costs and increase flexibility of material choice.[36,128] Fabricating and functionalizing microspheres provides a unique path for high-density adherent-cell culture in suspension, but the applications may be limited to cell types that are able to withstand the mechanical forces in the dynamic culture system.[129] An ideal scaffold fabrication method would balance the resolution, speed, accuracy, and cost of these approaches.

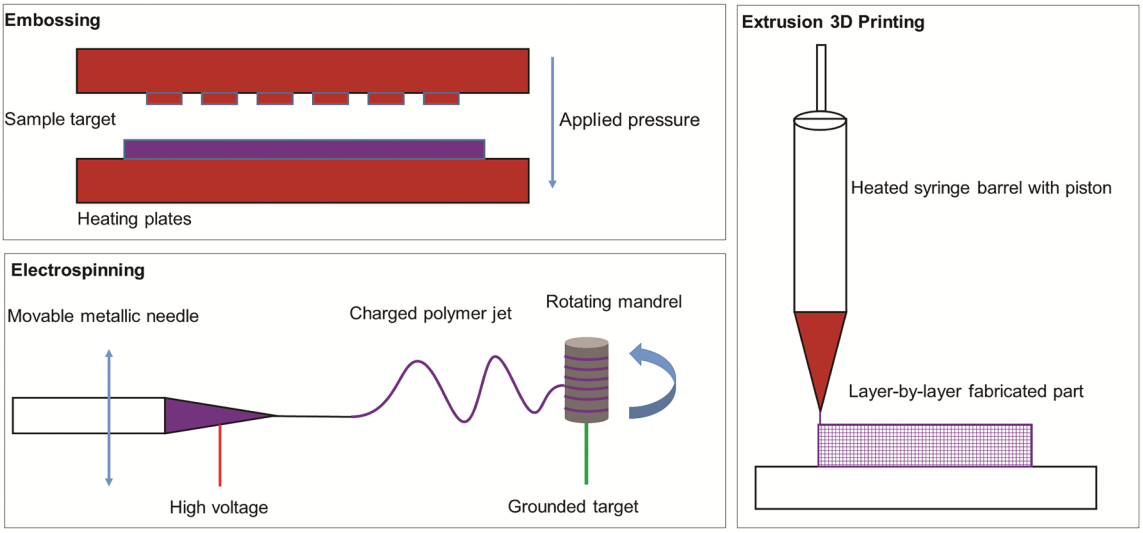

Figure 2.6 PS fabrication approaches. Top Left) High heat and pressure can be used to mold the material into highly structured shapes with hot embossing/injection molding approaches. Bottom Left) Applying a high voltage potential between the mandrel and polymer-containing syringe, electrospinning creates fine structures and repeated rotations can build dense, sizable meshes. Right) 3D printing offers an excellent balance between fabrication control and achievable detail, but little work has pursued PS as a 3D printing base for cell-based work.

Transitioning TCPS from a 2D substrate to 3D, regardless of the selected fabrication strategy, offers significant benefits. The potential exists to revolutionize cell culture: 3D models have been shown to improve disease and pharmaceutical modeling[19,130–132] and capitalize on dynamic culture methods, generating clinically relevant geometries and numbers of cells.[33,133,134] Transitioning culture from a 2D to a predictable 3D model standard would drastically increase the biomimicry of *in vitro* culture methods. These do come with additional challenges: ensuring sufficient nutrient exchange through the bulk of the object (overcome with bioreactor expansion methods[135]), visualizing growing cells (overcome with utilizing a clear material, such as PS, or with a microfluidic approach[51,136,137]), and efficient capture of the cells after culture and expansion (overcome with highly permeable, porous, and interconnected scaffolds[138,139]). Transformation of PS to a 3D culture substrate would allow continued investigation into the influences of geometry[140] and porosity[141] on *in vitro* cell growth, while utilizing a proven and versatile growth substrate. In the following section, we survey these fabrication methods and provide some perspective on continuing to advance PS as a universally accepted culture surface.

2.4.2 Fabrication: Electrospinning

Electrospinning remains a lucrative fabrication method to produce finely structured cell culture substrates. By manipulating the interactions between solvent, polymer, and current, electrospinning can form fine polymer strands to fabricate mesh structures. Where applied voltage and PS solution content have obvious influences, solvent choice impacts many solution parameters dictating PS electrospinning success (i.e. dipole moment, conductivity, boiling point, viscoelasticity, viscosity, surface tension, and

density).[142] Solvents with high dipole moment ((5.3 – 12.7) x 10^{-30} C*m) and moderate conductivity ((0 – 3.7) x 10^{-4} S/m) such as 1,2-dichloroethane, dimethylformamide, ethyl acetate, methyl ethyl ketone, and tetrahydrofuran appear to reduce the 'bead-on-a-string' morphology, producing uniform fibers therefore contributing to electrospinning sucess.[142] Additionally, reducing polymer content in PS solutions generates meshes without surface defects or beaded fibers, and increasing the conductivity of these low concentration solution tends to stretch the polymer jet better, reducing fiber diameter by an order of magnitude (down to several hundred nanometers).[125] In order to ultimately grow cells in high density in these platforms, studies investigating the effect of fiber alignment on cell attachment and morphology have been conducted on these highly packed, fine fiber as an amenable cell culture platform. (A more complete discussion of electrospinning to create cell scaffolding has been provided by Boudriot et al.[143]).

Cells are known to align along individual fibers, potentially due to the alignment of polymer chains within the larger microfibers.[144] PS microfiber meshes have been used to align and grow MC3T3 cells along the fibers, where osteoconduction was observed, therefore potentially utilizing PS scaffolds as the base for a bone scaffolding substitute. Keratinocytes and endothelial cells appear to organize themselves three dimensionally, layering in native epidermal-dermal structures along air-liquid interfaces, demonstrating intercellular signaling within the electrospun scaffolds.[145] In addition to polymer chain alignment, the porosity of the mesh architecture also influences the morphology of the adherent cells contained within the construct. Highly porous electrospun PS facilitates human induced pluripotent stem cells to develop 3D aggregates, allowing for cell

migration and signaling within a contained 3D object, and accelerating the shift to a bioreactor model with minimal external manipulation for culture, reducing or eliminating outside manipulation while maintaining pluripotency.[146] The highly porous and interconnected nature of electrospun fibers are an appealing substrate for surface functionalization, as they allow for relatively large (> 1 cm) scaffolds with micron and nano-scale inner structures to be fabricated within hours and custom functionalization to suit specific research needs.[147] The ability to physically absorb bioactive molecules, therapeutic agents, and modulate the surface chemistry and piezoelectric properties of these interconnected, high surface area objects makes highly porous electrospun meshes intriguing for tissue engineering, drug delivery, and other biomedical applications (A more complete discussion of functionalization approaches of electrospun objects has been written by Yoo et al.[148]).

The development of electrospinning technologies for PS has revealed several drawbacks, most notably the difficulty in defining and controlling fiber placement. The randomness associated with electrospun objects and random instability in the electrospray process reduces repeatability of experiments. Ambient humidity and PS molecular weight have been found to influence the development of surface pores, further reducing the uniformity of the strands and the structural integrity of the final polymer network.[149] Ambient humidity can interfere further by inducing the formation of surface winkles in the final PS mesh, which, along with voids in the bulk of strands, can be removed through annealing, adding additional processing steps which could harm the delicate structures formed.[150] From our on-going work with 3D-printed PS, environmental influences, such

as ambient humidity, appear to have little influence on fiber morphology, so long as the base material is stored properly. The substantial influence of environmental conditions in electrospinning necessitates highly controlled environments for the work, or significant time investment to achieve morphologically expected scaffolds. The above reasons make more directly controllable methods, like 3D printing, appealing, often allowing for greater environmental flexibility and control over the fabricated object.

2.4.3 Fabrication: 3D Printing

A significant need exists to fabricate customized structures with biological relevance, and 3D printing is emerging as a leading technology to achieve these goals. Over the last several years, various 3D printing technologies have moved within reach of even the most casual researcher. However, PS has generated little research interest to date as a 3D printed, cell-contacting growth material. This likely stems from the difficulty in liquefying PS without thermally degrading PS, as the polymer structure will break-down before transitioning fully to a true liquid from a solid.[151] Overcoming this obstacle requires specialized equipment to extrude the semi-solid. In addition, fine fibers of PS are mechanically weak. These limitations often limit PS's application as a primary structural element in 3D printed constructs, relegating PS to serve as a coating. For instance, optically clear support materials, such as Vero Clear, can be printed to form channels with an oxygen plasma activated PS coating.[152] This allows for both specific surface functionalization and direct scaffold control. These methods facilitate interactions between printable materials and cells by utilizing chemical interactions known to be amenable to cells. However, emerging evidence demonstrates the ability to directly 3D print PS,[153] making these grafting approaches obsolete.

Commercially available products now exist using 3D printed, plasma treated PS to grow and isolate cancer cell lines, with potential applications in general cell culture.[153] 3D printing provides a method to design and test culture surface geometry tailored to specific cell environments. By utilizing computational modeling to quantify surface shear stresses, oxygen content, and mechanical stresses,[154–158] there remain many possibilities for *in vitro* cell culture with targeted biological applications (e.g. the bone marrow niche). By coupling relevant biological regulators with large and internally complex surfaces, one would be able to grow large numbers of cells on biomimetic objects.

The evidence is present to establish the feasibility of complex 3D printed PS parts to become scaffolding for cells and harnessing the same surface functionalization methods employed in 2D. 3D printed PS should become a mainstay for cell culture, allowing for concentrated culture volumes, dynamic culture environments, and complex surface chemistry to dictate cellular interactions for *in vitro* study. Unfortunately, the financial barrier to 3D print scaffolds leads researchers to seek other methods to capitalize on dynamic culture approaches. A highly sought approach incorporates individual beads to encapsulate cells, either fused together generating a single larger object,[159] or circulating within the culture media. Microsphere carriers provide an alternative to structured scaffolds, allowing direct surface customization and dense cell culturing.

2.4.4 Fabrication: Microspheres

Microcarrier culture aims to suspend beads on the order of (0.01 – 1) mm in media and maintain the culture suspension with a bioreactor.[160] Cells can adhere to the bead surfaces

and remain suspended to increase culture density and utilize similar advantages of other bioreactor cultures (e.g. shear stress, oxygen content, geometry effects). These microspheres can be fabricated directly with a microhead[161] or in solution through dispersion polymerization, with the ability to control the particle size and molecular weight.[162] Microspheres remain an appealing option for cell culture: the high density of suspended carriers and scalable volumes effectively increases culture area to yield large numbers of phenotypically expected adherent cells.[163] Particularly, PS microspheres have been successfully fabricated through the mini-emulsion process, yielding PS carriers as small as 115 ± 9 nm with both carboxylic and amine tags, to activate pro-inflammatory responses in human macrophages.[164]The versatility of fabricated and commercially available beads remains unparalleled. As a base growth platform, PS microspheres can be functionalized using corona discharge or induced to carry a positive surface charge.[129] As a core-carrier, PS microbeads can be coated to carry proteins,[165] glass,[166] or peptides[163]. PS microbeads functionalized with quantum dots and magnetic nanoparticles efficiently facilitate capture and specific population enrichment.[167] Targeted functionalization of PS microspheres could be used to guide cell differentiation in large scale bioreactors without modifying the media composition, taking advantage of known chemo-responsive cell types, as previously performed with other base materials.[168] Carboxylated PS has been shown to create a surface with high epithelial cell attachment efficiency on static microbeads.[169] In addition, PS microbeads make excellent carriers to facilitate cellular uptake to deliver exogenous cargo,[170,171] DNA vectors,[172] monoclonal antibodies[173] or for localizing within tumor spheroids.[174] However, a major drawback to microcarrier culture, can be the clustering of the cell carriers, resulting in aggregated spheroids rather than

distinct circulating populations, poor attachment efficiency, and the difficulty in retrieving grown cells.[175,176] To diminish these draw backs, additional culture steps are necessary, such as cell suspension filtration to separate carriers from cell populations during harvest.[177] While the flexibility of microbead culture, from modulating surface charge to conjugating proteins through EDC chemical linking has been found to help facilitate binding and attachment,[178] the presented limitations reduce the clinical applicability of microbead systems.

2.5 Conclusions

PS has been thoroughly explored as a useful cell cultivation tool for decades, but the applications of the polymer may just be starting to be harnessed. The proven cell culture substrate shows promise for future and continued use but needs to be upgraded for the current challenges in the 21st century. For too long, researchers have relied on basic oxidized surfaces, where the possibility has been demonstrated to create specialized surfaces to select distinct cell populations or phenotypes. As the understanding of cell culture improves, so should the substrates used to grow the cells, becoming more specific and targeting individual populations.

As cell culture transitions from 2D to 3D substrates, so too should the most basic designs of cell culture platforms develop. A wealth of knowledge is out there, waiting to be tapped into including basic scientific understanding of how cells attach and regulate growth *in vitro* and why certain residues are more appealing to cell culture. Translating these to applied research could look at functionalizing materials to yield specific responses (e.g. directing differentiation of stem cells). There exists a wide range of

possible of research questions, tackling this most basic of culture surfaces. The only question left is: where is PS going as a culture surface?

As tissue culture continues to evolve, so should our surfaces. Whether this is through specific chemical or recognition moieties, or 3D environments to best harness the power of *in vitro* culture to mimic a cell microenvironment, treating culture surfaces to specifically act for a given cell type provides a course for personalized medicine and directed cell growth. TCPS provides a cost-effective means to grow a variety of cells, but better, equally stable, materials continue to be investigated to shrug the 'one-size-fits-all' approach to *in vitro* cell culture. The optical clarity and relative cost make PS a unique material to spearhead these efforts to customize surfaces. The presentation of phenyl rings provides many locations to facilitate cell-focused functionalization, and the low crystallinity of the material allows for relatively low processing temperatures. This combination of material functionality and formability is unique for a culture substrate, and likely holds many opportunities for advancing cell culture beyond the 50-year-old flat, traditional culture dish.

Chapter 3: 3D Printing in Cell Culture Systems and Medical Applications[ii]

This chapter discusses applications where 3D printing is being implemented to improve human health and welfare. 3D printing holds unique opportunities with the flexibility the technology allows with regards to material choice, scale of applications, and ability to rapidly modify the design. These characteristics have moved rapid prototyping from the tool-shop, to the lab bench, to a validated manufacturing approach. This chapter discusses pharmaceutical compounding and delivery, bioreactor development, microfluidic platforms, tissue models, imaging approaches, and surgical tool development. Cases in specific hard and soft tissue recapitulation are also discussed. 3D printing's impact on the medical field and future ramifications in the medical field, from device development to cell culture, are discussed. These various applications and recent improvements afforded with 3D printing highlight the important role the technology plays in modern medical research.

3.1 Introduction

3D printing has rapidly moved from an innovation novelty, to a widely accessible desktop fabrication method. With clinical applications in mind, rapid prototyping provides enormous flexibility and opportunity for engineers, physicians, and researchers to work collaboratively and rapidly solve medical problems. Currently, there are more than 20 active or recruiting clinical trials involving a 3D-printed component, ranging

[ii] Adapted and reprinted with permission from: MJ Lerman, J Lembong, G Gillen, and JP Fisher. 3D Printing in Cell Culture Systems and Medical Applications. Applied Physics Reviews. 5, 2018, (041109).

from metal bone implants, atrial fibrillation assistant devices, pulse oximeters, and sleep apnea masks.[179] This clinical work is proving fruitful, as many 3D printing-based technologies have received FDA clearance.[180] However, these devices remain primarily acellular. (For a discussion of cellular based bioprinting, see Cui et al.[181]). 3D printing has wide appeal clinically to rapidly observe, design, and fix defects in a single day. The flexibility in acceptable designs and materials without sacrificing resolution or fabrication time has pushed clinically based research to embrace the technologies. In this chapter, we look at various 3D printing approaches (Table 3.1) for pharmaceutical delivery, fabrication of acellular scaffolds, bioreactor systems, medical model devices, and organ-on-a-chip systems with practical applications in the clinic.

Table 3.1 Summary of 3D printing technologies utilized in clinical applications.
Technologies are grouped by type with general resolution, material compatibility, print rate, material costs, typical part sizes and part costs. Specific references for technologies are listed. Note: Resolution, print rate, and costs are approximate and do not consider equipment purchase costs, which can be significant and manufacturer dependent.

Method	Resolution	Material Compatibility	Print Rate	Material Cost	Part Size	Refs.
Extrusion: 1) Fused Deposition Modeling 2) Extrusion Modeling	50 µm – 1 mm	Materials must be extrudable as a semisolid melt or filament wire to melt directly at extrusion tip. This is generally limited to thermoplastics, but can include epoxies, composite materials, metals, cell-laden gels, and hydrogels, depending on the printer.	0.1 mm/s – 100 mm/s extrusion rate	≥20 $/kg	10 mm^3 – 50 cm^3	[182]
Energy Projection: 1) Digital Light Processing (DLP) 2) Stereolithography 3) Two-Photon Polymerization	200 nm – 100 µm	Materials must be crosslink-able liquids. Crosslinking is typically initiated by ultraviolet or visible light sources for DLP and stereolithography and infrared lasers for two-photon polymerization. Often only proprietary materials can be used with specific printers. Frequently these printers are used to generate fine featured parts.	1 min. – 10 min. per layer	≥500 $/kg	100 μm^3 – 10 cm^3	[183,184]
Selective Melting: 1) Laser Sintering 2) Electron Beam Melting 3) Powder Bed Fusion	100 µm – 500 µm	Ideal for high melting temperature materials, including metals	1 min. – 10 min. per layer	≥50 $/kg	1 mm^3 – 100 mm^3	[185,186]

3.2 Pharmaceutical Delivery with 3D Printing

3D printing has shown promise as means of delivering therapeutics with controlled, patient-specific dosages by compounding polymer filaments with medications, and varying both loading quantity and total mass of the tablet.[187] Research into 3D-printed tablets has shown that drug release profiles can be controlled and designed to deliver active pharmaceutical ingredients (APIs) to intended therapeutic locations.[188,189] A number of medications have been compounded directly mechanically or absorbed into desktop extrusion 3D printing (e.g., Fab@home, MakerBot Replicator 2) filaments with material bases of hydroxypropyl methylcellulose, poly(acrylic acid), poly(vinyl alcohol), poly(lactic acid) (PLA), and/or Eudragit EPO. APIs include guaifensin,[190] aminosalicylate,[191] nitrofurantoin,[192] and theophylline[193,194]. Customizing the filament formulation based on degradation mechanism, miscibility, and carrier geometry has been shown to improve compounding, extrusion, and release behavior,[194–197] and is easily explored using these extrusion 3D printing systems. Multiphase dosing,[190] multiple simultaneous drug combinations,[195] and 3D-printed non-degradable casings[198] show promise for medications administered together frequently or of varying dose to maintain therapeutic effect by fabricating API carriers to meet individual patient needs. Importantly, APIs appear to remain in their intended therapeutic form following printing.[192] With the prevailing evidence and extensive testing, the Food and Drug Administration (FDA) approved the first oral prescription therapy using 3D printing technology in 2015, where the APIs are added directly onto a powder bed to create patient-specific dose.[199,200] With Aprecia's ZipDose technology, a pharmaceutical containing layer is laid flat, then set with a binding liquid to control shape of the drug;

dosing is controlled by repeating this process to the desired number of layers.[200] Continuing this work would realize additional therapies beyond epilepsy treatment. Applications of controlled pharmaceutical delivery are not limited to ingestible tablets and pills. Using extrudable materials, such as ethylene vinyl acetate, poly caprolactone (PCL), and PLA on a MakerBot Replicator 2, custom drug-releasing polymers can provide pharmaceutical dosing and prevent biofilm formation on custom intrauterine implants[201,202] and potentially catheters[203]. Rapid prototyping of functionalized polymers could lead to novel devices like coronary stent, gastric, and neurological implants where both technical design requirements and drug eluting or antimicrobial properties remain pertinent. The relatively little amount of time where an API-loaded filament is exposed to high heat, as compared to traditional injection molding techniques, likely contributes to the API's intended therapeutic effects following printing. 3D printing's greatest engineering impact remains in rapid modification of designs to address niche clinical issues, rather than mass produced components.

3.3 3D Printing Applications in Fabrication of Bioreactors and Alternative Culture Systems

Applying 3D printing to fabrication of culture systems may offer a more realistic biomimetic environment for cells, resulting in physiologically relevant cell phenotypes.[204] 3D printing is particularly useful for such cell culture applications due to the capability to achieve geometries that are otherwise difficult to fabricate using conventional techniques (e.g., casting, electrospinning, etc). This technique can produce features with sizes that are relevant to cells, where parameters such as porosity, substrate roughness, and curvature can be tuned. Ultimately, the effect of these parameters on

cellular behavior (growth, cell alignment, differentiation, etc.), are investigated in these 3D culture platforms. The key to applying this technique for cell culture platforms relies on fabricating a geometry that provides the correct mechanical cues[205,206] (e.g., through perfusion flow that is guided by the geometry), and consequently the chemical cues,[207] that are needed for proper cellular signaling, specific tissue growth and development, and through cell-substrate interactions. The capability to fabricate application-specific geometries using 3D printing, which consequently dictates the substrate's mechanical properties and cell-cell organization, drives the development of culture platforms that can mimic various tissues.

Flat culture dishes, specifically tissue culture polystyrene, have been the foundation of biologically-based research, as it supports efficient cell expansion. As various biomedical fields grow, vigorous research efforts related to tissue / organ development and disease modeling emerge, and therefore so does the need for a cell culture platform that provides biomimicry, which flat culture dishes fail to provide. Transitioning culture from 2D to 3D substrates could improve the biomimicry, thus improving cell-cell interactions and increasing the efficiency of *in vitro* cell culture, and have driven greater interest in complex topology and material choices for extended and directed cell growth.[208]. For this application, 3D printing has been used to fabricate complex geometries with specific architecture, interconnected geometries, and microporous surfaces to facilitate tailored cell responses. Initial design of these cell culture platforms should utilize computational modeling to design the scaffold, in which one can study the fluid dynamics and understand the mechanical force transmission, therefore predicting the forces acting on

the cells once these acellular constructs are seeded with cells. Successful integration of modeling and part design can yield scaffolds for cell culture which balance mechanical integrity with porous structures facilitating nutrient exchange and cell infiltration, and may direct cell behavior.[209–211]

3D printing allows for great flexibility in compounding multiple components to 3D – printing chemically complex homogenous materials unavailable in traditional manufacturing environments. This includes combinations of porogens, polymers, metals, and ceramics used to mimic the mechanical and/or chemical properties of native tissues, and creating complex, interconnected, topography.[212,213] Incorporating these chemically and topologically complex constructs into dynamic culture techniques generally improves cellular infiltration and media exchange, therefore better replicating the native environment.[31] Crucial aspects of cell culture applications within 3D-printed scaffolds include cell expansion and migration, attempting to improve construct models to evaluate cell function *ex vivo*.[214] With all scaffolds, design approaches which verify study requirements ensures anticipated cellular outcomes are achieved and research objectives are met, such as fluid flow dynamics, mechanical force transmission, elasticity, porosity, etc.[215] Without this design feedback, ultimate study results remain hard to support and justify.

The recapitulation of tissue models achieved through three-dimensionality, aided by 3D printing, typically provides an environment that better sustains cell proliferation and differentiation. These 3D-printed cell culture systems are often substitutes for existing

commercial culture platforms, providing a more cost-effective, well-tailored solution for specific interests, and are therefore customizable for optimized specific tissue applications. One popular platform for cell culture is bioreactors for dynamic culture, which has been shown to enhance cell seeding efficiency,[216–218] proliferation,[219–222] and differentiation of various cell types.[33,223–230] For example, dynamic culture of human mesenchymal stem cells (MSCs) in a tubular perfusion bioreactor containing 3D-printed (with Eshell 300 as the resin on an EnvisionTEC Perfactory 4) vascular networks for an *in vitro* engineered bone tissue was found to increase the cell viability by 50 % in the core of the construct compared to the static culture.[133] Through 3D printing, interpenetrating networks with various geometrical parameters (porosity, pore-to-pore distance) can be fabricated. Investigation of the effect of these parameters on the cellular response and mass transport within the tissue can be performed.[231] Such porous networks provide three-dimensionality to tissue models, allow nutrient diffusion and cell migration throughout the printed construct, and provide a high surface area per volume ratio for cell attachment and growth, increasing media efficiency. Additionally, the digital light processing (DLP) system selected balances both feature size, part size, and fabrication time / cost for this vascular application.

More recently, a 3D-printed miniaturized, modular spinning bioreactor was developed and used to generate forebrain-specific organoids from human induced pluripotent stem cells (iPSCs).[232] The design utilizes computer-aided design (CAD) and 3D printing to optimize designs that sustain organoids of varying sizes in suspension under moderate spinning speed and prevent aggregation. The bioreactor was 3D-printed using the Fortus

400mc printer (Stratasys), with the ULTEM 9085 heat-resistant plastic as the printing resin. The use of this bioreactor was shown to enhance cell viability and promote maintenance of the stem cell niche in the organoid compared to static cultures. Existing culture dish-based cerebral organoid models have limited applicability since they poorly mimic key features of the human brain development. Specifically, culture dish-based models contain progenitors that show morphological characteristics of outer radial glia cells, but not a well-developed outer sub-ventricular zone. The design of this culture platform, as enabled by 3D printing, allows custom, optimized design for the creation and maintenance of tissue models that resemble critical aspects of human cortical development in an affordable, high-throughout, and reproducible organoid platform. In addition to the enhanced biomimicry and functionality of the organoid, the custom bioreactor design also improves upon currently available spinning bioreactors, whose scalability is inhibited by the large required incubator space, frequent media exchanges, and large sample-to-sample variability.[232]

Continued bioreactor system development seeks to scale up cell culture for large-scale clinical applications. For various clinical applications, large-scale production of cells is necessary to meet the dosage requirements. It is important to first understand scope of the clinical target and then work backwards to develop smaller scale culture platforms where studies can be done to investigate cellular mechanisms and scalable processes can be optimized at a much lower cost. This view has pushed research to scale-down. Integrating 3D printing presents a unique avenue to demonstrate small scale feasibility and perform

extensive investigation using a much smaller footprint and working volume prior to migration to production scale or clinical applications.

3.4 3D Printing of Droplet-Based Microfluidic Devices for Cell Encapsulation

The capability to spatially and temporally control cell growth and stimuli through substrate geometry and fluid transport, while simultaneously providing a platform for cell imaging, image-based analysis, and further biochemical analysis of single cells in tissues, makes microfluidics popular for biological applications.[233] However, conventional poly(dimethyl siloxane) (PDMS) -on-glass microfluidic device fabrication starts with a complicated, time-consuming soft lithography process requiring expensive equipment in a cleanroom facility.[234] This is followed by the assembly, which requires access to plasma treatment equipment.[234] Alternatively, recent advances in 3D printing technologies support single-step and rapid fabrication of highly complex microfluidic devices, while reducing costs associated with institutional infrastructure, equipment, and physical space.[234] Consequently, microfluidics are becoming widely accessible with the increasing availability of high-precision 3D printing.

One of the uses of 3D printing technology for the development of cell culture systems is the fabrication of microfluidic devices for high-throughput fabrication of hydrogel scaffold droplets for cell encapsulation. A microfluidic chip incorporating a coaxial flow device for co-extrusion has been fabricated using a DLP 3D-printer (Asiga pico27 with Asiga platclear resin) to generate an extracellular matrix (ECM)-coated, hollow, sub-millimeter alginate capsules to encapsulate cells.[235] The device enabled the creation of an enclosed microenvironment within each sphere, which mimics the basal membrane of the

cellular niche. Human neural stem cells derived from human induced pluripotent stem cells can be cultured and differentiated into neurons. A Lego-like modular 3D-printed microfluidic device has also been developed and used to encapsulate dental pulp stem cells within alginate droplets.[236] The devices were produced using fused filament fabrication in an Ultimaker 2 printer, with clear PLA as the printing material, resulting in a rapidly manufactured, low cost, transparent device that can be utilized for cell imaging. Furthermore, combination of 3D printing methods can be applied to construct a low-cost microfluidic chip for long-term 3D cell culture and growth; this application combines a stereolithography-based desktop 3D printer and an industrial 3D printer based on polyjet technology.[237] In addition to 3D cell encapsulation, this platform's capabilities also include spatial patterning within gelatin methacryloyl (GelMA) hydrogels, as well as complex, predictable, and controllable fluid flow patterns inside the 3D channel.

Similarly, generation of multicellular spheroids has been demonstrated inside a microfluidic device fabricated with a Object260 Connex printer with VeroClear-RGD810 resin and with a commercial stereolithography-based contract manufacturer (Proto Labs) using a polycarbonate based resin.[238] The internal device geometry immobilized the spheroids, and gravity-driven flow perfused the cell-containing circuit. Viability and functionality of patient-derived parental and metastatic oral squamous cell carcinoma tumor and liver cell (HepG2) spheroids were maintained, presenting a simple device with possible applications in investigations of drug efficacy, metabolism, and toxicity.[238] Enabled by 3D printing approaches, the capability for fabricating geometrically-defined micro-tissue models containing single cells and spheroids have allowed researchers to

develop model cellular systems to study mechanistic interactions with their microenvironment, giving rise to understanding of various physiological processes and disease mechanisms

3.5 3D Printing of Culture Platforms for Cell/Tissue Models and Mechanistic Cellular Studies

In addition to the capability of fabricating microenvironments that mimic physiological tissues, the versatility of 3D printing in creating large, complex shapes also enable the development of culture constructs that capture interactions of multiple tissues. While previous two sections focus on the use of 3D printing for dynamic culture systems (bioreactor, microfluidic devices), this section emphasizes on utilizing 3D printing to mimic specific biological features of tissues to capture cellular function and physiology inside a culture platform. These features allow for the study of diseases related to that particular tissue. For example, a dual-chamber bioreactor setup was fabricated and fitted into a microfluidic base as a representative model of the interactions between cartilage and the subchondral bone.[239] The bioreactor chamber and parts were fabricated using a stereolithography apparatus (EnvisionTec), with Eshell 300, a printing-material system capable of generating fine features with a non-cytotoxic resin. The geometry allows insertion of a biphasic osteochondral construct made from GelMA-encapsulated MSCs into the bioreactor chamber, which consequently exposes the chondral and osseous sides of the construct to chondrogenic and osteogenic medium, respectively. Such interaction between tissues in a controlled bioreactor environment provides a path to investigating the osteochondral tissue physiology, and possible pathogenic mechanisms of relevant diseases in the system such as osteoarthritis.

The use of 3D printing for cell culture platforms also enables development of miniaturized systems due to the high achievable resolution of various printers. For example, stereolithography-based printers have typically achieved a high spatial resolution, giving structures with dimensions of less than 10 μm,[240] while microsterolithography systems incorporating two-photon polymerization have been reported to improve the spatial resolution of printed scaffolds down to <1 μm.[241] The fine features observed with this fabrication method enables mechanistic studies of cells in tissues. For example, in addition to mimicking the key features of human cortical development, the brain-region-specific organoids were also employed to model Zika virus exposure, where decreased neuronal cell-layer volume, resembling microcephaly, was observed.[232] Similarly, a 3D-printed fluidic microscale bioreactor has been developed for characterization of gastrointestinal epithelial cell physiology.[242] The fluidic bioreactor was 3D-printed using the Object30 Pro extrusion-based printer with VeroClear-RGD810 (Stratasys), where it houses a porous villous scaffold that mimics the topography of the small intestine *in vitro*. This 3D platform provides both accurately-sized villus topography and fluid flow to improve the study of intestinal absorption, drug delivery, and barrier function. Mimicking the structure-function relationship extends across the body. For example, a 3D-printed placental model has been developed, where spiral artery geometry was successfully fabricated using an extrusion based EnvisionTEC Bioplotter with GelMA. With the incorporation of bioactive factors contained in placental ECM, this 3D-printed model was then used to study cellular migration in the development of preeclampsia, by placing growth factor loaded resin precisely.[243] When

the length scale of the fabricated models mimics relevant physiological dimensions, mechanistic studies can be performed on the cellular level, e.g. investigation of the impact of surface topography and fluid flow dynamics on cell growth, proliferation, and organ cell function.[242] Additional biomimicry is possible by combining manufacturing methods. For example, combining electrospinning and 3D printing has produced tympanic membrane analogues which successfully align fibers and facilitate cell growth, a promising start towards an implant and functional replacement of native tissue.[244] Further investigation, such as sound transmission or *in vivo* implantation would further demonstrate feasibility. Continued development of these and other 3D-printed medical technologies are likely to increase the understanding of cell behavior and interactions as test devices improve biomimicry.

3.6 3D Printing of Cell Imaging Platforms

While the use of 3D printing for culture systems is typically geared towards mimicry of tissues and enhanced cellular functions, other popular applications of 3D-printed culture platforms include cell/tissue imaging. For example, a 3D-printed, modular perfusion culture system was fabricated using the Object 260 Connex extrusion-based printer (Stratasys) and then integrated with miniature peristaltic pumps for live-cell imaging assays of easily incorporated microfabricated scaffolds.[245] Due to the modular design, possible studies with this platform included investigating the cellular response to chemical stimulants down to the single cell level using fluorescence imaging in long-term perfusion cultures. Another example of the use of 3D printing in cell-based imaging applications is the UniverSlide, a 3D-printed microscopy chamber for multidimensional imaging.[246] The frame of the UniverSlide is fabricated using the Micro Plus

stereolithography 3D printer (EnvisionTEC) and is meant for use in a long-term imaging experiments due to the chamber's controlled environment, compatibility with commercially available microscope stage holders, and possible perfusion. Due to the incorporation of a transparent agarose pads with imprinted microwells as the base, the platform is ideal for cell trapping and subsequently 3D visualization and tracking. Though it remains possible to image cells within 3D-printed constructs without sectioning, such as with confocal or fluorescence laminar optical tomography,[247] designing test objects from the start remains the easiest method to observe cellular interactions and mechanistic changes.[26]

3.7 3D Printing for Organ-on-Chips Applications

3D printing is being used to create tissue models and artificial organs inside microfluidic devices with the goal of providing the complexity, function, and physiological responses of real organs. The field of organ-on-a-chip engineering has integrated 3D printing technology by assembling tissues containing cells, ECMs, and other biomaterials with precisely controlled spatial distribution, creating organ models with 3D specific cellular arrangement within a microfluidic chip. The incorporation of other mechanical and electrical components into organ-on-a-chip systems is simplified in fully 3D-printed systems, enabling automated mass production and facilitating commercialization.[248] The ease and high-resolution of 3D printing for organ-on-a-chip applications provides a promising alternative to animal studies and conventional cell culture for investigating various biomedical research questions.[249] Review articles have been written where summary and advances in organs-on-a-chip technologies for tissue engineering applications are provided.[250–252] In this section, we will focus on recent developments that

specifically utilize 3D printing for fabricating functional organ-like models and molds for use inside microfluidic devices.

Combining precise geometrical features possible with 3D printing, well-defined flow patterns, and imaging capabilities of microfluidic devices, a perfusion microfluidic platform has been developed to simulate the blood-brain barrier (BBB) environment. The BBB model is composed of a porous membrane where brain microvascular endothelial cells and rat primary astrocytes are cultured on each side of the membrane.[20] The modular chamber consists of sterilized parts fabricated using an Objet 30Pro printer with VeroClear (Stratasys) assembled with a cell insert accommodating two cell monolayers forming a complete closed-loop perfusion system. Characterization of the *in vitro* model reveals a high-fidelity solution to studying the BBB biology due to the fluid residence time, perfusion rates, permeability coefficients of model drugs (caffeine, cimetidine, and doxorubicin), and trans-endothelial electrical resistance (barrier integrity) that mimic *in vivo* values. Such functionality means the BBB-on-a-chip could effectively screen candidate drugs targeting the brain, overcoming the limitations of typical BBB transwell culture, where controlled biochemical gradients are difficult to achieve in the large static fluid volume.

Similar to the BBB-on-a-chip model, cocultures relevant to other disease models are constantly being developed and optimized to capture biological interactions forming disease mechanisms. A 3D bone-on-a-chip model made of PDMS has been developed, consisting of cell growth chamber and a media reservoir that are separated by a

membrane to investigate metastasis of breast cancer cells to host bone marrow.[253] The PDMS chambers were fabricated by casting over a 3D-printed (Rostock MAX V2 Desktop 3D-Printer) mold, resulting in a transparent growth chamber that allows for easy and frequent monitoring of the breast cancer model. Growth and phenotypic maturation of mineralized collagenous bone tissue was observed simply by modifying the geometrical features of the membrane and the culture chamber, optimizing for nutrient and waste transport and providing appropriate concentration of bone matrix building proteins. Through 3D-printing, fabrication of this bone-on-a-chip geometrical design was enabled, allowing maximized cancer cell interaction with bone matrix of a concentrated surface area in a high-throughput experimental fashion. This serves as a reliable *in vitro* model that captures the complexity of the native bone environment and mimics *in vivo* processes, thus eliminating the need to obtain bone metastasis samples from human patients, which has been one of the major limitations in studying breast cancer bone colonization.

A 3D printing approach for a perfused liver organoid model on a chip has been demonstrated where the model entails the sinusoidal structure of the liver lobule as enabled by 3D printing (Cellbricks Bioprinter), with gelatin and poly(ethylene glycol) (PEG)-based bioinks.[254] Characterization of HepaRG (a human hepatoma cell line) and human stellate cells cultured for two weeks within the liver organoid-on-a-chip revealed higher expression of albumin and CYP3A4 proteins in 3D-printed tissues compared to monolayer culture. Hepatocyte functionality was shown through tight junction formation and stable overall metabolism by glucose, lactate, lactate dehydrogenase, and liver-

specific bile transporter multidrug resistance-associated protein 2 levels. This liver-on-a-chip model serves as an alternative platform for complex 3D liver model development, as opposed to 2D models, which are not as physiologically relevant, or the gold standard 3D spheroid culture, which are limited by diffusion of nutrient and oxygen. Utilizing 3D-printing capabilities, the geometry of the developed liver-on-a-chip can be tuned to ensure adequate nutritional supply within larger tissue models, therefore providing a new avenue to perform mechanistic studies in liver tissue engineering.

The organ-on-a-chip field exhibits an increasing demand to integrate other systems (e.g., electrochemical components, sensors and actuators, and imaging systems) to fully capture the functionality of the organ in interest. Particularly, as 3D printing requires a CAD model to produce shapes, incorporating scanning/imaging techniques into the fabrication of organ models are often applied. In fabrication of a 3D model of arterial thrombosis, computed tomography angiography scans were acquired, constructed, and processed into a printable 3D model.[255] The molds for microfluidic chips containing miniaturized healthy and stenotic vascular structures were fabricated using a Perfactory 3 stereolithography 3D printer with PIC100 resin with the resolution set as low as 25 μm. Taking advantage of the printers resolution limits, artery models within a microfluidic device successfully recapitulated vessel environments: confluent coating of the vessels with human umbilical vein endothelial cells, flow of human whole blood at physiologically relevant shear stresses, and thrombosis induced at and downstream of the stenotic region were observed.[255] Mimicry of shape, cellular environment, and functional response of this 3D-printed organ-on-a-chip model emphasizes the superiority of 3D

printing over typical microfluidic fabrication employing 2D soft lithography. Traditional microfluidic fabrication is limited to generating two-dimensional microstructures or 3D structures with very limited thickness. These design limitations coupled to the multiple complicated and time-consuming fabrication steps highlight the advantages of 3D printings. Structured-light scanning has been used to capture 3D topographical data of whole organs to generate a 3D-printed microfluidic device that directly interfaces with porcine kidney as a non-invasive platform to isolate and profile biomarkers from whole organs in real time.[256] The functionality of this conformal microfluidic device was shown by the transfer of relevant metabolic and pathophysiological biomarkers from the cortex of the kidney to the microfluidic device while fluid flow is present in the microchannel. The use of this device could potentially overcome the limitations of whole-organ studies simply by facilitating transport of relevant markers of the corresponding organ to a much smaller platform and the subsequent analysis.

Highly complex organs require complex *in vitro* models, often incorporating high numbers of inputs and outputs within the corresponding organ-on-a-chip system. By integrating 3D printing, templating, sensors, and system automation, a 16-channel microfluidic perfusion chamber has been developed for investigating endocrine tissues and secretions.[257] This device is capable of precise temporal manipulation of nutrient inputs and hormone outputs, shown by the measurement of real-time fatty acid uptake by adipose tissue exposed to a temporal mimic of post-prandial insulin and glucose observed by fluorescence imaging. The demonstrated flexibility of the listed platforms suggests feasible use of 3D-printed microfluidics as building blocks for an integrated, modular

organ-on-a-chip microfluidic devices. Further validation of these models could lead to broadly accepted use, becoming the new gold-standard for studies investigating mechanistic interactions of cell populations.

3.8 3D Printing for Orthopedic, Dental, and Craniofacial Applications

Orthopedic reconstruction with 3D printing technologies has garnered the greatest interest, likely due to the relative ease in manufacturing stiff materials and replicating the rigid structures. Materials range from stereolithographically cured poly(propylene fumarate),[258] to sintered ceramic-polymer blends.[259] By matching material choices, fabrication systems, and patient defects, 3D printing technologies can serve to improve patient outcomes. For bone implants, the use of materials and structures which induce bone regeneration and cellular infiltration present a viable path for custom implants. The resorption, integration and osteoconduction of bioceramics such as brushite and monetite, have survived 12 weeks in goats having undergone decortication of the lumbar transverse process, with significant bone formation seen in intramuscular implants.[260] Metal coatings (e.g., with niobium)[261] or select stable polymers (e.g., poly(ether ether ketone))[262] can improve porosity, osteointegration, and differentiation with surrounding tissue. With these stable materials capable of and inducing *de novo* bone regeneration, it remains critical to choose material systems which facilitate expected fabrication and can support cell growth, even if serving as sacrificial material.[263] Combining biphasic calcium and zirconia in an extrudable paste has successfully been used to fabricate biomimetic objects which induce differentiation.[264] Greater complexity to these implants can be achieved with extrusion 3D printing approaches. Interweaving multiple materials together, such as a BMP-2 containing collagen solution in between PCL/poly(lactic-co-

glycolic acid)/β-tricalcium phosphate fibers becomes possible with custom extrusion 3D-printers.[265] Directly compounding PLA and hydroxyapatite filaments for fused deposition modeling allows direct integration with commercial fused deposition modeling systems (i.e. 3DPRN LAB 3D).[266] 3D printing materials containing bioactive components has resulted in greater bone regeneration over multiple months as compared to non-bioactive implants.[265] Mimicking calcified bone with bioactive scaffolds has worked to guide MSC osteogenic differentiation in otherwise difficult regions where traditional implants may not succeed, such as the anterior cruciate ligament.[267] Including additional coatings, such as dopamine, can be added to induce osteogenesis and angiogenesis, regulating cell behavior towards a functional implant.[268]

Total reconstruction of the knee looks within reach; aligning collagen fibers with 3D-printed acrylonitrile butadiene styrene (ABS) fibers forces cells to align in hopes of encouraging tendogenesis.[269] A 3D-printed poly(carbonate urethane) – ultra-high molecular weight poly(ethylene) meniscus fabricated with a Lulzbot TAZ 6 extrusion printer shows some promise as a replacement device with appropriate wear properties demonstrated, with further investigation needed.[270] Continued developments of these technologies may yield custom 3D-printed total knee replacements in the near future. A 3D-printed casing made of MED610 on an Objet Connex 3D printer (Stratasys) held alginate beads loaded with MSCs have successfully been cultured in the shape of a human femur, showing potential to regenerate large bone sections.[134] Integrating a vascular network and rigid structure would increase the clinical relevance of such an implant, ultimately moving towards a load-bearing bone-regenerating implant. Varying

the hydroxyapatite content[271] and fiber oritentation[272] in 3D-printed objects could lead to zoned-structured objects where integration between tissues could help improve implant acceptance by mimicking the non-uniformity seen in biologic interfaces. These orthopedic structures benefit from the patient specificity available with 3D printing. 3D-printed structures tend to either maintain the structural stability demanded in orthopedic implants or tissue engineered approaches to induce active osteogenesis and osseointegration of the surrounding tissue. Further work to marry the mechanical and biological aspects of bone implants is warranted.

Dental implants and craniofacial repair lend itself readily to 3D printing, with the complex topology and need for cosmetically appealing repair schemes. Particularly in craniofacial injury, cosmetic restoration can greatly improve psychosocial abilities, but relies heavily on the surgeon's skill.[273] 3D printing could provide a way to rapidly and accurately repair these cosmetic issues and relieve strain on the surgeon. With accurate representation of anatomic details with relative dimensional differences less than 3 %,[274] mechanical stability,[275] and biocompatibility,[276] 3D-printed titanium implants show promise for custom dental repairs and implants.[277] Proper material and design selections aid in osseointegration and new bone formation, particularly by considering specific patient needs and anatomy of the implant site.[278] In instances of severe head trauma, a two-part technique has been proposed, where a custom mold is fabricated and filled with poly(methyl methacrylate), pressed into large defect areas and completely sterilized prior to surgery.[279] Whether as a guide for bridging-plates to pack with autograft[280] or a directly printed and sintered implant,[281] osseointegration aided by a highly porous, custom-material scaffold is achievable with 3D printing technologies. With the breadth of

applications and methods still under evaluation, one can easily imagine a time where 3D-printed implants are available, and not just in extreme clinical instances. Rapidly analyzing the implant area with radiography, simulating the mechanical loading of the 3D-printed implant digitally to confirm integrity, performing the surgery, and following-up with the patients lays a logical framework for point-of-use implant fabrication, verification, and implantation.[282] Continued development and validation with patients could see wide adoption of custom bone implants, seen to decrease operational time, additional fixtures needed, and complications observed.[283] Layering techniques also allow for replication of human anatomy unachievable through traditional manufacturing, including the use of phase changing substrates.[284] Where orthopedic and dental applications are developed near a point of clinical relevance, soft tissues remain challenging. The complexity of native tissues has led to numerous approaches in efforts to recapitulate native tissues.

3.9 3D Printing to Recapitulate Vascularized and Soft Tissues

Vascular implants and soft tissues present unique challenges, whereby combining strength, flexibility, and cellular compatibility have led to the use of materials which degrade and are replaced by native tissue overtime. A simple, non-degradable approach to mimic an externally visible soft tissue (i.e. non-functional ear) uses radiographs of human anatomy to develop desktop 3D-printed (3DTouch) ABS molds for a two-part cast silicone part.[285] Parts fabricated in this manner were approximately $1/10^{th}$ the cost of a similar 3D-printed and handmade replacement devices of similarly low functionality, providing a visually appealing device restoring cosmetic function.[285] Building complexity, sacrificial layers can be used to hold the shape, where multicomponent inks

can directly place cells or localize bioactivity to direct seeded cell populations.[286] A basic example of this involves a selective laser sintered (EOS P100) PCL carrier seeded with a collagen gel laden with chondrocytes which was successfully implanted as model ears and noses in pigs.[287] However, pairing the specificity of materials and application certainly remains pivotal, where proper material selection encourages neo-tissue formation. A silk bioink formulated with gelatin and glycerol and fabricated with a custom bio-printer was shown to degrade over 3 months, with cellular infiltration and collagen replacing the subcutaneously implanted material in murine models.[288] Keratin patches maintain sufficient structural integrity and cytocompatibility to facilitate cell growth, and has great potential as a DLP (EnvisionTEC) fabricated dermal patch or skin regeneration tool.[289] A Gelatin-GelMA system has successfully been used to repair tympanic membranes in a chinchilla model, where loading the 3D-printed (EnvisionTEC Bioplotter) bioink with epidermal growth factor was seen to improve healing numbers and cell invasion.[290] Using a highly flexible, multiple material extruding printer allowed for the complex model to be fabricated, without the need of post assembly processes other than removing support material. Poly(ethylene glycol) (PEG) diacrylate – alginate co-hydrogels with calcium and UV crosslinking have been proposed to increase the toughness and recovery of hydrogel networks by forming a double crosslinking network, increasing the applicability of otherwise unstable hydrogels within the clinic.[291] Another approach to strengthen 3D-printed hydrogel fibers, without degrading the overall shape or individual fiber, involves a ‘guest-host’ network with adamantane and β-cyclodextrin functionality on hyaluronic acid.[292] The hydrogel rapidly deforms and reforms noncovalent reversible bonds as one hydrogel is extruded into the other and can support

further chemical modification to further improve the bioactivity or functionality.[292] However, the difficulty for these large soft tissues remains in encouraging vascularization to prevent necrosis within the bulk.

To avoid this pitfall, channeling or printing lumens appear as a reasonable approach to improve the diffusivity of the bulk implant and formed neotissue to facilitate nutrient transport.[133] Printing a filament network using a modified RepRap Mendel 3D printer to define vascular lumens with a carbohydrate glass, casting a cell containing ECM, and dissolving the network filaments has showed sustained metabolic function of primary rat hepatocytes.[293] Typically, suppressed function would be exhibited in a bulk gel without network and the alignment of endothelial cells along the open lumens within the bulk demonstrates vascular formation.[293] Drawing these individual filaments to define the location of the vasculature becomes significantly easier when using an extrusion based 3D printing system. Similar work with combinations of GelMA and Pluronic F127[294] and gelatin and collagen[295,296] show the ability to print vascular networks directly, allowing perfusion of the circuit, improved expression of functional mRNA markers over static culture, and cell budding. The challenge remains in creating these kinds of open networks which support complex shapes and networks,[297] and can translate to a wide range of clinical applications: translation from the lab to the clinic remains extremely challenging. Engineering vasculature poses the greatest clinical need in tissue engineering, as without adequate vascularization, any large cell-containing implant will fail from insufficient nutrient exchange.

In addition, vascular issues remain of immense importance with heart disease remaining the leading cause of death in the United States, according to the CDC.[298] Engineered vessels could provide a viable path to help combat this ailment, and other vascular problems, by replacing diseased or damaged vessels with functional, anatomy-matched implants. To help address this, a pericardium-PEG 3D-printed (EnvisionTEC Perfactory 4) hydrogels have been shown to have sufficient strength to form the aortic arch, and reduce inflammatory signaling.[299] Aortic valves from PEG – alginate hydrogels have been also shown to support cell growth and reform tissue, as observed within porcine tissue models.[300] A 3D-printed (EnvisionTEC Perfactory 4) poly(propylene fumarate) vascular graft remained patent for up to 6 months in a mouse model, with initial mechanical properties comparable to the native replacement tissue.[301] For both of these applications, the highly liquidus resin would not have been well suited for an extrusion or sintering based printing. The appeal remains that 3D-printed object can easily replace individual physiology by imaging the defect ahead of the surgery. With promising results seen in animal models, continued work would translate these technologies to human clinical use. Engineered vessels have worked as interim solutions for hemodialysis patients with failing shunts until a transplant organ was available.[302] 3D printing provides a unique pairing of complex geometry with soft resorbable materials and appears to be a viable strategy to solve vascular challenges without permanent implants or xenografts, which cannot remodel as the patient ages and carry concerns of host immune response, infection, and rejection.[303–305]

3.10 3D Printing in Surgery

Several 3D printing applications have moved from development to the clinic. Starting with training physicians, on demand, 3D-printed, anatomic models are becoming more available and increasingly accurate, becoming emphasized in medical school curriculums over anatomic dissection.[306] Using anatomically colored analogues helps alleviate ethical concerns and reduces stress on cadaveric supplies, storage, and medical school financial burden.[307] 3D-printed anatomies generated from CT images are sufficiently accurate (with less than 2 % dimensional variation) to serve as suitable replacements for cadavers for both large (arm) and small (inner ear) anatomies.[307]

Training on combinations of 3D-printed models and cadaveric anatomy can be beneficial for both medical students and practicing physicians. Surgical planning for complex procedures has been revolutionized with 3D printing. Where projected 2D images may be sufficient for simple procedures, instances exist where a 3D model better serves clinicians in determining the most appropriate course of treatment. From complex neck aneurisms,[308] to pediatric cerebrovascular lesions,[309] and complex spine surgeries,[310] 3D printing improves visualization and tactile manipulation of the defects prior to surgery, improving assessments and, reducing surgical time (by approximately 12 % based on matched operations[309]). These guides and tools serve the patients well; 3D-printed fixing aids and packing tools have been shown to improve surgical intervention success.[310] 3D printed devices (Cube 2) have been used to plan the filling of soft tissue voids and design skin grafts, aiming to restore stability to a wound site.[311] Outside the operating theater, forensic models of bone fractures, vessels, and soft tissues for presentation in courtrooms

and classrooms have begun to gain interest, where color choices are used to draw attention to regions of interest.[312]

Certainly, the greatest area of interest for 3D printing related to medical applications remains fabrication of medical devices and implants. With the FDA approval of software to convert radiographs to usable formats for 3D printing, medical device manufacture has begun.[313] As of 2017, the distribution of 510k cleared medical devices is 75 % orthopedic, 13 % surgical, 6 % dental, and the remaining for other applications.[314] However, the great appeal of 3D printing remains the extreme flexibility. FDA approval limits the scope of individual technologies, for good reason, to specific areas of treatment. This does ultimately hamstring the technology and may be why 3D-printed devices remain most prevalent in the research realm and extreme clinical situations. Even with the rigors associated with FDA approval, the benefits of bringing patient-tailored devices to market should exceed the costs of narrowed applications. A likely niche that meets these requirements is on-demand surgical tools, which have already been shown to have sufficient mechanical integrity to compete with traditional stainless steel tools at $1/10^{th}$ the cost.[315] Manufacturing surgical tools within a sterile environment would negate the need for secondary sterilization and help to provide rapid access to surgical tools in the developing world.[315]

3.11 Conclusions

3D printing has rapidly moved from a fabrication novelty to a ubiquitous manufacturing technique for biomedical applications. Though there remain many challenges for general acceptance, such as validation and repeatability, milestones within the 3D printing

revolution have been reached. A future where medical technology manufacturers' work closely with additive manufacturing centers and hospitals to answer various biomedical questions and solve numerous clinical problems that are otherwise difficult to decipher. As an acellular technique, 3D-printed implants and scaffolds show promise to increase the biomimicry of culture surfaces, creating specific objects for targeted problems. As a technique to study single cells, large cell populations, and organoids, 3D printing is unparalleled in its proven flexibility to investigate cell interactions across size scales. Overall, continued investigation into 3D printing technology and applications will only see improvements in clinical and research objectives.

Chapter 4: Development of Surface Functionalization Strategies for 3D-Printed Polystyrene Constructs[iii]

4.1 Introduction

Linking together surface chemistry, material properties, and biological response provides a viable path to translating 2D *in vitro* culture surfaces to 3D scaffolds. This builds *in vitro* surfaces to mimic tissue niches through protein adhesion, cell patterning, and guiding differentiation to sequester cells and generate functional tissues.[316,317] However, the applications of 3D-printed PS as a cell-contacting growth surface have been limited.[318] The combination of 3D printing and surface chemical modification provides the potential for a highly tunable process to select culture environments for select cell types. Directed surface modification has been shown to influence human mesenchymal stem cell (hMSC) differentiation, but further exploration would fully develop the link between surface chemical cues and cell phenotype.[319] Fibronectin and integrins have been seen to associate preferentially with carbonyl and amine containing surfaces.[320] Surface wettability influences the adhesive force between proteins and the substrate, resulting in conformational changes at the interface[321] which can be sensed by adhered cells and influences spreading and proliferation.[108] Building surface properties to selectively elicit and pattern protein adhesion provides a viable path to engineering cell-material interactions.[322–324]

[iii] Adapted and reprinted with permission from: MJ Lerman, S Muramoto, N Arumugasaamy, M Van Order, J Lembong, AG Gerald, G Gillen, and JP Fisher. Development of Surface Functionalization Strategies for 3D-Printed Polystyrene. Journal of Biomedical Materials Research Part B: Applied Biomaterials. 2019, (1)

The main objective presented in this chapter explores engineering surface chemistry for 3D-printed PS scaffolds to target hMSC expansion. First, we sought to establish the surface characteristics generated by our plasma system. Next, we determined the link between surface properties and protein adhesion. Then, we investigated hMSC spreading, growth, and ECM expression on the surfaces and ultimately show the concept translates to a 3D model. We demonstrate that carbonyls on moderately hydrophilic surfaces help to promote hMSC proliferation and phenotype maintenance, likely through associated surface ECM proteins expressed by the cells and deposited from media. These strategies present a viable 3D PS scaffold capable of supporting hMSC expansion with wide applicability.

4.2 Materials and Methods

4.2.1 2D Substrate Preparation

Silicon wafers were wiped clean with ethanol (EtOH), sonicated for 5 min in acetone, then methanol, and dried with nitrogen. 10 % (w/w) PS (> 50,000 molecular weight atactic flakes, Polysciences, Inc., Warrington, PA)/Toluene was spun cast at 314.2 rad/s (3000 RPM) for 40 s with a spin coater. These samples were used for surface characterization. For cell and protein analyses, cover glass slides were wiped clean with EtOH and coated 10 % PS solution following the same spin casting method.

4.2.2 Surface Activation

A low temperature plasma activated samples by creating a dielectric barrier discharge (DBD) in a 4 mm ID glass capillary tube attached to a 20 kHz AC high voltage source

(Fig. 1A). Ultrapure helium was used as a discharge gas with acetonitrile vapor or oxygen added at a concentration of 2.5% (v/v). Ignition frequency was visually tuned with the lowest power selected achieving uniform and consistent plasma ignition and to avoid thermal damage to surfaces (0.14 kV to 0.34 kV). Samples were translated under the plasma jet with servo motors. For 3D-printed objects, each side was exposed to plasma treatment. Sample characterization and use in cell studies were generally performed at least a day after treatments, with samples generated at the same time generally used in subsequent studies.

4.2.3 Goniometer wettability measurements (water contact angle)

2 μL of deionized water was dispensed onto leveled samples with an inverted syringe pump. A video camera recorded the pendant droplet touching and stabilizing on the surface. The baseline water-surface interface was determined and contact angle measured on at least 3 drops.

4.2.4 X-ray photoelectron spectroscopy (XPS)

Quantitative XPS measurements determined elemental compositions with a survey scan (0 eV to 1100 eV), a pass energy of 160 eV, and resolution of 1.0 eV. The binding stoichiometry was determined from high-resolution scans with a pass energy of 40 eV and resolution of 0.1 eV and deconvolving the peak into its components based on overall shape. A Gaussian-Lorentzian distribution was used for peak fitting, with a full width at half maximum constraint of approximately 1.7 eV on 6 spectra per sample. Charging was accounted for by a low energy electron flood-gun with a filament current of 1.8A and

charge bias of 2.5V. Differential charging on the surface was not suspected based on a lack of significant peak broadening.

4.2.5 Total protein determination

Samples were covered in fetal bovine serum (FBS) for 1 hour at 37 °C, then rinsed with phosphate-buffered saline (PBS), placed on ice, and covered with cold radioimmunoprecipiration assay (RIPA) buffer for 5 min. Isolated protein was centrifuged at 14,000 g for 15 min at 4 °C. The supernatant was tested on 3 samples in technical triplicate with a Pierce BCA Protein Assay following standard microplate procedures.

4.2.6 Polyacrylamide gel electrophoresis protein separation and Coomassie staining

Protein was isolated following the methods explained above with Halt Protease Inhibitor (ThermoFisher, Waltham, MA) added to RIPA, including a 1:100 FBS:RIPA control. Mini-Protean TGX (Bio-Rad, Hercules, CA) gels were loaded with Laemmli buffer and samples, as described.[299] Gels were run for 45 min at 120 V in 1X Tris-Glycine buffer and fixed in 5 % acetic acid, 45 % deionized distilled water (ddH_2O, >18.2 MΩ resistivity), and 50 % methanol for 30 min. Gels were washed 3 times for 5-min in ddH_2O with protein bands visualized and imaged with Coomassie blue.

4.2.7 Proteomics through mass spectrometry (MS)

Protein was isolated through electrophoresis, as described. Gel lanes were separated, cut into 10 equal pieces, digested with sequencing grade trypsin, and peptides extracted with

acetonitrile-formic acid buffer.[325] Liquid-Chromatography (LC)-MS/MS was performed using a nano-LC system (Easy nLC1000) connected to Q Exactive mass spectrometer (ThermoFisher). Peptides were eluted at 300 nL/min using a series of linear gradients of acetonitrile in 0.1 % formic acid. Data sets were searched against UniProt human database using MaxQuant software (version 1.5.5.1).[326] Groups with peptide counts less than the total number of test groups (6), non-species, or obvious contaminants were eliminated.

4.2.8 Cell culture practices

hMSCs (RoosterBio, Frederick, MD) were thawed and expanded in Dulbecco's Modified Eagle Medium with 10 % fetal bovine serum, MEM non-essential amino acids 0.1 mmol/L, and penicillin (100 U/mL) - streptomycin (100 µg/mL) (growth media). 90 % confluent hMSCs were washed with pH 7.4 PBS and lifted with 0.25 % trypsin-EDTA and neutralized with growth media. Passage 2-4 hMSCs were used during experiments, with cells treated as passage 1 upon receipt. 50,000 hMSCs per at least 20 minute UV sterilized sample were used unless noted. Cell counting was accomplished using the Trypan Blue exclusion method with a hemocytometer.

4.2.9 Confocal imaging and image processing

Cells were lifted as described and resuspended in the media of interest (growth media or RoosterBio High-Performance Basal Media (No Serum Media). hMSCs were seeded onto surfaces and grown overnight. Cytochalasin-D treated hMSCs had their media replaced with growth media containing 10 µmol/L cytochalasin-D for 1 hour prior to fixing.[26,327–329] Samples were chemically fixed using 4 % formaldehyde and 1 % sucrose

solution and permeabilized with a 300 mmol/L sucrose, 50 mmol/L sodium chloride, 6 mmol/L magnesium chloride, 20 mmol/L HEPES, and 0.5 % Triton-X-100 solution. Actin was stained with 2.5 % AlexaFluor 594 Phalloidin in PBS, counterstained diamidino-2-phenylindole (DAPI) or VectaSheild (Vector Labs, Burlingame, CA). A confocal microscope (SP5 X, Leica Microsystems, Buffalo Grove, IL) captured Z-stack images, which were processed with a MATLAB (MathWorks, Natick, MA) program. The program read in image files from the specified directory, and separated the image stacks into individual image locations (i.e. groups of individual z-stacks). Small debris and background fluorescence were eliminated with size and intensity exclusion thresholds. For each image stack, the average spread area was calculated by dividing the total area covered by phalloidin (red channel) by the number of detected nuclei (blue channel). Running this process for each stack was used to generate statistics (Appendix).

4.2.10 Flow cytometry

hMSCs were seeded as described and grown for 6 days, with media replaced on the 3rd day. Cells were lifted with StemPro Accutase (ThermoFisher), diluted with an equal volume of growth media, and resuspended in 1 % FBS in PBS (flow buffer). To stain, a PE Negative Cocktail (CD45, CD34, CD11b, CD19, and HLA-DR) and Positive Cocktail (FITC CD90, PerCP-Cy 5.5 CD105, and APC CD73) from a Human MSC Analysis kit (BD Biosciences, Franklin Lakes, NJ) was used, following manufacturer's recommendations. hMSC Isotype controls were run and UltraComp eBeads (ThermoFisher) single color controls were used for compensation. Data collection was performed on a FACS Canto II (BD Biosciences) and analysis performed with Cytobank Community software (Cytobank Inc. Santa Clara, CA).

4.2.11 DNA quantification

Cells were dissociated from 3 samples with Trypsin and 0.25 % EDTA and resuspended in PBS. DNA was isolated following the procedures for DNeasy Blood & Tissue Kit (Qiagen, Hilden, Germany) and quantified in technical triplicate using a Quant-iT PicoGreen (ThermoFisher) kit, following the manufacture's protocol. Fluorescence measurements were read on a M5 SpectraMax plate reader (Molecular Devices, San Jose, CA) with an excitation wavelength of 490 nm and emission read at 538 nm.

4.2.12 RT-PCR

RNA was isolated with a Trizol phase separation technique. Samples were covered with Trizol, gently mixed and transferred to a microcentrifuge tube. Chloroform was added and vigorously mixed. Phase layers were separated by centrifugation at 12,000 g for 15 min at 4 °C, with the aqueous phase transferred. 70 % EtOH was added to 35 % of the final volume. Samples were transferred to an RNeasy mini column (Qiagen). Complete RNA isolation followed kit instructions. cDNA conversion was completed using a High Capacity cDNA Archive Kit (ThermoFisher) following manufacturers procedures. A ΔΔCT gene expression assay was completed, comparing genes of interest to GAPDH (endogenous control). A 7900HT RT-PCR system (Applied Biosystems, Foster City, CA) cycled samples: 2 min at 50 °C, 10 min at 95 °C, 40 cycles of 15 sec at 95 °C, and 1 min at 60 °C.

4.2.13 3D scaffold fabrication

A 3D Bioplotter (EnvisionTEC GmbH, Gladbeck, Germany) fabricated scaffolds. A sugar-glass support material (EnvisionTEC GmbH) was heated to 150 °C and extruded

through a 0.3 mm ID needle tip at 70 - 80 kPa at 10 - 30 mm/s. The PS was melted at 155 °C and extruded through a 0.4 mm ID needle tip at 900 kPa at 3 – 5 mm/s. The build surface was maintained at 60 °C. The extrusion temperature of the PS is below the thermal decomposition temperature of the material (around 163 °C[151]) to avoid degradation of the material. At the completion of prints, the support was removed with ddH_2O, scaffolds washed overnight in ddH_2O, cleaned in 100 % EtOH for 30 min, and air dried. With these washing procedures, we believe the support material was solubilized following printing and not present during later cell studies.

4.2.14 Scanning electron microscopy (SEM)

A FEI Quanta 200 FEG-ESEM (Hillsboro, OR) was used to image PS scaffolds under high vacuum at 5.0 keV. Samples were coated with Au-Pd prior to imaging to reduce charging artifacts.

4.2.15 Gel permeation chromatography (GPC)

The molecular weight of printed and stock PS was determined by GPC (Waters Alliance Separations Module e2695, Waters 2414 Refractive Index Detector, and Waters HSPgel columns in series (HR MB-L and HR 3.0 columns, 6.0 mm ID × 15 cm, Waters, Milford, MA). Three samples of each were dissolved in tetrahydrofuran with molecular weight (g/mol) determined against polystyrene standards in at least technical duplicate.

4.2.16 Differential scanning calorimetry (DSC)

The glass transition temperature was determined by measuring the thermal energy change as a function of temperature change with a TA DSC Q100 (TA Instruments, New Castle, DE). Three approximately 10 mg samples of printed and stock PS were sealed in

hermetic aluminum pans. Samples were rapidly equilibrated at 160 °C and kept isothermal for 5 min. The temperature was ramped at 10 °C per min to −20 °C and back to 160 °C and heat flow recorded.

4.2.17 Statistical analysis

Statistical significance was determined through a one-way two-sided ANOVA at the 95% confidence interval using the Games-Howell comparison method in Minitab 18 (Minitab, Inc. State College, PA) unless noted.

4.3 Results

4.3.1 Surface characterization of 2D treated surfaces

In this work, we sought to develop a surface modification method which facilitates hMSC adhesion and growth on custom PS scaffolds. This work was performed on 2D surfaces to validate our method. Wettability analysis (Figure 4.1 B, C) shows that treated surfaces experience a significant increase in wettability as compared to the no treatment (NT) control (92.3º). 2.5 % oxygen (O_2) and 2.5 % acetonitrile (ACN) plasmas reduced contact angles to 54.6º and 26.4º respectively, while TCPS surfaces maintained a native contact angle of 50.0° ($p < 0.05$). With contact angle measurements performed at least a day following treatment, we suspect contact angles would have stabilized by the time measurements were taken. Further surface characterization, accomplished through XPS, confirmed the NT surface as primarily carbon containing, with moderate oxygen and little nitrogen content observed in TCPS (Figure 4.1 D). Nitrogen incorporation in O_2 and He surfaces were similar ($p < 0.05$). Total oxygen incorporation was similar in TCPS, 100 % helium plasma (He), and O_2 plasma treated samples, followed by ACN. ACN

treated samples had much greater nitrogen incorporation ($p < 0.05$). Specific bonding stoichiometry indicate that oxygen present in He and O_2 treated surfaces contained both single-bonded oxygen and carbonyl groups (Figure 4.1 E, Table 4.1). The carbonyl content of He and O_2 treated surfaces exceeded, though not statistically different, the quantities present in TCPS ($p > 0.05$). ACN treated surfaces contained the greatest quantity of single and double bonded oxygen, as well as potential surface amines groups and malononitrile ($p < 0.05$).

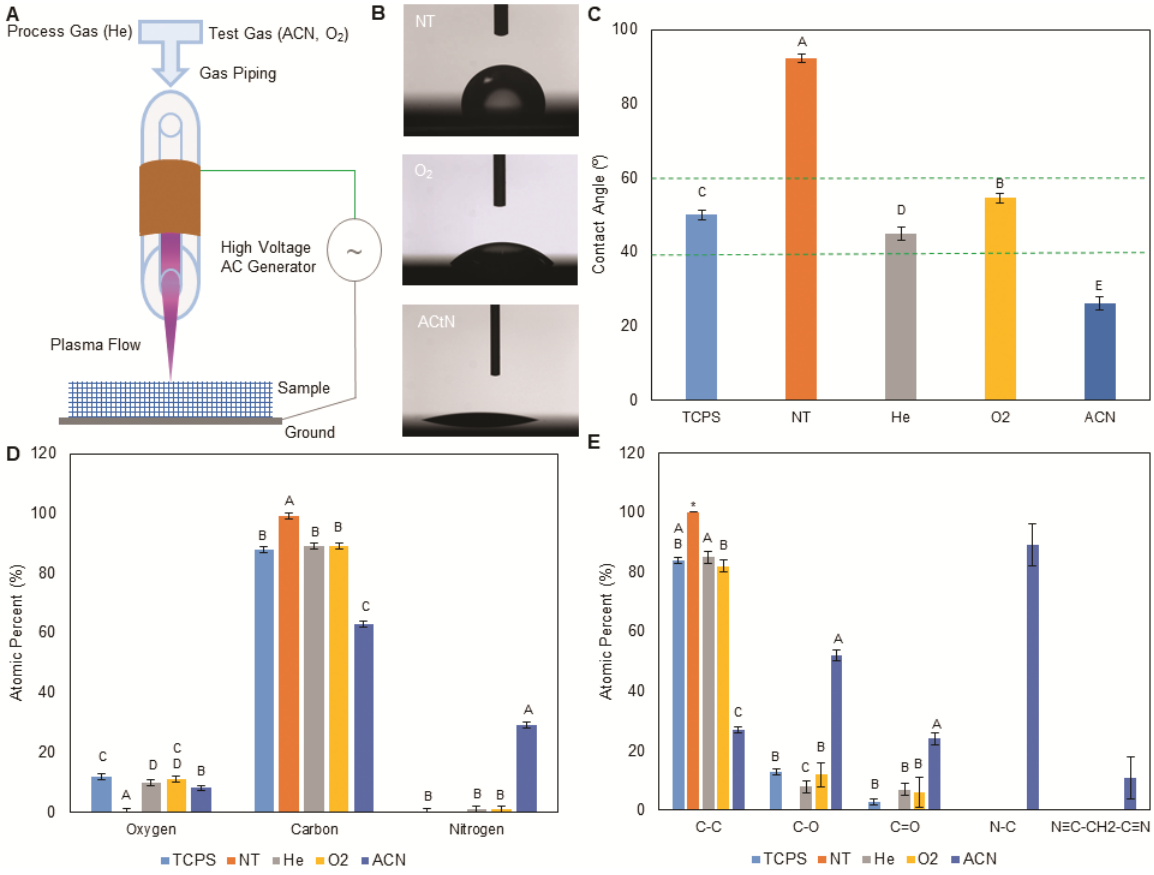

Figure 4.1 Characterization of DBD treated surfaces. A) Diagram of the DBD system with plasma flowing over the sample. B) Example contact angle images of the NT, O_2 and ACN treated surfaces. C) Quantified contact angles. Activating the surfaces with He, O_2, and ACN reduced contact angles. Groups with different letters indicate statistical difference ($p < 0.05$), data is shown as mean ± standard deviation, n = 5. D) Survey XPS data shows surface oxygen and nitrogen presence on the DBD treated surfaces and TCPS and nitrogen on the DBD treated surfaces. Nitrogen presence in the DBD surfaces is likely a by-product of plasma treatment in ambient atmosphere. The greatest nitrogen presence was seen on the ACN treated surfaces. Oxygen and nitrogen presence were accompanied by a reduction in carbon. E) High-Resolution DBD treated surfaces showed single bonded oxygen, and carbonyl groups. TCPS showed both single bonded oxygen and carbonyl groups. NT surfaces remained purely carbon. Nitrogen presence on the ACN treated surfaces were primarily bound to carbon as imine groups, with 13 % of nitrogen on the surface was present as malononitrile. XPS Data is shown as mean ± standard deviation, 6 scans per sample, single sample for NT, ACN, TCPS, two samples for He, O_2. Groups with different letters indicate statistical difference, asterisk indicates identical values (Tukey multiple comparison, $p < 0.05$).

Table 4.1 XPS compositional analysis. The survey scan shows the elemental distribution of the surface in percent atomic composition, while the high-resolution scan shows the chemical states for the elements carbon and nitrogen. Data is shown as mean ± standard deviation. *Imine (R=N-R) where R is aromatic, **Malononitrile (N≡C-CH2-C≡N)

	Survey Scan			High Resolution Scan				
	O 1s	**C 1s**	**N 1s**	**285.3 C-C**	**286.4 C-O**	**287.6 C=O**	**397.9 N-R***	**402.4 Malo****
NT	0 ± 1	99 ± 1	-	100	-	-	-	-
ACN	8 ± 1	63 ± 1	29 ± 1	27 ± 1	52 ± 2	24 ± 2	89 ± 7	11 ± 7
TCPS	12 ± 1	88 ± 1	0 ± 1	84 ± 1	13 ± 1	3 ± 1	-	-
O_2	11 ± 1	89 ± 1	1 ± 1	82 ± 2	12 ± 4	6 ± 5	-	-
He	10 ± 1	89 ± 1	1 ± 1	85 ± 2	8 ± 2	7 ± 2	-	-

4.3.2 Characterization of adhered surface protein

The contact angle decreased relative to initial values following serum exposure, and was statistically similar across all surfaces, except for ACN treated surfaces (Figure 4.2 A). ACN treated surfaces were observed to have an increase in contact angle. All contact angle changes were statistically different from initial values (two sample t-test, $p < 0.001$ for all test surfaces at the 95 % confidence interval). A Pierce BCA analysis revealed O_2 treated samples were the only group to contain a statistically greater quantity of adhered protein relative to the NT control, but no different from the other surfaces ($p < 0.05$, Figure 4.2 B). Coomassie staining confirmed the adhered protein quantities similarities, where the darker bands of the O_2 and TCPS treated samples indicate greater protein presence (Figure 4.2 C). Additionally, darker high-molecular weight bands appear present in these samples. To better quantify protein differences, mass spectrometry was performed on the PAGE gel separated proteins. The proteins have been grouped by family type and the top 10 protein families present ranked (Figure 4.3). Based on peptide counts (e.g., instances of matching protein fragments), O_2 treated surfaces tend to associate better with 1) proteins generally, attracting more and a wider variety and 2) greater relative amounts of ECM proteins (23.1 % of O_2, 19.7 % of TCPS, 14.8 % of NT, 11.5 % of He, 10.8 % of FBS, and 5.1 % of ACN). Specifically, collagen family proteins were only found to be a top 10 present protein by peptide count in the O_2 (#6, 3.6 %) surfaces and TCPS surfaces (#10, 3.0 %). These both represent a greater fraction than in the diluted FBS control (#10, 2.6 %).

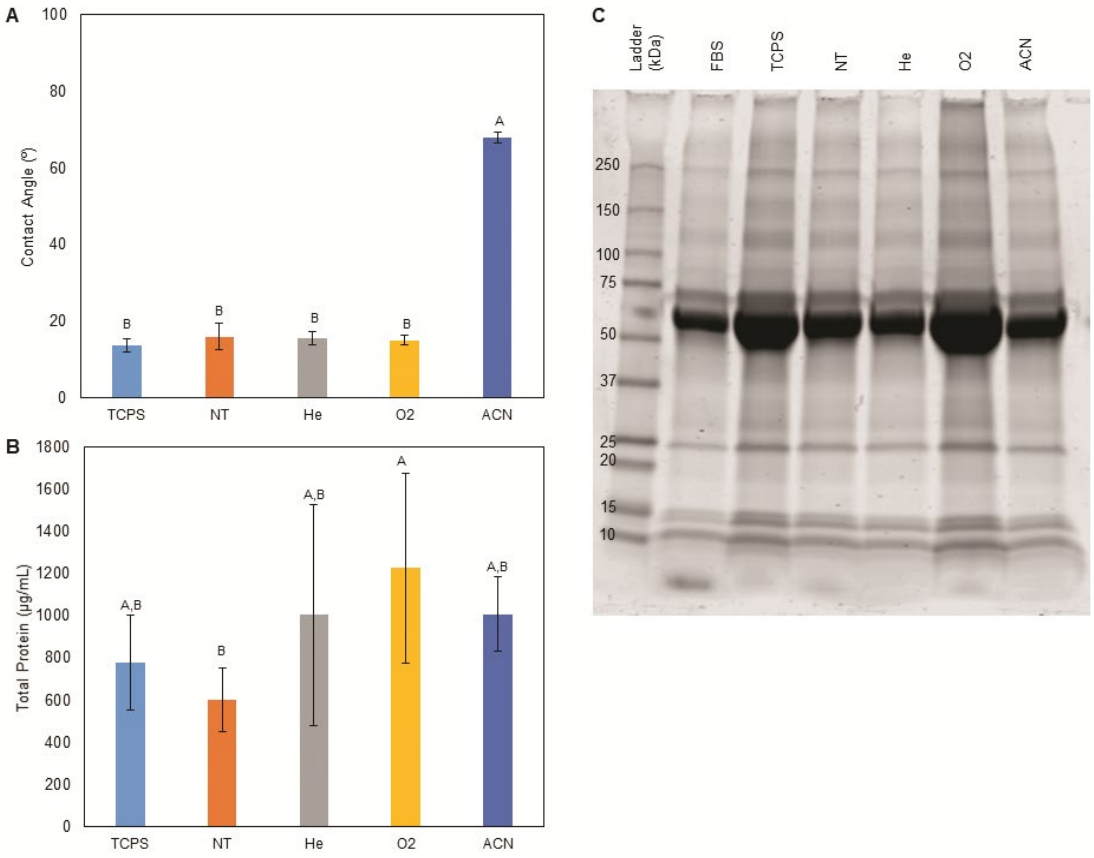

Figure 4.2 Protein effects on DBD treated surfaces. A) Quantified contact angles across the surfaces following serum exposure Contact angles were reduced for all surfaces except on ACN treated surfaces. This indicates increased surface wettability and surface energy following exposure to serum. Groups with different letters indicate statistical difference ($p < 0.05$), data is shown as mean ± standard deviation, n = 5 except TCPS n = 4, ACN n = 3. B) Total protein content following coating. O_2 surfaces showed statistically greater protein adhesion than the NT surface, but no different from any other surface. Data is shown as mean ± standard deviation, n = 3. C) Coomassie stained gel. Visually, the O_2 surface band appears darker than the NT surface across the whole lane. Similar bands are observed across all treatment samples and the source serum.

A

Top 10 Families Per Group

FBS	TCPS	NT	He	O_2	ACN
Serotransferrin (13.5%)	Complement Factor (10.5%)	Serotransferrin (11.2%)	Serotransferrin (15.5%)	Complement Factor (9.3%)	Serotransferrin (15.3%)
BSA (10.5%)	Serotransferrin (9.6%)	Serpin (9.5)%	BSA (11.0%)	Serpin (7.6%)	BSA (14.0%)
Serpin (10.0%)	Serpin (7.8%)	Complement Factor (9.1%)	Serpin (9.0%)	Serotransferrin (7.0%)	Serpin (10.9%)
Complement Factor (8.8%)	BSA (5.3%)	BSA (7.6%)	Complement Factor (8.2%)	Apolipoprotein (5.0%)	Complement Factor (7.4%)
Glycoprotein (5.7%)	ITIH Protein (5.0%)	ITIH Protein (4.2%)	Macroglobulin (4.9%)	ITIH Protein (4.9%)	Glycoprotein (4.6%)
ITIH Protein (3.5%)	Apolipoprotein (3.8%)	Glycoprotein (4.2%)	ITIH Protein (4.5%)	Collagen (3.6%)	Antiproteinase (4.5%)
Antiproteinase (3.4%)	Macroglobulin (3.5%)	Macroglobulin (3.4%)	Glycoprotein (4.4%)	BSA (3.5%)	Kininogen (3.9%)
Fetoprotein (3.1%)	Glycoprotein (3.4%)	Apolipoprotein (3.3%)	Apolipoprotein (3.2%)	Macroglobulin (3.5%)	Vitamin D-Binding Protein (3.7%)
Vitamin D-Binding Protein (2.8%)	Coagulation Factor (3.2%)	Antiproteinase (2.5%)	Coagulation Factor (3.1%)	Coagulation Factor (2.9%)	Fetoprotein (3.6%)
Collagen (2.6%)	Collagen (3.0%)	Hemoglobin (2.5%)	Fetoprotein (3.0%)	Glycoprotein (2.7%)	Hemoglobin (3.4%)
Other (36.2%)	Other (45.0%)	Other (42.7%)	Other (33.3%)	Other (50.0%)	Other (28.7%)
ECM (10.8%)	ECM (19.7%)	ECM (14.8%)	ECM (11.5%)	ECM (23.1%)	ECM (5.1)

B

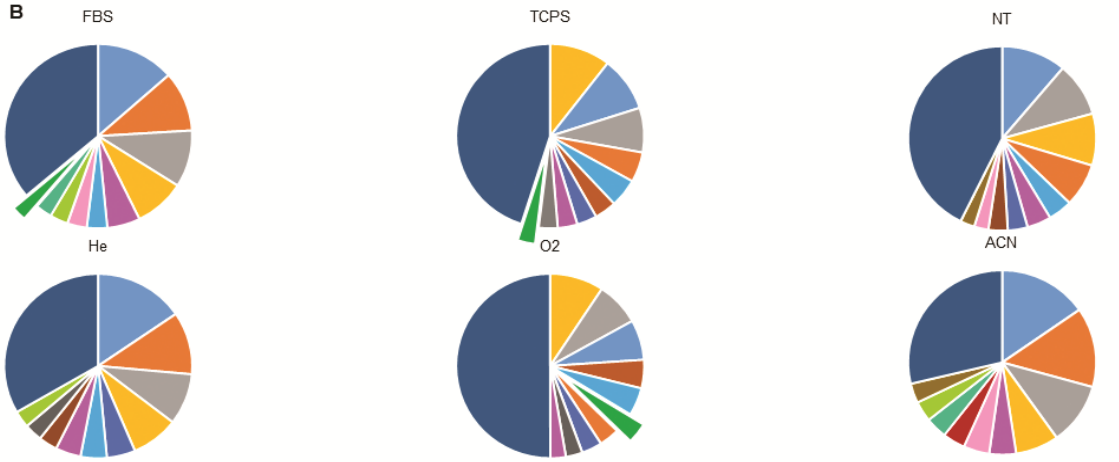

Figure 4.3 Adhered protein composition on DBD treated surfaces. A) Table showing the top ten proteins present by peptide count, grouped by identified protein family. ECM proteins are called out separately and represent percent of total peptides counted. Collagen was only present in the top ten for FBS, TCPS, and O_2, indicating a possible correlation between carbonyls on surfaces and ECM protein association. Conversely, ACN surfaces had the lowest percentage of ECM proteins present. B) Graphical representation of the percentages of counted peptides. Colors in figures match those in the table for each group.

4.3.3 Cellular interaction with surfaces

Surfaces containing the highest quantities of carbonyl-groups tended to facilitate the greatest spreading (Figure 4.4). Protein containing media and coating the surfaces with media increased cell spreading, while the use of a serum-free media and an actin inhibitor (cytochalasin-D) reduced cell spreading. NT surfaces tended to prevent cellular spreading, where cells remained rounded. Quantified hMSC phenotype (Table 4.2) shows that the cells generally expressed (>95 %) of the positive markers and lacked expression of negative markers (83 to 90 %). O_2 treated samples exhibited the highest amount of phenotypically expected hMSCs. To contrast this, He treated samples, with lower wettability and similar oxygen content, exhibited higher ratios of hMSCs expressing the differentiation markers in the Negative Cocktail Mix. The ACN treated surfaces showed decreases in the positive and negative markers.

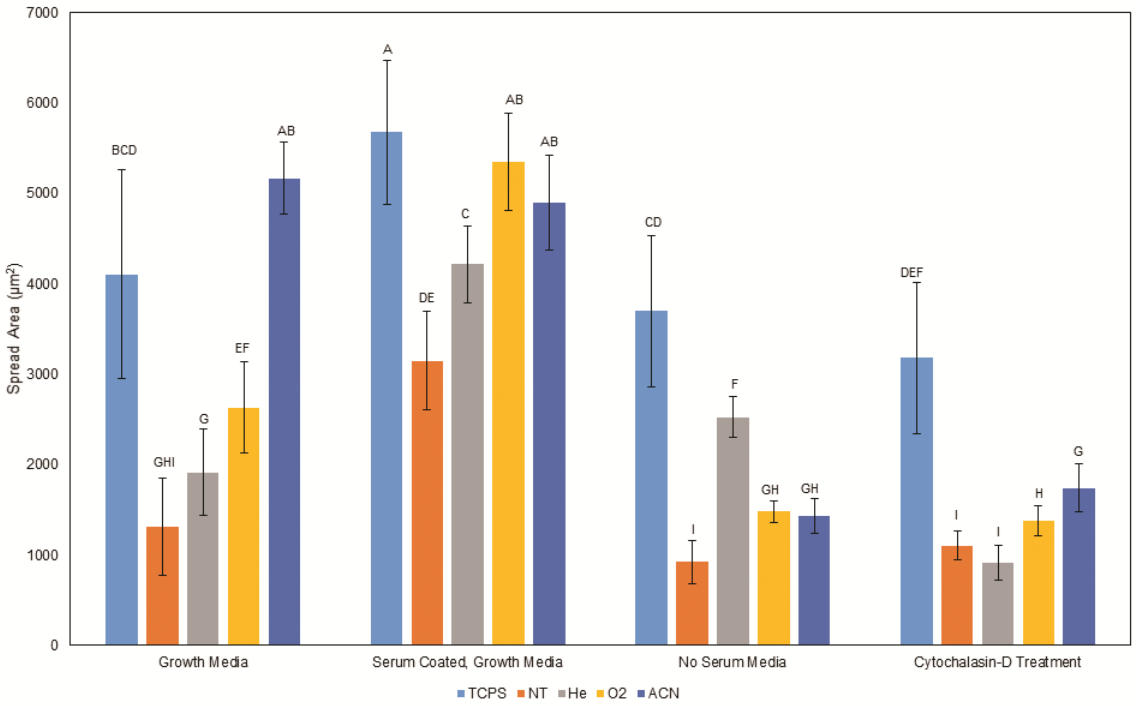

Figure 4.4 Average spread area of hMSCs on treated surfaces in various media. The data indicates that proteins tend to associate with the carbonyl containing surfaces, facilitating cell spreading through an actin-related mechanism. Surfaces pre-coated with serum generally had greater spread areas, where media lacking protein showed less spread cells. The addition of cytochalasin-D, an actin inhibitor, to the media prior to imaging generally reduced spread area of the hMSCs. Note: ANOVA was performed over the whole dataset, groups with different letters indicate statistical difference ($p < 0.05$), is shown as mean ± standard deviation, n = 16 except NT cytochalasin-D treatment, n = 15.

Table 4.2 hMSC phenotype assessment through flow cytometry. Carbonyl containing surfaces tended to have greater percentages of hMSCs displaying expected surface markers, where ACN treated surfaces tended to have reduce the percentage of expected phenotype hMSCs.

Condition	% CD90 (+)	% CD73 (+)	% CD105 (+)	% Negative (-)
TCPS	94.8	95.5	96.1	83.3
NT	97.9	97.3	95.3	84.0
He	99.4	98.4	98.3	74.3
O2	94.1	97.2	95.6	89.9
ACN	74.4	73.2	80.5	58.5

4.3.4 Cellular response to 2D surfaces

DNA quantification showed significantly higher growth (DNA fold change) after 6 days (Figure 4.5 A). The He and O_2 treated surfaces showed the greatest increase in DNA, followed by treatment with ACN ($p < 0.05$). PCR showed similar collagen I (Figure 4.5 B) and fibronectin (Figure 4.5 C) mRNA expression of hMSCs attached to the plasma treated samples and TCPS over the course of 6 days. Expression levels were significantly greater than on the NT surface (collagen I, expression on the NT surface was inconclusive, $p < 0.05$). As well, CD29 (Figure 4.5 D) expression was significantly greater from hMSCs on the treated surfaces relative to the NT surfaces (except for He, where expression was inconclusive $p < 0.05$).

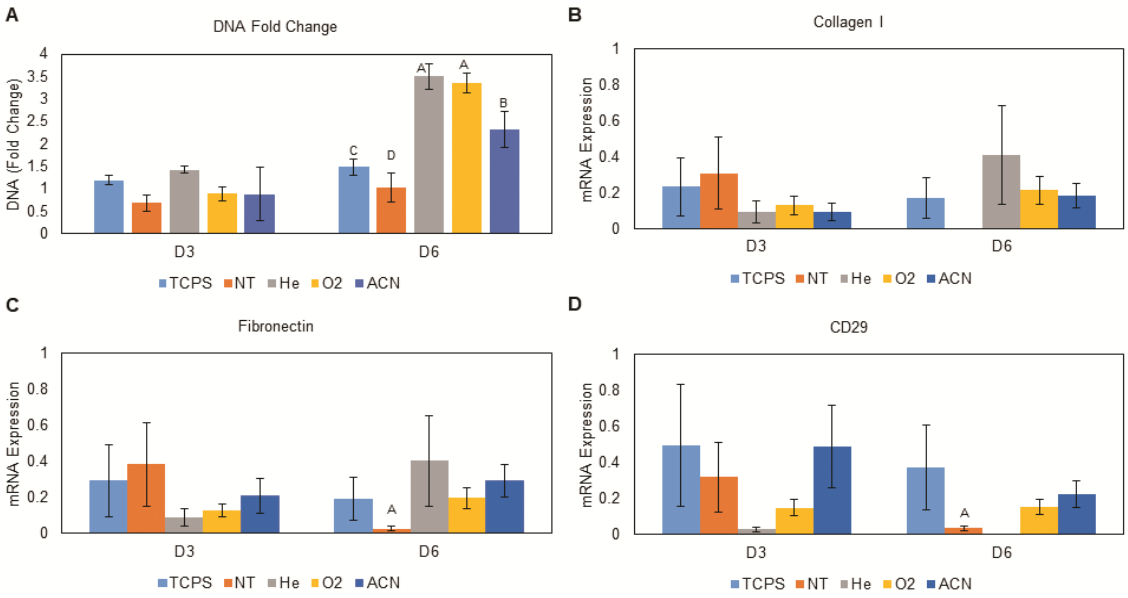

Figure 4.5 hMSC growth and ECM marker expression on DBD treated surfaces. A) Normalized DNA content to each D0 value. The He and O_2 surfaces showed the greatest DNA content fold change, followed by ACN, TCPS, and NT surfaces. This indicates surface activation successfully facilitated hMSC proliferation. Data is shown as mean ± standard deviation, n = 3. B) mRNA expression of collagen I. All surfaces showed detectable expression except for the NT surface. C) mRNA expression of fibronectin. All surfaces showed greater expression than the NT surface on day 6. D) mRNA expression of CD29. All surfaces showed detectable expression except for the He surface. Statistically greater expression was seen on TCPS, O_2 and ACN surfaces compared to the NT surface at day 6. For ΔΔCT mRNA expression, depressed expression on the NT surface at day 6 may indicate reduced ability to modify the surrounding environment and express ECM proteins, likely related to the underlying protein content directed by the surface chemistry. Note: Groups with different letters indicate statistical difference ($p < 0.05$) for ANOVA was performed on each time point. For figures B, C, and D data is in technical triplicate and displayed as mean ± standard deviation.

4.3.5 Translation of results to 3D model

To explore the applicability of this method on 3D-printed PS, we developed a method for extrusion deposition modeling of polystyrene without thermally degrading the polymer (Figure 4.6 A). Scaffolds with 90° (Figure 4.6 B) 60° (Figure 4.6 C), and 85.5° (Figure 4.6 D) rotations between individual layers were printed. SEM imaging of the 90° matching demonstrates open internal pore structure (Figure 4.6 E). When the 85.5° surface was treated with the O_2 plasma, hMSCs adhered and spread within the scaffolds. At 3 days, hMSCs were observed to bridge fibers (Figure 4.6 F) and remained spread on fibers with expected morphology after 6 days (Figure 4.6 G). hMSC seeded at 5,000 cells/cm^2 continued to expand in static culture up to 7 days (two sample t-test p value between NT and O_2 scaffolds = 0.011, Figure 4.6 H). No differences in glass transition temperature (two sample t-test, p = 0.212, Figure 4.6 I), high or low fraction molecular weights (two sample t-test, p = 0.825, 0.210, Figure 4.6 J, K), or molecular weight area fractions (two sample t-test p = 0.905, Table 4.3) were observed between the printed and stock material, indicating our method did not thermally degrade the material during extrusion.

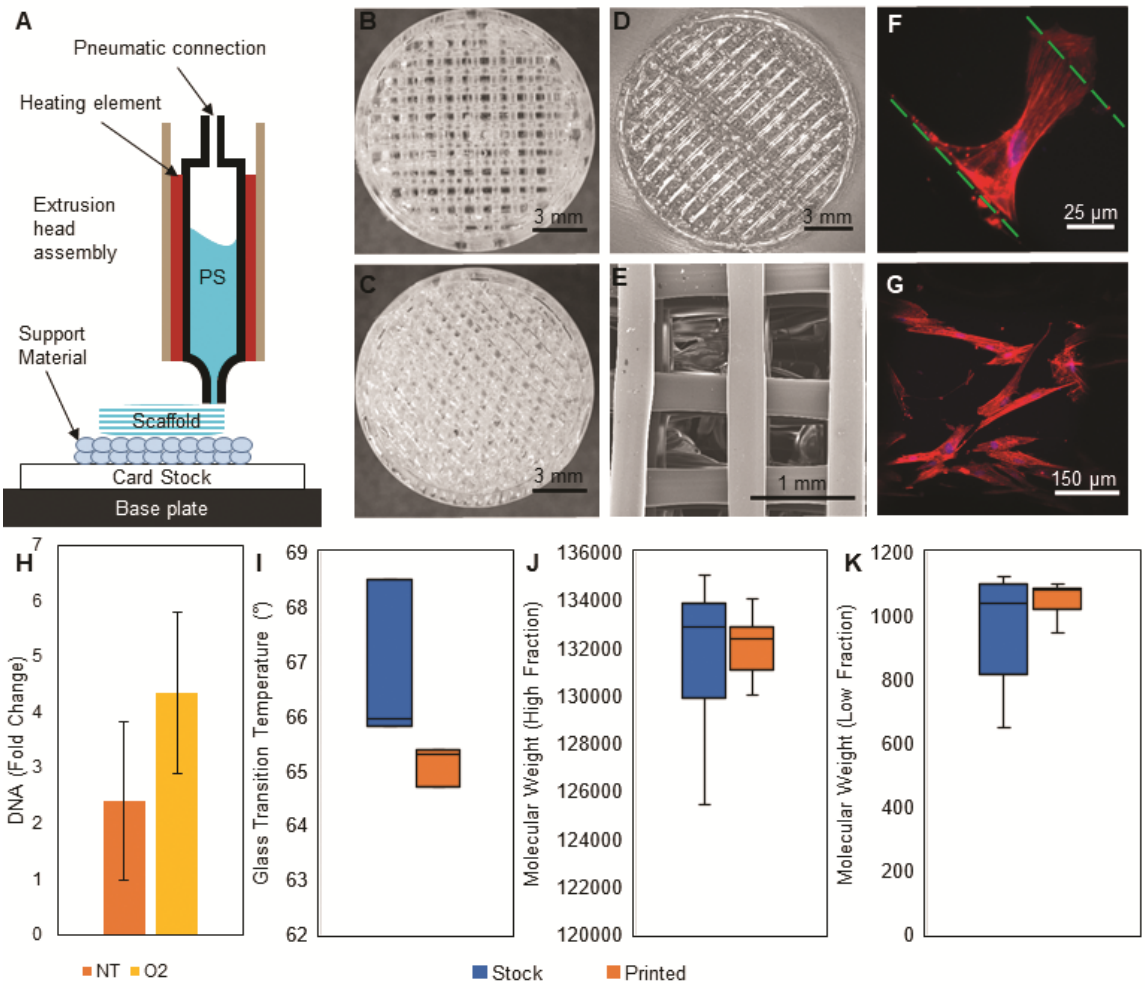

Figure 4.6 3D printing method supports flexible fabrication and hMSC growth. A) 3D printing method schematic: card stock is placed onto the temperature controlled base plate with the support material printed on top. The extrusion head is then replaced with PS extruded onto the support material. 3D-printed PS scaffolds with layer offset angles of B) 90°, C) 60°, and D) 85.5°. E) A SEM image of the 90° inner geometry of the PS scaffold. F) A single hMSC is seen bridging two PS fibers in an 85.5° scaffold at 3 days. Green lines indicate the edges of the PS fibers, DNA is stained blue with DAPI, and F-actin is stained red with phalloidin. G) hMSCs on an 85.5° scaffold display expected morphology on a O_2 treated scaffold at 6 days. The image is a projected z-stack over the curved surface of a single PS fiber. DNA is stained blue with DAPI and F-actin is stained red with phalloidin. H) DNA Fold change from day 0 after seven days of growth. hMSCs initially seeded at 5,000 cells/cm^2. Trends indicate that the 85.5° scaffold O_2 scaffold supports hMSC growth throughout the scaffold and warrants further development. ($p = 0.011$, data shown as mean ± standard deviation, $n = 3$). Matching batches of source (stock) and extruded (printed) material were evaluated for the occurrence of degradation during printing. I) Differential scanning calorimetry determined no difference ($p = 0.212$) in the glass transition temperature ($n = 3$). J) High molecular weight fraction and K) Low molecular weight fraction of stock and printed polystyrene as determined by gel permeation chromatography. ($n = 3$) samples were run against a standard curve to determine molecular weight. No difference was found between high ($p = 0.825$) and low ($p = 0.210$) fractions of the stock or printed material.

Table 4.3 Area fractions molecular weight peaks. No difference between the relative quantity in each group was observed ($p = 0.905$).

	Stock (%)	Printed (%)
High Fraction	33.5 ± 0.2	33.5 ± 0.5
Low Fraction	66.5 ± 0.2	66.5 ± 0.5

4.4 Discussion

Our first goal was to decouple the 3D geometry and surface chemistry by understanding the wetting and chemical properties generated by the DBD plasma treatment. The He test group was included as a process control with O_2 and ACN surfaces intended to increase wettability and incorporate carbonyl and amine groups respectively. NT samples set a baseline for the DBD groups and TCPS provided a comparison to standard culture surfaces. Targeting contact angles within the 40° to 60° range have been shown to best promote cell adhesion, independent of surface chemistry.[84] TCPS, He, and O_2 surfaces achieved this target range and ACN and NT surfaces were outside this range. As well, the differences in contact angle between the He and O_2 treated surfaces may be attributable different, subtle (10s of nm) structures on each[92,108] or differences in surface charge[330,331]. Qualitative SEM imaging of a treated and untreated surfaces did not reveal differences in the surface roughness.

Previous work suggests that carbonyl incorporation on surfaces tends to correlate positively with cell growth[77] and surface wettability influences protein conformation[332]. The moderate oxygen and low nitrogen content in TCPS is consistent with the manufacturing process: a corona discharge plasma in an oxygen rich environment.[25] O_2 and He chemical similarity likely due to the experimental DBD system depositing reactive species from the ambient atmosphere. Deposited malononitrile on ACN substrates was likely a by-product of plasma polymerization of the monomer as well as degradation of the vaporized acetonitrile in the energetic plasma discharge. Malononitrile is thought to inhibit metabolic rate of mammalian cells and form thiocyanate in tissues,[333]

causing detrimental effects on seeded cells. The developed custom DBD system promotes surface changes, controlled by changing the input gasses, and effectively modifies the PS targets with reactive ionized species.

Having established surface chemical differences between the groups, we next investigated how these surface properties impacted protein adhesion. It is well established that proteins will tend to adhere on surfaces, regardless of underlying composition through nonspecific adsorption.[69] However, protein conformational differences, types of bound proteins, and relative concentrations may differ due to surface chemistry.[334] The interaction between the surface chemistry, wettability, and proteins likely dictates preferences towards individual protein adhesion types and conformation.[335] By engineering surfaces to attract or repel proteins of interest, targeted cell expansion and niche generation may be possible. The first step to realizing differences in our treated surfaces included repeating wettability measurements on serum-coated surfaces. We found the surface wettability significantly increased on all surfaces, except the ACN surfaces. These data indicate that the adhered proteins may undergo a conformational change depending on the surface chemistry, as seen previously.[321,334] Total protein quantification, PAGE gel separation, and MS analysis support differences in total protein content and composition. As with all protein interacting surfaces, the Vroman Effect is certainly in play.[336] We sought to investigate how hMSCs will begin to interact with the surface. It has been previously observed that at an hour, approximately 10 % of seeded cells will begin to attach to TCPS,[337] beginning to spread on the surfaces[338]. As well, this time is near the peak (areal mass) of attached protein, forming a uniform layer, and cells

may sense this attached protein as a single uniform structure.[339] The protein layer is fully formed, though it may change over time, with higher molecular weight material generally replacing lower weight material.[340] Particular proteins of interest contain the peptide sequence arginine-glycine-aspartic acid (RGD), help to promote cell adhesion through integrin proteins.[341] ECM proteins, such as collagen, contain the RGD sequence and have been shown to influence proliferation and osteoblastic differentiation of hMSCs through cellular pathway activation and mechanical substrate deformation.[342–345] Determining the surface proteins informs ultimate hMSC response. Other than collagen, the remaining proteins mentioned in the table are not known to have definitively beneficial cell adhesion affects. Kininogen and apolipoprotein have been observed to inhibit cell adhesion processes.[346,347] ITIH proteins work to stabilize hyaluronic acid.[348] Glycoproteins play a role in cell-cell interactions, but not ECM interactions directly.[349,350] Serum albumin works to inhibit endothelial apoptosis.[351] The serpin superfamily inhibit enzymes, such as those in the coagulation cascade.[352] Macroglobulin and antiproteinases act in the foreign body response.[353,354] Serotransferrin, vitamin D-binding protein, hemoglobin, and fetoprotein are all linked to carrying metabolites.[355–358] Collagen stands apart from this group, as the only ECM component protein. Improved protein adhesion on the carbonyl containing surfaces could be due to their electronegativity relative to single bonded oxygen, encouraging hydrogen bond formation associating with proteins.[359] Conversely, ACN treated surfaces appear to resist protein adhesion, specifically ECM proteins, which may be linked to the extremely high surface wettability[360] or surface chemistry and likely acidic surface environment.[361]

Protein adhesion differences were compared against hMSC spread area, a measure of surface attractiveness, binding, and phenotype. Quantified cell spreading suggest the carbonyl groups on surfaces with contact angles between 50° – 55° act with proteins either in the media or during a coating to facilitate attachment, potentially through an amenable conformational preference or increased presence of ECM proteins.[332] Surfaces lacking these traits may lack the native biological residues necessary for optimal protein adhesion and cell anchorage, attachment, and spreading. All the treated surfaces should allow hMSCs to initially attach and grow, and that the carbonyls on surfaces are likely coordinating with proteins to encourage the cell attachment and spreading. For example, more ECM proteins were observed on O_2 surfaces and these had higher spreading as compared to He and NT surfaces. Both the use of a serum free media and treating the cells with an actin inhibitor (cytochalasin-D) reduced cell spread area as compared to both growth media conditions. This correlation indicates cell spreading is influenced by an actin-mediated mechanism with the underlying surface proteins, guided by the underlying surface properties. Though the cells likely do not sense the chemistry directly, the coordination of surface chemistry and protein adhesion certainly facilitates cell adhesion, patterning, and growth.[99,362] The underlying surface properties can be used to influence hMSC adhesion characteristics by modulating underlying adhered protein.

hMSCs stemness was evaluated with flow cytometry with a set of positive and negative multipotency markers. Moderately hydrophilic surfaces (TCPS, O_2) supported a high fraction of phenotypically expected cells, suggesting some interaction between the underlying surface chemistry, adhered protein, and differentiation potential. The adhered

hMSCs on these surfaces were found to align with previously set guidelines of surface marker expression.[363] In contrast, the ACN surface showed decreased positive and increased negative markers, indicating a reduction in multipotency.

The next objective was to evaluate growth and ECM protein expression of hMSCs grown on the test surfaces. Cumulative results suggest that adding oxygen to the plasma tended to improve hMSC surface interactions, where treatment with ACN tended to diminish these. The hMSCs expanded significantly more on the treated surfaces vs. the untreated ($p < 0.05$) and continued to express collagen I, fibronectin, and CD29. Collagen I and fibronectin are two representative ECM matrix proteins.[364] CD29 (Integrin β1), in part, helps to regulate hMSC ECM adhesion, migration, and focal adhesion kinase pathway activation.[365,366] The diminishing presence of ECM production suggests the cells may lack the ability to modify the surrounding environment on the NT surface.[367] This may be caused by the underlying protein layer directed by the surface treatment. The carbonyl containing surfaces tended to allow continued matrix production over the time studied.

The final goal was to evaluate the translatability of our 2D findings to a 3D model, working towards bringing PS from a 2D surface to 3D scaffold with directed functionalization. The 2D work details the importance of the O_2 treatment and was tested in 3D as a proof-of-concept. The method is capable of producing a wide range of geometries and heights with open internal architecture without thermally degrading the polymer. The high fraction of the low molecular weight of the low molecular weight component contained within the PS could be acting as a plasticizer to both reduce the

measured glass transition temperatures and aid in extrusion.[368,369]Additionally, this low molecular weight fraction is likely concentrated near the surface of fibers, based on the entropic forces creating a gradient of concentrations to minimize the free energy during solidification.[370] hMSCs were observed to spread and interact with the scaffold, utilizing both the polymer filaments and filling in the void spaces between the fibers. We suspect these cellular interactions were occurring throughout the entirety of the scaffolds. The trends indicate that the plasma treatment improved growth. O_2 treated scaffolds demonstrate a method to transform PS to a 3D culture surface which hMSCs attach and grow with future work seeking to investigate this further. Extrusion 3D-printed PS scaffolds have previously isolated and expanded lymphoma cancer cells, with the scaffold isolating the cells of interest[153] and PS punched scaffold have expanded hMSCs in a perfusion bioreactor[318]. Continued customization of PS scaffolds would define surface chemistry, geometry, and flow properties for individual cell populations. Further work seeks to understand how hMSCs sense these 3D culture platforms, and the influences on directed differentiation, leading to highly specialized PS bioreactors.

4.5 Conclusions

We propose a set of criteria to transform PS from a 2D to 3D culture surface. Incorporating carbonyls on surfaces with water contact angles between 50° – 55° tended to facilitate ECM protein and hMSC adhesion, produce greater numbers of cells, and a greater fraction of phenotypically expected cells. The data suggests that protein-cell coordination at the surface was influenced by the underlying surface properties, where the high electronegativity of the carbonyl bonds and moderate wettability likely improves hMSC response to adhered proteins. Extremely wetting surface detracted from these

findings. A surface containing approximately 6 % carbonyl groups on an O_2 treated polystyrene base with water contact angle between 50° – 55° would serve well as a growth substrate in 3D. Transitioning PS from a 2D to 3D culture surface would allow for culture systems utilizing flow, complex geometry, and densified culture, better replicating the *in vivo* environment and potential to generate clinically-relevant population sizes for transplantation and research.

Chapter 5: 3D Printed Polystyrene Supports Mesenchymal Stem Cell Osteogenic Differentiation and Proliferation

5.1 Introduction

Understanding how cells interact, modify, and react to the culture environment is essential in tissue engineering and regenerative medicine applications. The complex interplay between substrate properties, adhered proteins, and stem cells is crucial to achieving populations with expected differentiation capacity.[371] PS culture surfaces grafted with poly(allylamine) have been shown to support hMSC adhesion and chondrogenesis, a phenomenon not seen with poly(acrylic acid) grafted surfaces.[372] Carboxylic acid modified surfaces have been shown to enhance chondrogenic differentiation[72,319,373] and amines have been shown to enhance calcification and osteogenic marker expression.[374,375] Calcium phosphate substrates have been used to induce osteogenic differentiation.[376] Positively charged modified poly(acrylic acid) surfaces have been found to increase hMSC proliferation and support osteogenic differentiation.[377] These surface chemical modifications continue to be transitioned from 2D substrates to 3D (hydrogels), showing continuing trends in modulating cell differentiation.[378] Linking chemical influences to 3D culture systems serves the research community by mimicking the natural environment of adherent cell culture and provides a tool to investigate hMSC processes under flow to better replicate niche processes.

Along this rational, we sought to develop a plasma treated, 3D printed PS scaffold and bioreactor system for hMSC culture. Particularly, we sought to understand how surface

treatment influences growth and osteogenic differentiation. To accomplish this goal, we first characterized the effect of our surface treatment on PS. Next, we sought to understand growth and osteogenic differentiation with and without induction media in 2D and 3D culture conditions. Finally, we wanted to understand the performance of our scaffold within a perfusion bioreactor. Overall, this study focused on the impact of surface treatment on hMSC expansion and differentiation working towards a multicellular bioreactor system to model the bone marrow niche.

5.2 Materials and methods

5.2.1 3D scaffold fabrication

A 3D Bioplotter (EnvisionTEC GmbH, Gladbeck, Germany) was used to fabricate scaffolds as described.[379] Briefly, a sugar-glass support material (EnvisionTEC GmbH) was printed and used as a support substrate with PS (>50,000 MW atactic flakes, Polysciences, Inc., Warrington, PA) extruded to fabricate 15 mm diameter scaffolds of 5 layers with a center-to-center fiber distance of 1 mm extruded at 155 °C through a 0.4 mm ID needle tip, at 900 kPa, at 3 – 5 mm/s. Each layer in the scaffold was set at an 85.5 ° offset to the previous layer, creating a structure which did not repeat over the scaffold height. At the completion of prints, support material was solubilized with ddH_2O cleaned in 100% ethanol (EtOH) for 30 minutes and air dried.

5.2.2 Surface activation through plasma treatment

Test samples were activated using a Femto Diener Electronic vacuum plasma system (Ebhausen, Germany) (typically below 150 Pa). The entire chamber was filled with test gases Oxygen (O_2, Roberts Oxygen, Gaithersburg, MD) and Ammonia (NH_3, Matheson,

Bernards Township, NJ) added at 10 SCCM and system power set to 80 W. These settings were chosen as they were found to produce consistent plasma activation and chamber filling. The chamber was evacuated and flooded two times before activating plasmas. 6-well non-treated (NT) dishes were used for 2D experiments and 3D-printed scaffolds for 3D experiments. Samples were sterilized under UV light for at least 20 minutes prior to use in cell studies. Experiments were performed generally at least the following day. Samples generated at the same time were used for subsequent studies.

5.2.3 Surface characterization through water contact angle

Water contact angle was measured using Drop Shape Analysis (First Ten Angstroms, Inc. Portsmouth, VA) on approximately 3 μL drops of deionized water dispensed from a vertically mounted syringe. The pendant droplet was lowered to touch the surface and detach from the syringe, viewed through a high-resolution camera (Zoom 6000 Lens System, Navitar, Rochester, NY). Drops stabilized and contact angle measured. Five measurements were taken of each surface.

5.2.4 Chemical surface property assessment through x-ray photoelectron spectroscopy (XPS)

Quantitative spectroscopic measurements using a Kratos Axis Ultra delay-line detector (Kratos Analytical LtD, Manchester, United Kingdom) used in hybrid mode with a monochromatic Al Kα1, 2 X-ray source ($h\nu$ = 1486.6 eV) determined sample elemental distribution and bonding stoichiometry with survey scans (0 eV to 1100 eV, resolution of 1 eV) and high-resolution scans (pass energy of 40 eV, resolution of 0.1 eV). A Gaussian-Lorentzian distribution with a full width at half maximum constraint of

approximately 1.7 eV was used for peak fitting with 3 spectra per sample. Charging was accounted for by a low energy electron flood-gun with a filament current of 1.8A and charge bias of 2.5V. Differential charging on the surface was not suspected based on a lack of significant peak broadening. Binding chemistry was identified by deconvolving peaks into components based on the overall peak shape.

5.2.5 Structural characteristics of 3D-printed constructs though microcomputed tomography (μCT)

Samples were scanned by μCT (Skyscan 1272, Bruker, Kontich, Belgium) in order to generate 3D models of the printed constructs following established protocols.[271,380,381] Briefly, three samples were imaged using 180° rotation at 40 kV and 220 mA. A resolution of 8 μm/pixel was used with an Al 0.25 mm filter. Raw images were reconstructed, sliced, and analyzed using NRecon and CTAn software packages (Bruker, Billerica, MA). Data was then imported into LabView (National Instruments, Austin, TX) with 10 different longitudinal slices used to measure the maximum feret diameter, Waddel disk diameter, and spacing of fibers ($n \geq 13$/scaffold).

5.2.6 Cell culture

hMSCs (RoosterBio, Frederick, MD) were expanded in RoosterNourish media (RoosterBio). Cells were maintained in a humidified 37 °C incubator with 5% CO_2. To seed studies, culture flasks were washed with pH 7.4 PBS and lifted with 0.25% trypsin-EDTA (ThermoFisher, Watham, MA) and neutralized with media. Passage 2 - 5 hMSCs were used and treated as passage 1 upon receipt. Cells were passed into Dulbecco's Modified Eagle Medium with 10% fetal bovine serum, MEM non-essential amino acids

0.1 mmol/L, and penicillin (100 U/mL) – streptomycin (100 μg/mL) (growth media, ThermoFisher) at the start of cell studies. This media was used as the growth media for all studies. Osteogenic media contained 1 mmol/L sodium pyruvate (ThermoFisher), 100 nmol/L dexamethasone, 50 μg/mL ascorbic acid 2-phosphate, and 10 mmol/L β-glycerophosephate (Sigma-Aldrich, St. Louis, MO), as described.[382] Cells were seeded at 5,000 cells/cm^2 for 4 hours and then sufficient growth media added to cover samples. Cell counting accomplished using the Trypan Blue (Sigma-Aldrich) exclusion method with a hemocytometer. Media was changed at each time-point for 10-day studies, with induction media added at day 1, as appropriate, and twice per week for 3-week studies.

5.2.7 DNA quantification

Cells were dissociated from 3 samples with Trypsin and 0.25% EDTA. Samples were rinsed with PBS and added to lifted cell suspension. Cells were pelleted and resuspended in PBS with DNA isolated following the procedures for DNeasy Blood & Tissue Kit (Qiagen, Hilden, Germany). Isolated DNA was mixed with the diluted dye in technical triplicate and compared to a standard DNA ladder, following protocols for Quant-iT PicoGreen (ThermoFisher). Fluorescence measurements were read on a M5 SpectraMax plate reader (Molecular Devices, San Jose, CA) with an excitation wavelength of 490 nm and emission read at 538 nm.

5.2.8 RT-PCR

Sample RNA was isolated using Trizol (ThermoFisher) phase separation techniques. Briefly, 3 samples were washed with a single volume of Trizol solution and gently mixed to generate a pooled sample. Trizol solution was transferred to microcentrifuge tubes,

chloroform added, and vigorously mixed. The mixture was centrifuged at 12,000g for 15 minutes at 4°C with the aqueous (top) phase removed. 70% EtOH was added to account for 35% of the total solution volume and transferred to an RNeasy mini column (Qiagen, Hilden, Germany). Complete RNA isolation followed kit instructions. cDNA conversion was completed using a High Capacity cDNA Archive Kit (ThermoFisher) following manufacturer's procedures. ΔΔCT gene expression was completed in technical triplicate, comparing Taqman probes for genes of interest (RUNX2, ALP, and OPN) to GAPDH (endogenous control) with Universal Master Mix (ThermoFisher). A 7900HT RT-PCR system (Applied Biosystems, Foster City, CA) cycled reaction vessels as follows: 2 minutes at 50°C, 10 minutes at 95°C, 40 cycles of 15 seconds at 95°C, and 1 minute at 60°C. NT Day 1 growth media samples were used for normalization.

5.2.9 Alizarin Red S (ARS) staining, imaging, and solubilized stain quantification

At least two samples were washed with Hank's buffered salt solution (Sigma-Aldrich), fixed with 4% buffered formaldehyde 1% sucrose solution for 15 minutes, and rinsed 3 times with PBS. Calcification was stained with 40 mM pH 4.1 ARS (Sigma-Aldrich) as previously described.[383,384] Briefly, samples were washed 4 times with PBS and imaged (Nikon, Tokyo, Japan). A 30-minute room temperature 10 % (v/v) acetic acid incubation solubilized stain. Samples were mechanically detached and supernatant transferred to microcentrifuge tubes (3D scaffolds transferred as well), vortexed, and overlaid with mineral oil. Samples were heated at 85 °C for 10 minutes, cooled on ice, mineral oil removed, and centrifuged at 15,000 g for 15 minutes. The supernatant was transferred and neutralized with 10 % (v/v) ammonium hydroxide with absorbance at 405 nm

determined in technical triplicate on a plate reader (M5 SpectraMax, Molecular Devices). Absorbance was normalized to NT growth media samples.

5.2.10 Bioreactor fabrication and assembly

Bioreactor chambers were designed in SolidWorks (Dassault Systemes, Velizy-Villacoublay, France) with STL files exported, aligned, and support structures generated (Magics, Materialise, Leuven, Belgium), and fabricated with Eshell 300 on a Perfactory 4 DSP printer (EnvisionTEC) following manufacturer's procedures. Excess resin was removed from objects by soaking in 99% isopropyl alcohol (IPA) for approximately 5 minutes, rinsing with IPA, and blowing the objects dry with air. This process was repeated until resin was completely removed. Support structures were removed and chambers fully cured with up to 2000 flashes of broad-spectrum UV light (Otoflash, EnvisionTEC). Chambers were cleaned in 100 % EtOH for 30 minutes and sterilized under UV light in fresh 100% EtOH for 20 minutes, and rehydrated as described.[385] Chambers were stored in fresh sterile PBS at 4 °C until use and cleaned between uses.

14-gauge pump tubing was connected to cut 1/8" ID platinum-cured silicone tubing by 1/16" x 1/8" Kynar connectors and fed into 2-hole #5 stoppers (Cole-Parmer, Vernon Hills, IL). Open connections to the media reservoir and bioreactor chamber were covered in aluminum foil. 125 mL Erlenmeyer flasks were used as media reservoirs. 50A durometer silicone sheet of 0.5 mm thickness (Small Parts) was cut using an Epilog laser fusion M2 laser engraver to make gaskets. Stainless steel hardware (#10 flat washers, #10-24 0.5-inch machine screws, and #10-24 washers) were used to seal chambers. These components were autoclaved. Following overnight static cell seeding, as described, 3

scaffolds containing seeded cells were placed in each chamber, sealed closed with gaskets and hardware, and attached to Erlenmeyer flasks filled with 50 mL of growth media. A Masterflex L/S digital drive multichannel pump (Cole-Parmer) set at 3.4 mL/min was used to drive flow within a cell incubator. Flow rate was determined by simulating the bioreactor assembly in SolidWorks Flow Simulation to determine a shear stress approximately an order of magnitude lower than typically used to induce osteogenic differentiation (1.5 mPa surface shear stress).[31,386] At media changes, media was removed from the flasks and fresh 50 mL was added. At each time point, chambers were disassembled, and scaffolds processed as described.

5.2.11 Confocal imaging

10 day samples were washed with Hank's buffered salt solution (Sigma-Aldrich), fixed with 4% buffered formaldehyde 1% sucrose solution for 15 minutes, and washed 3 times with PBS. Permeabilization was performed for 5 minutes with a 300 mmol/L sucrose, 50 mmol/L sodium chloride, 6 mmol/L magnesium chloride, 20 mmol/L HEPES, and 0.5 % Triton-X-100 solution. Actin was stained with 2.5 % AlexaFluor 594 phalloidin (ThermoFisher) in PBS and counterstained with 1 μg/mL diamidino-2-phenylindole (DAPI). A SP5 X Leica Microsystems confocal microscope (Buffalo Grove, IL) captured Z-stacks. ImageJ projected images along the imaging axis and generated 3D renderings.

5.2.12 Statistical analysis

Statistical significance was determined through a one-way two-sided ANOVA at the 95% confidence interval ($p < 0.05$) using the Games-Howell comparison method in Minitab 18 (Minitab, Inc., State College, PA). Data is presented as mean ± standard deviation.

5.3 Results

5.3.1 Ammonia plasma treatment successfully aminated surfaces

We sought to define surface properties which translate from 2D to 3D in creating culture environment amenable for hMSC growth with tunable osteogenic response. We found that the plasma treatment saturation (i.e. no further chemical modification) occurred after 5 minutes for O_2 and NH_3 (Figure 5.1 A, B). This plasma treatment exposure was used for all remaining experiments. The greatest increase in total oxygen was observed on the O_2 treated surface and the greatest increase in nitrogen on the NH_3 treated surface ($p < 0.05$, Figure 5.1 C). High Resolution XPS spectra revealed that nitrogen species on the NH_3 treated surfaces were predominantly amines (Figure 5.1 D). Limited oxidation was present on the native NT surfaces, but the surface treatment increased both the total oxidation ($p < 0.05$) and complexity of oxygen species present (Figure 5.1 D) The increase in surface oxygen indicates the O_2 and NH_3 treatments increased the total quantity of carbonyl and carboxylate groups, though not statistically different based on measured bonding stoichiometry ($p > 0.05$) (Figure 5.1 D). The largest quantity of carboxylate groups was observed with the O_2 treated surfaces, though not statistically different ($p > 0.05$, Figure 5.1 D). This was also accompanied by a significant decrease in water contact angle for both surface treatments, consistent with increased surface energy through plasma surface activation ($p < 0.05$, Figure 5.1 E).

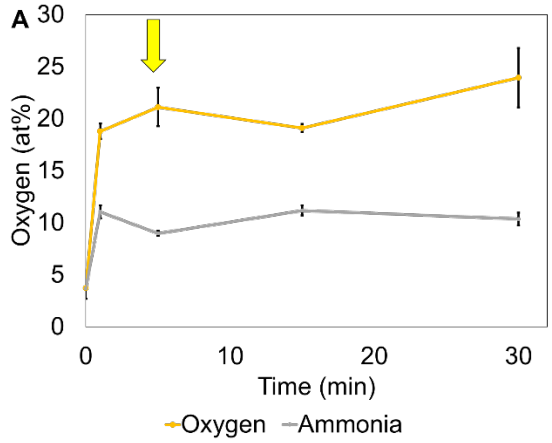

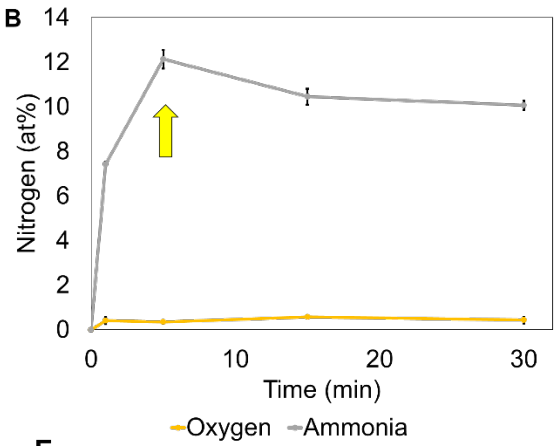

C

	C 1s (at %)	O 1s (at %)	N 1s (at %)
O2	78.5 ± 1.9	21.1 ± 1.8	0.4 ± 0.02
NH3	78.9 ± 0.2	9.0 ± 0.2	12.1 ± 0.4
NT	96.3 ± 1.0	3.7 ± 1.0	-

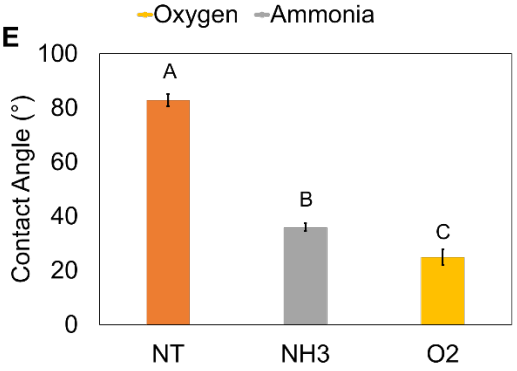

D

	285 eV C-C (at %)	286 eV C-OH (at %)	288 eV C=O (at %)	290 eV O=C-O (at %)	398 eV NH2 (at%)
O2	62.3 ± 7.6	14.6 ± 2.8	12.6 ± 2.7	5.7 ± 0.4	-
NH3	51.3 ± 23.0	20.9 ± 7.1	22.9 ± 14.1	2.6 ± 1.5	100
NT	74.0 ± 6.9	14.2 ± 2.9	6.2 ± 6.0	2.3 ± 1.7	-

Figure 5.1 Characterization of surface treatment. A) Oxygen atomic percentage (at%) vs. time for the two treated surfaces, as determined by XPS. B) Nitrogen at% vs. time for the two treated surfaces, as determined by XPS. From A, B it is observed that the oxygen and nitrogen content remain relatively constant after 5 minutes, indicating surface saturation. C) Survey XPS data detailing atomic species on the 5-minute treated surfaces. The NT surface contained little base oxidation, where plasma treatment increased both oxygen and nitrogen content. D) High-resolution XPS data, detailing the binding stoichiometry of present carbon and nitrogen species. Many oxygen species are observed on the O_2 and NH_3 surfaces, with amines incorporated into the NH_3 surface. XPS data are shown as mean ± standard deviation, 3 scans per sample. E) Static water contact angle for the treated surfaces. Significant reduction in the contact angle is observed after treatment, with the lowest contact angle observed on the O_2 surface. Groups with different letters indicate statistical difference ($p < 0.05$), data is shown as mean ± standard deviation, $n = 5$.

5.3.2 Surface amines encouraged growth and osteogenic differentiation in 2D cultures

Over the course of 10 days, it was observed that the NH_3 treated surface promoted hMSC growth as compared to the O_2 treated surface and the NT surface (Figure 5.2 A). Early osteogenic markers (RUNX2 and ALP) were generally down-regulated over the 22-day study until the final time point. At the 22-day time point, RUNX2 had the highest expression on the O_2 treated surface, followed by the NH_3, and NT surfaces ($p < 0.05$, Figure 5.2 B). The greatest and only up-regulation of ALP expression was observed on the NH_3 treated surface at the 22-day time point, followed by O_2, and NT surfaces ($p < 0.05$, Figure 5.2 C). OPN saw increasing expression only on the NT and O_2 treated surface, but no statistical differences at the final time point were found ($p < 0.05$, Figure 5.2 D). After 22 days, ARS staining was performed and semi-quantitatively assessed. It was found that there were no statistical differences between these surfaces ($p < 0.05$, Figure 5.2 E) with little characteristic bright red staining present (Figure 5.2 F).

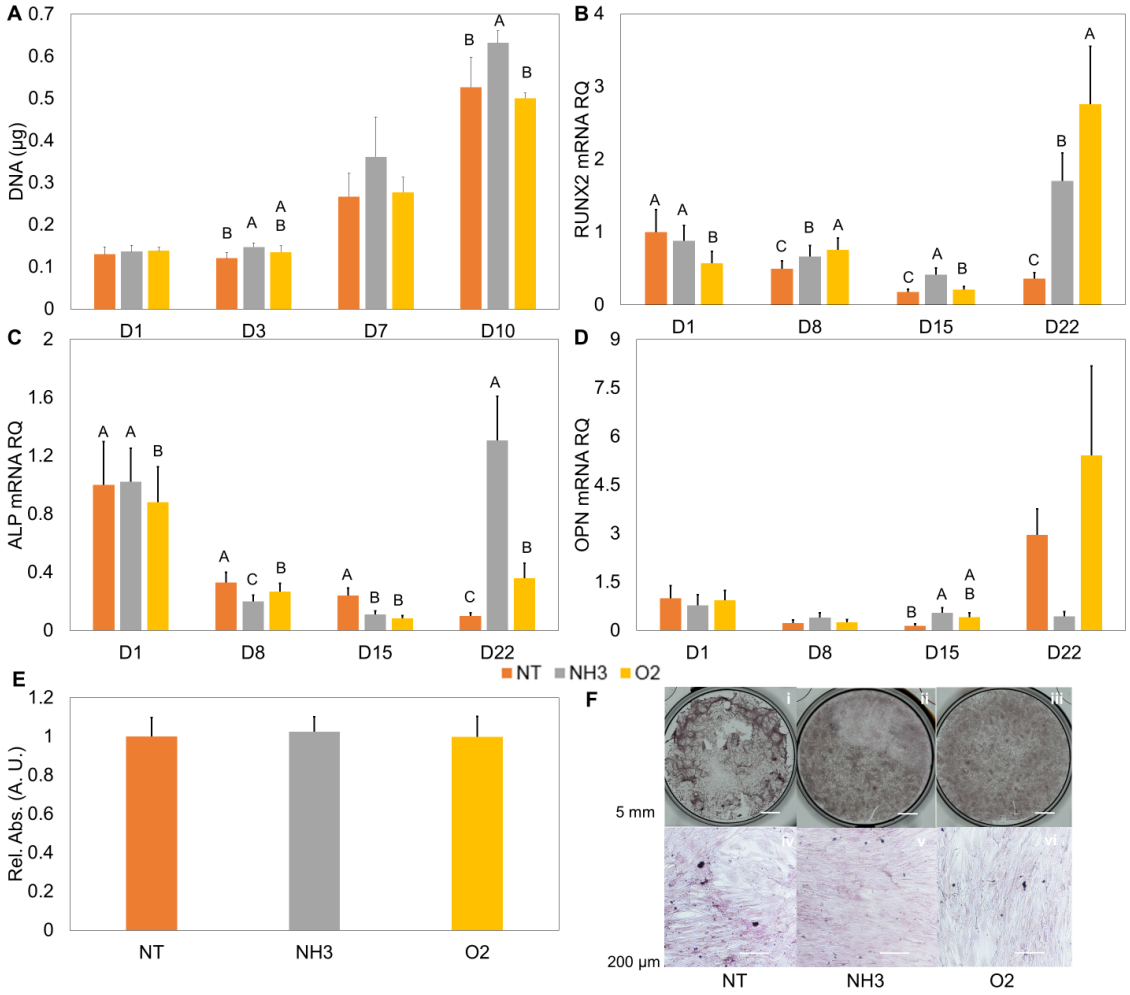

Figure 5.2 hMSC response in 2D without osteogenic media. A) Total DNA content on 2D treated surfaces. NH_3 has significantly higher DNA after 10 days of growth as compared to NT and O_2 surfaces. Data shown as mean ± standard deviation, n = 3. B) mRNA expression of RUNX2. Surfaces showed down regulation until the 22-day time-point. C) mRNA expression of ALP. Surfaces showed down regulation until the 22-day time-point. D) mRNA expression of OPN. Surfaces showed down regulation until the 22-day time-point, but was not statistically significant. E) Relative ARS absorbance as normalized to the NT surface in growth media (n = 3: NT, O_2, n = 2: NH_3). Little relative differences in calcification were observed, and confirmed F) with representative images. Note: A-D, the abbreviation 'D' as in D1 refers to day 1, A-E, groups with different letters indicate statistical difference ($p < 0.05$) at each time-point, data displayed as mean ± standard deviation. For figures B, C, and D data is in technical triplicate. F) i-iii tiled images taken at 2x and stitched with the scale bar = 5 mm. iv – vi images taken at 10x with scale bar = 200 µm.

When osteogenic media was used, characteristic differentiation traits were observed. Peaking was observed at the 8 day and 15-day time points for RUNX2 on the NH_3 surfaces and continually increasing expression on the O_2 surfaces (Figure 5.3 A). This peaking behavior at 8 to 15 days was also observed on all test surfaces with ALP (Figure 5.3 B). Higher expression of ALP was seen on the NT and O_2 surfaces, and down-regulation observed at the 22-day time point for the NH_3 surfaces ($p < 0.05$). OPN expression generally increased on the NT and NH_3 over the time course, with the greatest peak seen on the NH_3 surface after 22 days ($p < 0.05$, Figure 5.3 C). Characteristic red staining was observed with ARS, with significantly more solubilized stain present on the O_2 surfaces ($p < 0.05$, Figure 5.3 D, E).

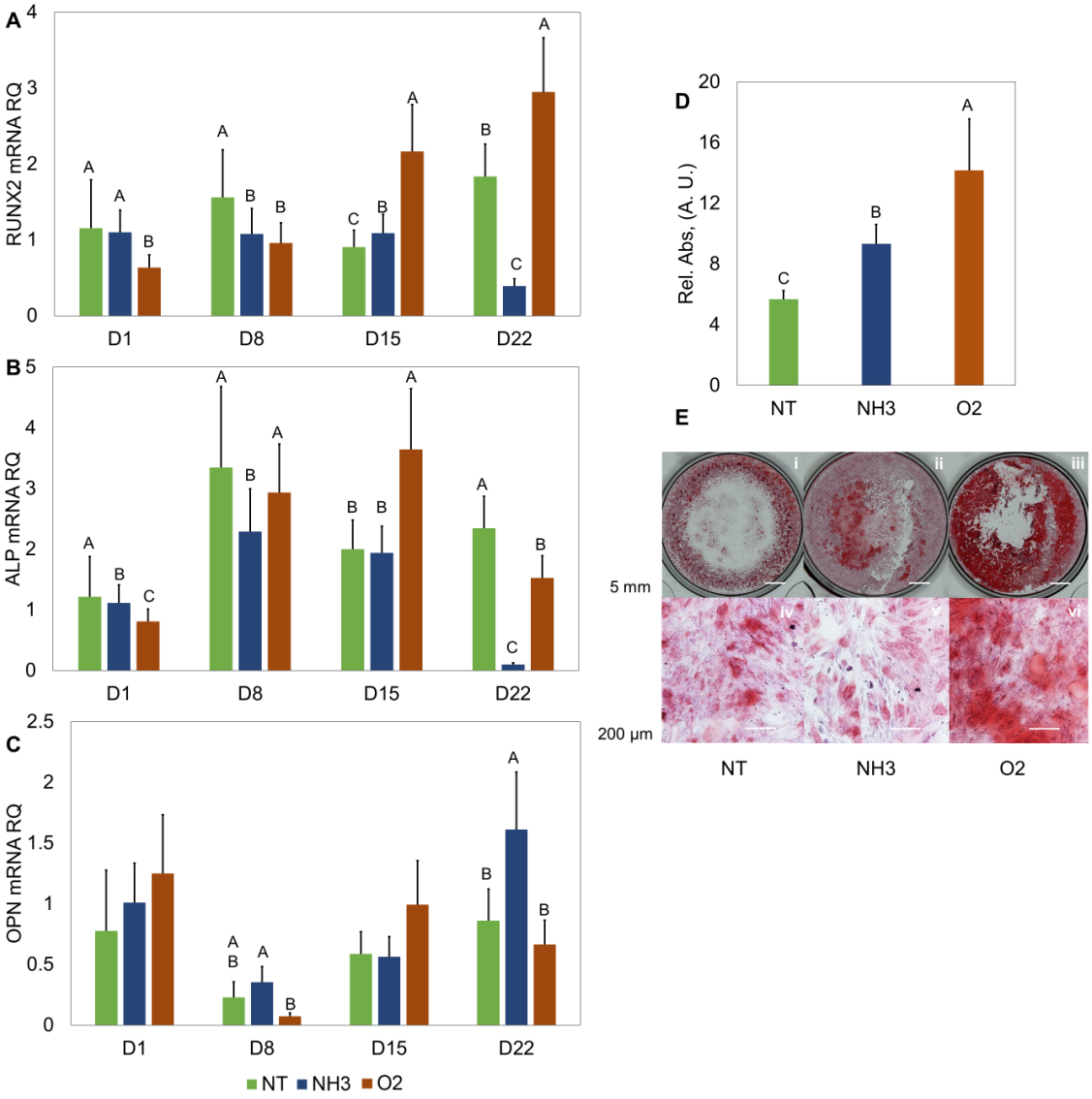

Figure 5.3 hMSC response in 2D with osteogenic media. A) mRNA expression of RUNX2. Surfaces showed up-regulation, with earlier, greater expression on NT and O_2 surfaces. B) mRNA expression of ALP. Surfaces showed up-regulation, with earlier, greater expression on NT and O_2 surfaces and characteristic peaking at the middle time-pints on all. C) mRNA expression of OPN. NH_3 surfaces showed up-regulation at the 22 day time-point. D) Relative ARS absorbance as normalized to the NT surface in growth media (n = 3). Significantly more calcification was observed on the O_2 and NH_3 surfaces as compared to the NT. The high degree of calcification was confirmed E) with representative images. Note: A-D, the abbreviation 'D' as in D1 refers to day 1, A-D, groups with different letters indicate statistical difference ($p < 0.05$) at each time-point, data displayed as mean ± standard deviation. For figures A, B, and C data is in technical triplicate. E) i-iii tiled images taken at 2x and stitched with the scale bar = 5 mm. iv – vi images taken at 10x with scale bar = 200 µm.

5.3.3 Effect of surface amination is conserved when translated from 2D to 3D culture

Having established our treatment method facilitated hMSC expansion and osteogenic differentiation in 2D, we then investigated using short (5 layer, approximate 10.5 cm^2 surface area) scaffolds. Fabricated scaffolds were found to have open internal geometry and the fabricated structures were very near the intended design (Figure 5.5). Under static conditions, we saw the O_2 and NH_3 treated scaffolds had consistent growth over the time-course (Figure 5.4 A). NH_3 treated scaffolds outperformed the O_2 treated scaffolds as measured through total DNA content, though not statistically greater, with consistently increasing growth ($p > 0.05$, Figure 5.4 A). The NT scaffolds appeared to have inconsistent, discontinuous growth (Figure 5.4 A). Characteristic hMSC spreading on and between the fibers on the treated scaffolds was observed, similar to that seen on flat TCPS (Figure 5.6 A, C, D). Spreading was seen over the complex 3D surface on the NH3 treated scaffold through 3D rendering. On the NT scaffolds, more cellular crowding was observed and overlaid cells were observed through a 3D rendering of the images (Figure 5.6 B). Similar to the 2D surfaces without osteogenic media, down-regulation of RUNX2 was observed across the time course, with the NT scaffold having greater expression than NH_3 during the 8 and 15 day time points ($p < 0.05$, Figure 5.4 B). ALP was consistently down-regulated during the time-course Figure 5.4 C). OPN expression did not see consistent increasing expression (Figure 5.4 D). Quantified solubilized ARS stain showed statistically greater calcification on the NH_3 and O_2 treated scaffolds and was confirmed visually ($p < 0.05$, Figure 5.4 E, F).

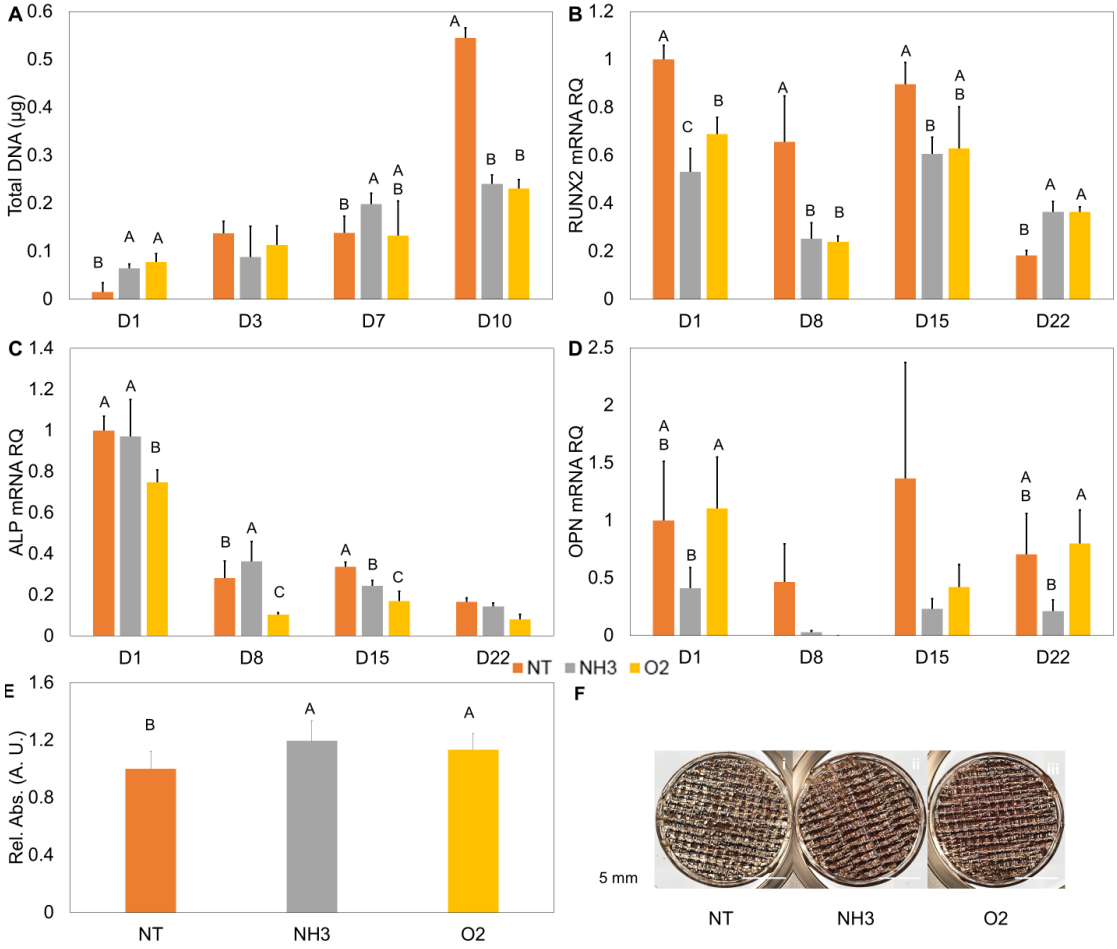

Figure 5.4 hMSC response in 3D without osteogenic media. A) Total DNA content on 3D treated scaffolds. NH_3 has significantly higher DNA after 7 days of growth as compared to NT and O_2 surfaces. Data shown as mean ± standard deviation, n = 3. B) mRNA expression of RUNX2. Scaffolds showed down-regulation during the time course, with the highest levels generally on the NT scaffolds. C) mRNA expression of ALP. Scaffolds consistently showed down-regulation, trending to decrease over time. D) mRNA expression of OPN. Scaffolds generally showed down-regulation during the study. Note: 1 NT, 2 NH_3, and 3 O_2 8 day replicates failed to amplify and were not included in analysis. E) Relative ARS absorbance as normalized to the NT surface in growth media (n = 3). Slightly higher calcification was observed on the NH_3 and O_2 surfaces, confirmed to have little overall stain with F) representative images. Note: A-D, the abbreviation 'D' as in D1 refers to day 1, A-E, groups with different letters indicate statistical difference ($p < 0.05$) at each time-point, data displayed as mean ± standard deviation. For figures B, C, and D data is in technical triplicate. F) i-iii tiled images taken at 2x and stitched with the scale bar = 5 mm.

A

Dimension (Target, μm)	Average ± Standard Deviation (μm)
Max Feret Diameter (400)	604 ± 43
Waddel Disk Diameter (400)	503 ± 21
Fiber Spacing (600)	448 ± 33

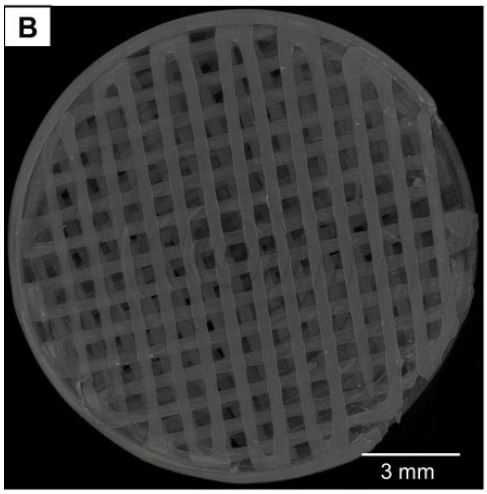

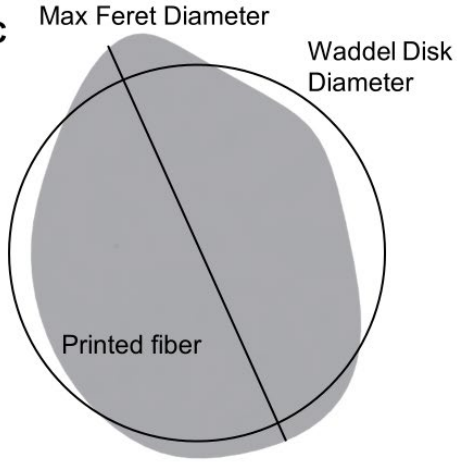

Figure 5.5 Scaffold dimensional characterization. A) Tabulated measured dimensions within 3 scaffolds. The printing parameters produced relatively consistent 5-layer scaffolds, with slightly higher overall dimensions observed for each. This indicates the fibers may be slightly pressed and oversized, giving rise to not perfectly circular fibers, but the overall consistency of the shapes indicates reproducibility of the employed method. B) Internal shape can be observed in the cut view of a reconstructed image of a 5 mm tall scaffold, with the scale bar = 3 mm. C) Diagram explaining each of the measured fiber dimensions. The fiber spacing is the measured space between fibers.

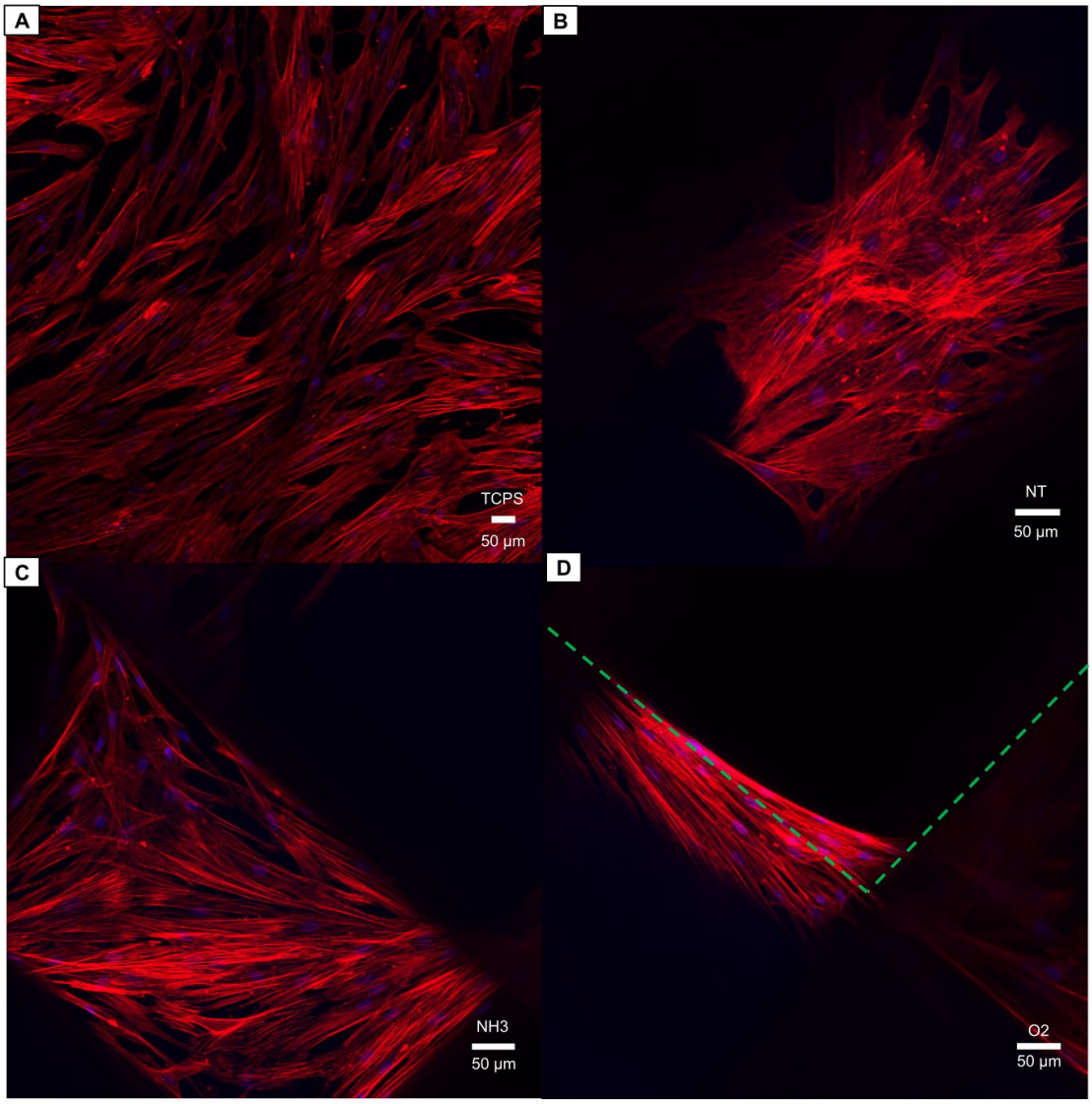

Figure 5.6 Confocal z-stack maximum projections on the treated scaffolds under static culture for 10 days. A) Tissue culture polystyrene (TCPS) is included to compare morphology. B) Highly crowded hMSCs are observed on the NT fiber surface. C) Expected spreading is occurring on and around the fibers on the NH_3 scaffolds. D) Some bridging between fibers and spreading on the fiber surface in the scaffold is observed. Cells appear to be bridging a gap between individual fibers, utilizing the 3D space. The green lines indicate the edge. Scale bar = 50 µm, F-actin is stained red, nuclei are stained blue.

When osteogenic media was used to direct differentiation, the seeded hMSCs began to undergo osteogenic differentiation. Upregulation of RUNX2 was observed, with characteristic peaking at days 8 and 15 (Figure 5.7 A). The greatest expression was seen on the NH_3 treated scaffolds, followed by the O_2 and NT scaffolds ($p < 0.05$, Figure 5.7 A). Similar trends were seen with ALP expression. NH_3 treated scaffolds had earlier, greater expression than NT or O_2 scaffolds (Figure 5.7 B). The late osteogenic marker OPN showed the greatest expression at the final time-point in the NT treated scaffolds ($p < 0.05$, Figure 5.7 C). Solubilized ARS stain showed no significant differences between the treatments at three weeks (Figure 5.7 D). Areas of red calcification were observed on the scaffolds (Figure 5.7 E).

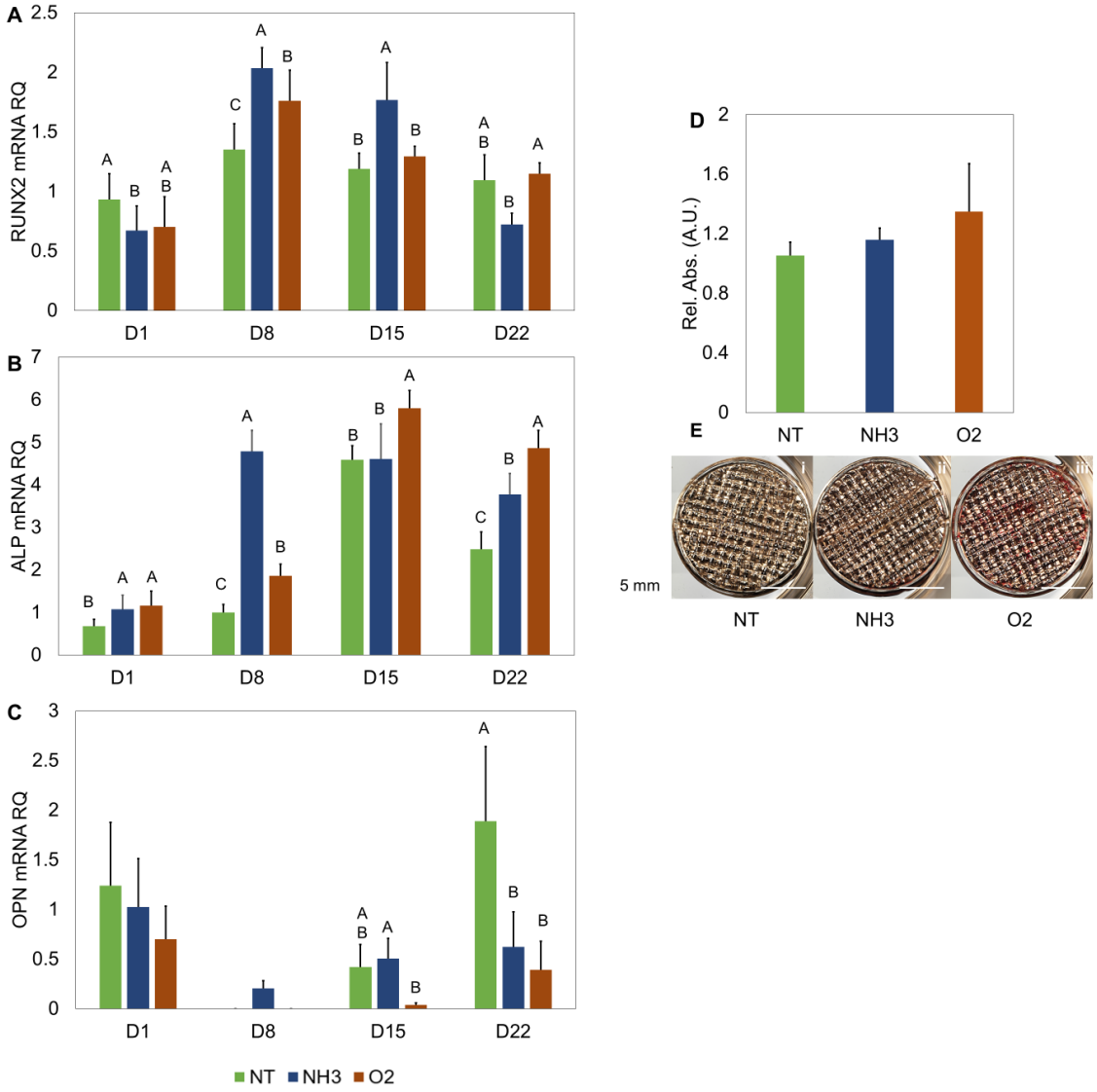

Figure 5.7 hMSC response in 3D with osteogenic media. A) mRNA expression of RUNX2. Scaffolds showed up-regulation with the addition of osteogenic media, with the highest, earliest expression seen on the NH_3 scaffolds. B) mRNA expression of ALP. Scaffolds consistently showed up-regulation with the addition of osteogenic media, with the earliest expression seen on the NH_3 scaffolds. C) mRNA expression of OPN. Scaffolds only showed significant up-regulation on the NT surface at the day 22 time point. Note: 3 NT, 2 NH_3, and 3 O_2 8 day and 1 NH_3 15-day replicate failed to amplify and were not included in analysis. D) Relative ARS absorbance as normalized to the NT scaffold in growth media (n = 3). Slightly higher calcification was observed on the NH_3 and O_2 scaffolds, but not statistically significant. Areas of higher stain can be observed on the O_2 scaffold in E) representative images. Note: A-D, the abbreviation 'D' as in D1 refers to day 1, A-D, groups with different letters indicate statistical difference ($p < 0.05$) at each time-point, data displayed as mean ± standard deviation. For figures A, B, and C data is in technical triplicate. E) i-iii tiled images taken at 2x and stitched with the scale bar = 5 mm.

5.3.4 Surface amination supported expansion without differentiation in 3D culture under flow

Moving our scaffolds into the bioreactor (Figure 5.8) resulted in consistent growth over at least seven days, with the NH_3 treated scaffolds containing the most DNA at day 3 and day 7 time points ($p < 0.05$, Figure 5.9 A). NT and O_2 treated scaffolds did not appear to support continued growth while under dynamic culture. Unintended differentiation did not appear to occur on the treated surfaces as well. RUNX2 expression decreased over time, as in 2D and 3D, with the NT scaffold showing the greatest relative expression ($p < 0.05$, Figure 5.9 B). ALP expression remained down-regulated across all time-points and treatments (Figure 5.9 C). Interestingly, even without any chemical signaling to undergo differentiation, the NT treated surfaces experienced significantly greater, continually increasing OPN up-regulation when exposed to flow (Figure 5.9 D). OPN expression was seen on the NH_3 and O_2 scaffolds as well, with an expression peaking at day 8 and no statistical difference between the two groups ($p < 0.05$, Figure 5.9 D). NH_3 scaffolds were seen to have relatively higher ARS stain after 22 days ($p < 0.05$, Figure 5.9 E), but little total calcification observed with all groups (Figure 5.9 F).

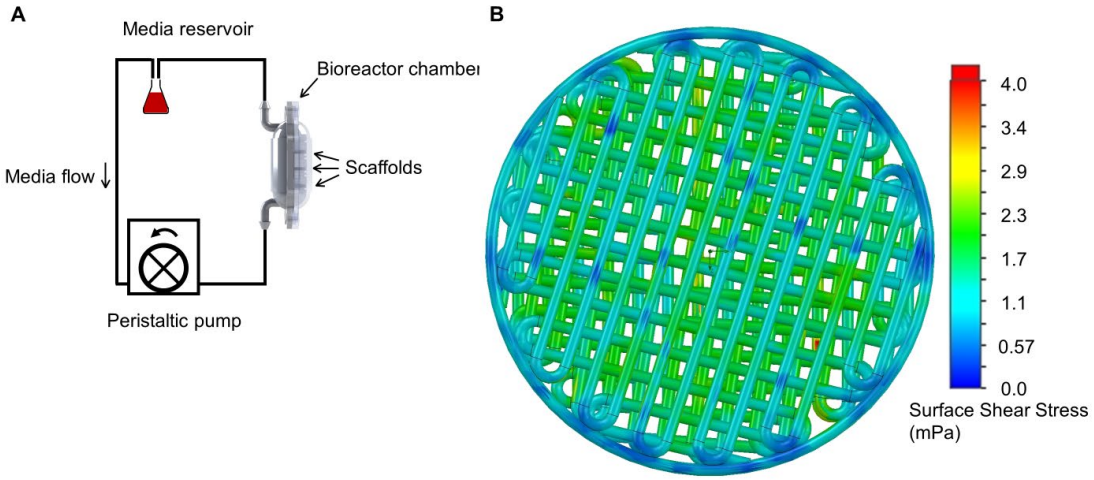

Figure 5.8 Bioreactor design and shear stress determination. A) A diagram of the bioreactor assembly. Fluid is pumped antiparallel to gravity to remove air and provides consistent flow through the assembly. The entire pump and fluid line is placed inside a cell culture incubator. B) Verification of the design with drawn scaffolds shows the average shear stress across the 3 scaffolds to be 1.5 ± 0.06 mPa at 3.4 mL/min. The top view of the central scaffold is shown with a heat map of the surface shear stress showing uniform shear distribution throughout the object.

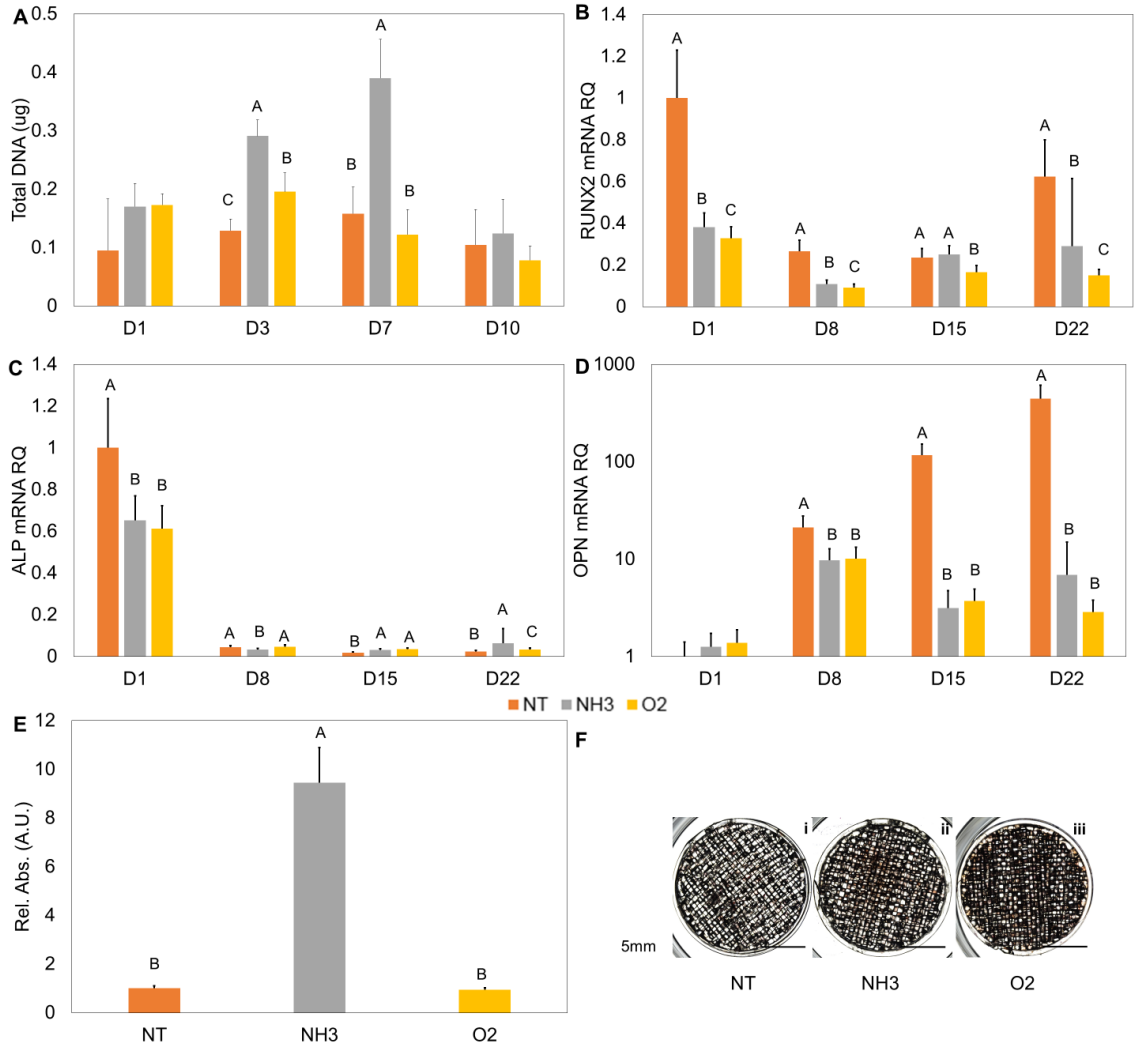

Figure 5.9 hMSC response in 3D dynamic culture. A) Total DNA content on 3D dynamic treated scaffolds. NH_3 has significantly higher DNA after 3 and 7 days of dynamic growth as compared to NT and O_2 surfaces. Data shown as mean ± standard deviation, n = 3, O_2 Day 1 two scaffolds cells were combined and subsequently split prior to DNA extraction and analysis. B) mRNA expression of RUNX2. Scaffolds showed down-regulation during the time course, with the highest levels generally on the NT scaffolds. C) mRNA expression of ALP. Scaffolds consistently showed down-regulation. D) mRNA expression of OPN. The NT scaffolds showed significant up-regulation during the study, with NH_3 and O_2 showing modest upregulation as well. E) Relative ARS absorbance as normalized to the NT scaffold in growth media (n = 3). Higher calcification was observed on the NH_3 scaffolds, confirmed to have little overall stain with F) representative images. Note: A-D, the abbreviation 'D' as in D1 refers to day 1, A-E, groups with different letters indicate statistical difference ($p < 0.05$) at each time-point, data displayed as mean ± standard deviation. For figures B, C, and D data is in technical triplicate. F) i-iii tiled images taken at 2x and stitched with the scale bar = 5 mm.

5.4 Discussion

Establishing how hMSCs respond to osteogenic stresses helps to define surface properties and underlying culture influences to develop our bone marrow niche model. A short (5 minute) exposure to the energetic vacuum plasma was sufficient to modify the 2D and 3D test substrates. The drastic reduction in surface carbon content ($p < 0.05$) is consistent with an extensively modified surface and a greater proportion of functional groups detected, which work in tandem with proteins to facilitate cell adhesion and spreading.[322,387] The incorporation of different surface groups and properties affect protein adhesion through electrostatic and polar interactions seeking to minimize surface free energy.[89,388,389] The minor quantity of surface oxygen in the NT surface appeared as a few different species, but their relative total presence (i.e. greater oxidation, $p < 0.05$) was much greater with the plasma treatments. The incorporation of oxygen and nitrogen outside of the intended treatment (e.g. oxygen in the NH_3 treatment) likely comes from reacting with the ambient air. The treatment did produce a surface with nitrogen primarily bound as amines, resulting in two distinct surface types for investigation. As well, we observed the O_2 treated surfaces had higher surface energy (lower water contact angle, $p < 0.05$). Previous work has shown that surface contact angles between 40 ° – 60 ° best facilitate cell adhesion.[84] The NH_3 treated surfaces were closest to this range. It is possible that unwanted protein spreading / denaturation could occur based on the water contact angle,[321] ultimately influencing hMSCs adhesion to the protein layer. Interestingly, we observe a correlation between surface carboxylate content and water contact angle. These differences in the surface properties were observed to influence hMSC response. We suspect this is the underlying reason for the differences in cell

growth and proliferation. By controlling the surface properties, we sought to direct hMSCs growth and differentiation.

Our selected scaffold geometry sought to gain inspiration from trabecular bone geometry while creating a scaffold which could be reliably printed. Trabecular bone has a highly porous (9 % – 26 % bone volume/tissue volume) structure with trabecular thickness between 120 μm – 219 μm and trabecular spacing between 667 μm– 712 μm.[390] The design with 400 μm fibers and 600 μm spacing and without a repeating layer structure over the scaffold height allows for fluid flow to penetrate throughout the scaffold without narrowing the flow to individual channels as would be seen in a highly structured pattern. To verify functionality of the printed construct, we first investigated hMSC growth on our printed structures. Consistent across the static culture conditions (2D, 3D), aminated surfaces best supported hMSC growth without unintended osteogenic differentiation. Similar results have been previously observed.[76] This leads towards the development of targeted hMSC PS scaffolds for hMSC growth. The improved hMSC response on the NH_3 treated surfaces and scaffolds is attributable to a combination of positive surface charge, moderate surface energy, and decreased surface carbon content all leading to appropriate protein conformation at the surface.[391–396] These same properties were not found with the NT and O_2 treatments. Inconsistencies in NT hMSC growth on the 3D surface may be a result of poor distribution through the scaffolds, as the poorly wetting surface prevented media from fully coating the internal structure during seeding, resulting in cell crowding at the surface. We observed that the seeding media was rapidly drawn into plasma activated scaffolds where the NT scaffolds saw the seeding media sit on top

and more slowly be drawn in during seeding. This also suggests the bulk of the objects were activated and allowed hMSCs to interact, adhere, and grow throughout. The O_2 treated scaffolds supported modest growth and spreading along and between fibers, with similar surface treatment, oxygen content, and oxygen species, and as commercial TCPS.[97,397] Doubling times for of bone marrow derived hMSCs have been observed to be as high as 2.5 days and higher for hMSCs from other sources.[398] In this study, the hMSCs doubled approximately every 3 to 4 days. To ensure our treatments produced culture platforms for hMSCs to expand and not undergoing unintended osteogenic differentiation, we surveyed a two early and two late osteogenic markers. Studies were taken out to 3 weeks as these are typical time lengths when these osteogenic markers should be expressed. Without osteoinduction media, osteogenic markers surveyed remained primarily down-regulated, consistently so on the NH_3 treated 3D-printed scaffolds. In 2D, the hMSC population began to express osteogenic markers at day 22 where this was lacking in 3D. The gained biomimicry from the 3D platform is suspected to help maintain the population here.[204] The compliment of 3D geometry and underlying chemistry directing the underlying protein layer, on our PS surfaces and scaffolds was sufficient to expand hMSCs without osteogenic differentiation.

When aiming to develop bone marrow niche models, it remains prudent to understand how the underlying surface chemistry may work to influence an adhered hMSC population. Likewise, we intended to understand how our scaffolds influence osteogenic differentiation. Geometry of scaffolds can influence hMSC fate,[231,399] with the research goals remaining to reduce spontaneous osteogenic differentiation. Based on our work,

this was not observed, but did observe increased relative expression of osteogenic markers in 3D as compared to 2D, indicating the geometry could be aiding in osteogenic progression without causing it. When osteogenic media was included in culture, earlier peaking of early osteogenic markers on NH_3 surfaces was observed and is consistent with previous results.[373,374] We found that the addition of induction media initiated osteogenic differentiation on all surfaces, with expression enhanced by surface amines and consistent across 2D and 3D. Surface amination resulted in earlier and greater expression of RUNX2 and ALP. RUNX2 has been theorized as a master regulator, and marker for osteogenic differentiation.[400,401] ALP expression during osteogenic differentiation typically peaks, and then expression should decrease as later osteogenic markers begin to express and mineralized matrix is deposited.[402] These early markers typically peak after 1 to 2 weeks of culture.[22,403] The shifted differentiation timeline, particularly in 3D, of NT and O_2 indicates that hMSCs adhered to this surface treatment may react more slowly to the chemical osteoinduction signaling present in the media. This theory is supported with the NH_3 2D surface expressing significantly more OPN than either of the other surfaces. Significant calcification is visually observed in 2D and moderate calcification observed in 3D. Calcification and OPN expression will typically increase with osteogenic differentiation.[33] Improved seeding efficiency in 3D would likely improve total calcification. Interestingly, increasing OPN expression is observed on the NT 3D scaffold, indicating the lack of surface chemistry scaffolds may be supporting the later stages of osteoblastic differentiation. Cumulatively these data show the NH_3 treated surfaces and scaffolds supported directed osteogenic differentiation. Osteogenic commitment was not observed solely based on surface chemistry. This indicates a

potential interaction exists between the soluble chemistry in the induction media and underlying surface chemistry interact to help direct differentiation.

Following directed differentiation, we investigated our scaffold construct under dynamic culture. The bioreactor design was expected to encourage growth without differentiation, as the estimated shear stress is an order of magnitude below typical values used to induce osteogenesis.[31,386] With the flow rate of 3.4 mL/min, we aimed to develop a bioreactor where flow would aid nutrient and oxygen exchange without spontaneous osteogenic differentiation and lead to long-term growth of contained hMSCs. By establishing this model, we aim to developing PS scaffolds for consistent and predictable expansion in the bioreactor which leads to the use of a widely accepted and studied culture substrate as the basis for investigating the mechanosensitive nature of hMSCs.[225,404] Building this model lends the future possibility of coculture and using the adherent hMSC population to direct a non-adherent population, as is the current approach in hematopoietic stem cell (HSC) expansion.[405] Developing the bioreactor culture for hMSCs initially allows us to build to a bioreactor bone marrow niche mimic for coculturing HSCs and hMSCs for future clinical applications. However, the NT scaffold and the O_2 scaffold did not support consistent hMSC expansion in the bioreactor. We suspect the dynamic culture environment have worked to shear adhered proteins or cells, where the NH_3 treatment aided in keeping adhered proteins and cells on the scaffolds. Using this hierarchical building structure, changing surface properties to vary protein adhesion, and direct hMSC behavior, appears to be a viable strategy when transitioning PS from a 2D to dynamic 3D culture substrate. The bioreactor system developed with the NH_3 treated scaffolds was

capable of expanding hMSCs without unintended osteogenic differentiation, as demonstrated by the consistent down-regulation of early osteogenic markers. This trend was observed across treatments. The higher relative calcification measured is likely due to the low number of cells present on the NT surface, as is confirmed visually, reducing the total amount of stain available to solubilize. Interestingly, OPN expression increased exponentially on the NT scaffolds inside the bioreactor, as observed in induced 3D culture. Some OPN expression was present on the NH_3 and O_2 treated scaffolds. This link between surface properties and flow indicates that the lack of surface functionality within the dynamic environment impacts this late stage differentiation marker. In addition to being known as a later-stage osteoblastic marker, OPN is thought to regulate population size in the HSC niche by inhibiting cell proliferation.[406] Balancing total population present and expression of this marker has future use in regulating and developing the bioreactor towards a bone marrow niche model. On-going work is looking to investigate how to use this functionality to work in the bioreactor environment and encourage this type of intercellular signaling to build a bone marrow niche model for long term HSC renewal, with hMSCs on scaffolds as a feeder source during dynamic culture. Ultimately, optimization and continued development of this bioreactor system seeks to build on these complex cell-cell interactions, increasing biomimicry with up to 4 separate cell populations per line possible or increased cell output with increased chamber or scaffold size.

5.5 Conclusions

The goal of this study was to define surface properties which encouraged hMSC expansion without inducing osteogenesis. We found that aminated PS works to support

hMSC growth in 2D, 3D, and 3D dynamic conditions superiorly to NT and O_2 treated surfaces and scaffolds. The underlying surface chemistry was insufficient on its own to induce differentiation but did support directed osteogenic differentiation. The NH_3 scaffolds enhanced early osteogenic differentiation, in agreement with previous literature. Placing scaffolds in the bioreactor favored the establishment of a quiescent HSC-like niche environment. PS scaffolds with an NH_3 treatment best supports hMSC growth and intended osteogenic differentiation. This method results in consistent hMSC expansion on 3D-printed PS scaffolds in both static and dynamic culture for up to 7 days. The demonstrated method presents a self-contained bioreactor model for hMSC growth without unintended osteogenesis. This creates a platform for dynamic culture modeling and studying the multicellular interactions found in the bone marrow niche *in vitro*.

Chapter 6: Modulating Jurkat Proliferation with Mesenchymal Stem Cells in Bioreactor Culture

6.1 Introduction

Methods for expanding HSCs and their progenitors have applications in treating multiple disease states. Maintenance of HSCs during MSC coculture is theorized to occur through intercellular crosstalk, such as cytokine expression,[407] though some expressed cytokines (e.g. TGFβ) may harm HSCs (e.g. inhibit proliferation).[408] MSC expansion in a bioreactor is becoming an accepted method for producing MSCs to HSCs, with previous work suggesting the approach can achieve clinically relevant HSC populations from manageable bone marrow aspirates.[409]

To study these complex cell interactions, a model cell line can be employed. Jurkat cells are a T-lymphocyte cell line originally isolated with the intent of studying leukemia.[410] T-lymphocytes are a terminally differentiated cell type from HSCs within mononuclear cells (MNCs).[411] The interaction between MSCs and leukemia cells (e.g. acute myeloid leukemia) is suggested to occur within the bone marrow niche.[412] It has been reported that MSCs support T-lymphocyte survival in a quiescent state, preserving inactivated T-lymphocytes by preventing cell division and rescuing Jurkats from chemically induced apoptosis.[413] MSCs expressing the Fas ligand (Fas-L) had highly inhibitory effects on multiple myeloma cells, with a binding between Fas and Fas-L inducing apoptosis significantly.[414] However, MSCs which lacked the Fas-L promoted multiple myeloma growth.[414] This suggests heterogeneity in an MSC population could play a role in the

ultimate therapeutic effects. Others have suggested the inhibition of T-lymphocyte proliferation by MSCs could be temporary and reversible, by interacting during the early stages of cell division to prevent expansion.[415] MSCs have also been reported to enrich Jurkat proliferation in static and dynamic coculture.[26] Further investigation into the interactions between these cell populations would better inform bioreactor design and coculture systems for MNCs and bone marrow niche models.

In this study we sought to develop a dynamic culture environment for Jurkats and investigate the effect of hMSC coculture. To demonstrate the utility of our culture system, we investigated the effects of flow rate, culture substrate, geometry, and coculture ratios to modulate Jurkat proliferation. The presence of signaling molecules and interaction with culture surfaces was evaluated to support observed interactions between the cultured cells. Future work seeks to decouple the surface and coculture effects and continue development of the bioreactor system to include additional cell types.

6.2 Materials and Methods

6.2.1 3D scaffold and chamber fabrication

A 3D Bioplotter (EnvisionTEC GmbH, Gladbeck, Germany) was used to fabricate 5 layer PS scaffolds with 0.4 mm diameter fibers spaced 1 mm a part, with each layer offset from the previous one by 85.5° creating a regular non-repeating structure. PS (>50,000 MW atactic flakes, Polysciences, Inc., Warrington, PA) scaffolds were printed on top of a sugar-glass support material (EnvisionTEC GmbH), as previously described.[379] Support material was removed with ddH_2O, scaffolds cleaned in 100% ethanol, and air dried.

A multilevel bioreactor scaffold (MBS) was designed in SolidWorks (Dassault Systemes, Velizy-Villacoublay, France) and fabricated out of Eshell 300 on a Perfactory4 DSP (EnvisionTEC) following the manufacturer's procedures, as described.[385] Briefly, a 30 mm long 12.7 mm diameter tube-like structure with 5 layers of 0.5 mm pillars with 1 mm spacing was fabricated to which allows flow through the circuit and around the pillars. Bioreactor chambers were fabricated similarly, with chambers designed to accommodate the printed PS constructs. Excess resin from objects was removed by soaking in 99% isopropyl alcohol (IPA) for 5 minutes, rinsing the surface with IPA, and blowing the objects dry with air. This was repeated until excess resin was removed. Support structures were removed, and objects cured with up to 2000 flashes of broad-spectrum UV light (Otoflash, EnvisionTEC) and cleaned in 100% ethanol (EtOH) for at least 30 minutes. Objects were sterilized under UV light in fresh 100% EtOH for at least 20 minutes and rehydrated in a series of pH 7.4 phosphate buffered saline (PBS):EtOH washes (ratios of 75:25, 50:50, 25:75 and 0:100), with a 5 minutes soak at each step. Objects were stored in sterile PBS at 4 °C until use and cleaned between uses.

6.2.2 Surface and scaffold activation with ammonia plasma

PS samples and non-tissue culture treated PS 6-well culture dishes were activated using a Femto Diener Electronic vacuum plasma system (Ebhausen, Germany). The entire chamber was evacuated and filled 2 times with ammonia added at 10 SCCM and plasma ignited with the system power set to 80 W to create amine activated PS (PS-A). Samples were generally used in cell studies the day following surface activation.

6.2.3 Cell culture

Human MSCs (hMSCs, RoosterBio, Frederick, MD) were thawed and expanded in RoosterNourish media (RoosterBio). Passage 3 to 5 hMSCs were used for studies and cells were treated as passage 1 upon receipt. At the start of studies, hMSCs were rinsed with pH 7.4 PBS (Sigma-Aldrich, St. Louis, MO), lifted with 0.25% trypsin-EDTA (ThermoFisher), and neutralized with media. hMSCs were passed into Dulbecco's Modified Eagle Medium with 10% fetal bovine serum, MEM non-essential amino acids 0.1 mM, and penicillin (100 U/mL) – streptomycin (100 μg/mL) (hMSC media) (ThermoFisher) at the start of cell studies. hMSCs were seeded for 4 hours and then sufficient growth media added to allow complete adhesion overnight. Jurkat (E6-1, ATCC, Manassas, VA) were thawed and expanded in RPMI 1640 (ATCC) with 10% FBS (Jurkat media). Jurkats were seeded at 1 x 10^5 cell/mL for all studies and cultures were maintained at most every 3 days. Cell counting was accomplished using the Trypan Blue (Sigma-Aldrich) exclusion method with a hemocytometer. Cell culture was accomplished in a cell culture incubator with humidified atmosphere at 37 °C and 5% CO_2. Coculture experiments used a 50:50 ratio of hMSC and Jurkat medias.

6.2.4 Static Jurkat, hMSC, and coculture practices

PS and PS-A samples were sterilized under UV light for 20 minutes prior to use in cell studies. hMSCs were then seeded at 5,000 cells/cm^2 onto culture substrates for 4 hours. Additional media was then added to fully cover the surfaces/scaffolds and allowed to adhere overnight. The next day, the hMSC media was replaced with coculture media and Jurkats seeded, as appropriate. Three pre-seed volumes were taken to determine DNA fold change. Three cell cultures were performed of each condition. Cultures were run for

3 days, at which time samples were collected, surfaces rinsed with PBS and collected, and hMSCs dissociated from surfaces.

6.2.5 Dynamic Jurkat, hMSC, and coculture practices and bioreactor assembly

Overnight static hMSC seeding was performed at variable densities. Three scaffolds with or without seeded hMSCs were placed in each chamber and sealed closed with custom cut 50A durometer silicone gaskets (Small Parts) and stainless-steel hardware, as described in chapter 5. Autoclaved 0.125 inch platinum cured silicone tubing connected to 14-gauge pump tubing was attached to bioreactor chambers and the 2-hole #5 stopper attached to the Erlenmeyer flasks filled with 50 mL of coculture media with seeded Jurkats. A Masterflex L/S digital drive multichannel pump was set at 3.4 mL/min and was used to drive flow within a cell incubator. At the end of each 3 day study, media containing Jurkats was collected and lines run clean with PBS and collected. For static studies, scaffolds and surfaces were rinsed with PBS to collect any adhered Jurkats. hMSCs were dissociated from surfaces using 0.25% trypsin EDTA and collected, as applicable. Collected cells then had DNA quantified relative to initial study seeding quantities. For Jurkats this was 3 aliquots of the cell seeding volume and hMSCs this was hMSCs isolated at the start of seeding. Jurkat bioreactor lines used 3 cell aliquots from each line ($n \geq 2$).

6.2.6 DNA quantification

Double stranded DNA content was quantified using Quant-iT PicoGreen (ThermoFisher) following the Manufacture's protocol. Briefly, cells were resuspended in PBS and sample DNA isolated following the procedures for DNeasy Blood & Tissue Kit (Qiagen, Hilden,

Germany). Isolated DNA was diluted as necessary and mixed with the diluted dye in technical triplicate and compared to a standard DNA ladder. Fluorescence measurements were read on a plate reader (M5 SpectraMax Molecular Devices, San Jose, CA or Spark Multimode Microplate Reader, Tecan, Mannedorf, Switzerland) with an excitation wavelength of 490 nm and emission read at 538 nm.

6.2.7 Total protein determination

Media samples were diluted 1:10 in PBS and tested on 3 samples in technical triplicate with a Pierce BCA Protein Assay following standard microplate procedures. A 50:50 DMEM:RPMI 1640 control was run for correction as well. Samples were quantified against a standard curve in technical triplicate and read on a Spark Multimode Microplate Reader at 562 nm.

6.2.8 Polyacrylamide gel electrophoresis (PAGE) protein separation and Coomassie staining

A Mini-Protean TGX (Bio-Rad, Hercules, CA) gel was loaded with Laemmli buffer and 1:5 diluted media samples (in PBS), as described.[299] The gel was run for approximately an hour at 120 V in 1X Tris-Glycine buffer and washed in ddH_2O with protein bands visualized and imaged with Coomassie blue on a LICore Odyssey CLx (Lincoln, NE).

6.2.9 Multiplex analysis

A Luminex MagPix system (ThermoFisher) with Luminex software (Riverside, CA) was used to quantify IL-10, osteopontin (OPN), Fas-L, Fas, and hepatocyte growth factor (HGF) from media aliquots against a standard curve in technical duplicate following manufacture's (R&D Systems, Minneapolis, MN) procedures.

6.2.10 Cell staining and imaging

Jurkats were counted and resuspended in serum free Jurkat media containing 2.5 μmol/L CellTracker Green (ThermoFisher) and incubated for 45 minutes in growth conditions. Media was replaced with coculture media and PS and PS-A samples were cultured for 3 days and images captured (Nikon, Tokyo, Japan). Images were adjusted to remove background fluorescence in ImageJ.

6.2.11 Flow bioreactor assembly

0.5 inch, 0.25 inch, and 0.125 inch platinum cured silicone tubing was cut and connected to 14-gauge pump tubing with Kynar connectors to create an increasing in size line assembly with the open ends inserted into a 2-hole #5 stopper (Cole-Parmer) and a side left open for the MBS to be inserted. Open connections were covered in aluminum foil and the entire line was autoclaved. For lines using a scaffold, the scaffold was inserted into the open line and bioreactor sealed. The completed line was attached to a Masterflex L/S digital drive multichannel pump (Cole-Parmer) with 50 mL of Jurkat media in and 125 mL Erlenmeyer flask and seeded with Jurkats. Studies ($n \geq 2$) were run with static controls ($n \geq 2$) of equal volume and seeding density in T75s culture flasks. After 3 days of culture in a culture incubator, media containing cells was collected and lines run clean with PBS to collect additional cells within the lines. These were collected, and an aliquot of the cells had their DNA quantified relative to study controls.

6.2.12 Statistical analysis

Unless noted, statistical significance was determined with the following: through one-way two-sided ANOVA at the 95% confidence interval ($p < 0.05$) using the Games-

Howell comparison method for studies with more than 2 groups or two-sample Student's t-tests were performed for studies with 2 groups with Minitab 18 (Minitab, Inc. State College, PA).

6.3 Results

6.3.1 PS-A culture substrate had inhibitory effects on Jurkats

In this chapter, we built on our adherent culture results in chapter 5 to understanding how defined surface chemistry influences a non-adherent cell population and can modulate proliferation through cytokine expression. We found that Jurkats in coculture media above PS surfaces and scaffolds tended to proliferate more than Jurkats cultured above PS-A surfaces and scaffolds, as indicated by the listed t-test values for each culture condition (Figure 6.1 A). This trend was not observed under dynamic culture (Figure 6.1 A). Cocultured Jurkats saw the inhibitory effect of the PS-A surface as well regardless of culture condition ($p < 0.05$, Figure 6.1 B). The PS-A scaffolds and surfaces were generally found to have greater amounts of hMSCs in 2D and 3D dynamic mono and coculture ($p < 0.05$, Figure 6.1 C, D). In 3D static culture, this effect was muted or reversed (Figure 6.1 C, D).

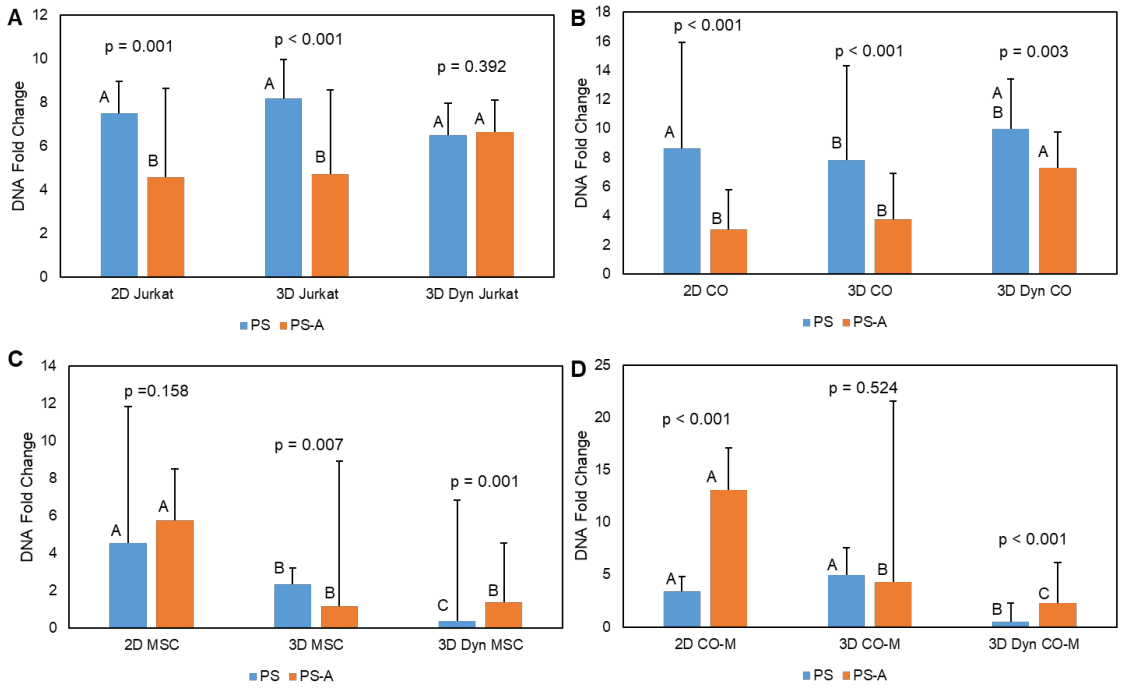

Figure 6.1 Jurkat response in monoculture and coculture. A) DNA fold change from pre-seed Jurkats after 3 days of culture. PS surfaces and scaffolds tended to have greater Jurkat fold change as compared to PS-A surfaces and scaffolds in monoculture. Running the Jurkats in the bioreactor removed the effect in monoculture. For static 2D and 3D cultures n = 3, dynamic culture n = 2 with 3 aliquots per line. B) DNA fold change from pre-seed Jurkats after 3 days of coculture. 'CO' refers to Jurkats cultured under a coculture condition. PS surfaces and scaffolds tended to have greater Jurkat fold change as compared to PS-A surfaces and scaffolds across all culture conditions. For static 2D and 3D cultures n = 3, dynamic culture n = 2 with 3 aliquots per line. C) DNA fold change from hMSCs lifted at the start of the 3-day study in monoculture. D) DNA fold change from hMSCs lifted at the start of the 3-day study in coculture. 'CO-M' refers to hMSCs cultured in a coculture condition. In both instances, the adherent fraction tended to prefer the PS-A surface, particularly in dynamic culture. For static 2D and 3D cultures n = 3, dynamic culture 2 lines were used for coculture and a 1 line for monoculture, 3 scaffolds per line, hMSCs seeded at 5000 cells/cm^2. Note: Groups with different letters indicate statistical difference ($p < 0.05$) within a test group (PS-A, PS), data displayed as mean ± standard deviation. p-values for two sample t-tests are listed above applicable group pairs.

6.3.2 PS-A surfaces had greatest differences in protein content

The culture media from the 2D culture condition was tested to determine the total protein content. In the 1:10 diluted samples, it was found that Jurkats cultured above the PS-A surface had less protein than the corresponding coculure condition. ($p < 0.05$, Figure 6.2 A). No other significant differences were found. Analyzing the media content through a Coomassie stained PAGE gel showed similar banding as compared to the 50:50 hMSC:Jurkat media and FBS controls (Figure 6.2 B).

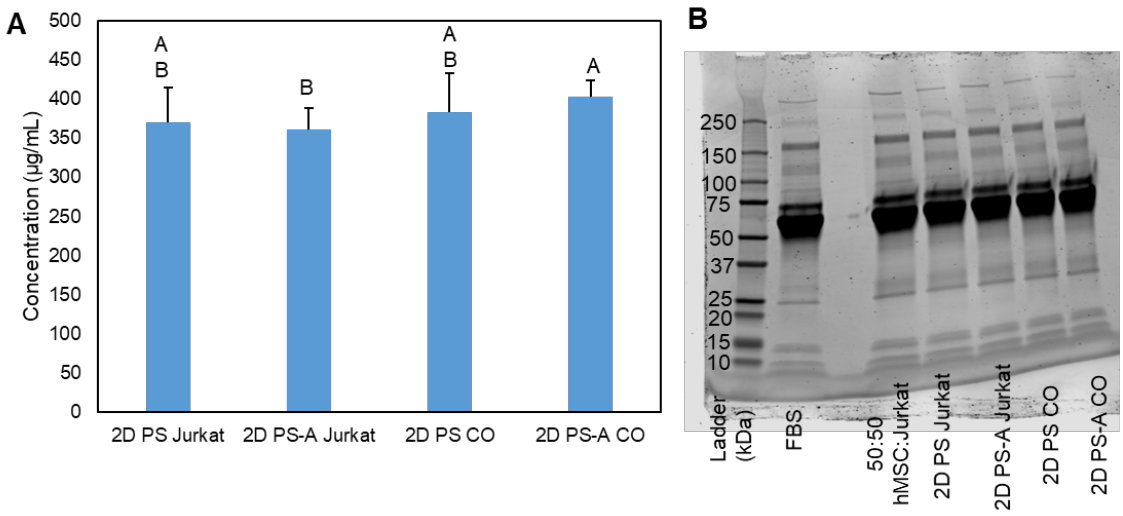

Figure 6.2 Protein content in mono and coculture media. A) BCA protein content of the 2D culture media conditions (n = 3). Statistical difference was observed between the two PS-A groups. B) Coomassie stained gel showing bands of the tested media groups. Note: groups with different letters indicate statistical difference ($p < 0.05$), data displayed as mean ± standard deviation.

6.3.3 Inhibitory cytokines in media linked to hMSCs coculture

Individual metabolites were analyzed to determine the total soluble amount in the media at the end of 3-day culture. These cytokines are theorized to act through both indirect and direct cell-contact methods (Figure 6.3 A). IL-10 (< 1 pg/mL) and Fas-L (< 2 pg/mL) were both measured below the minimum value of their respective standard curves in the assay (data not shown). OPN (Figure 6.3 B) was below the detection limit of the assay for the 50:50 hMSC:Jurkat media and the 2 monoculture (PS, PS-A) 2D conditioned medias (< 23 pg/mL). Total soluble OPN content was statistically greater ($p < 0.01$) in the PS-A coculture conditioned media than the PS coculture conditioned media (Fig. 3B). Fas (Figure 6.3 C) and HGF (Figure 6.3 D) appeared to show similar trends. Fas (Figure 6.3 C) was below the detection limit in the 50:50 hMSC:Jurkat media, with greater expression observed in the monoculture conditions as compared to the and coculture conditions ($p < 0.01$). HGF was below the detection limit in the 50:50 hMSC:Jurkat media, the PS-A, and PS monoculture conditions (Figure 6.3 D). Total HGF showed no statistical difference ($p > 0.05$) between the PS-A and PS coculture conditions (Figure 6.3 D).

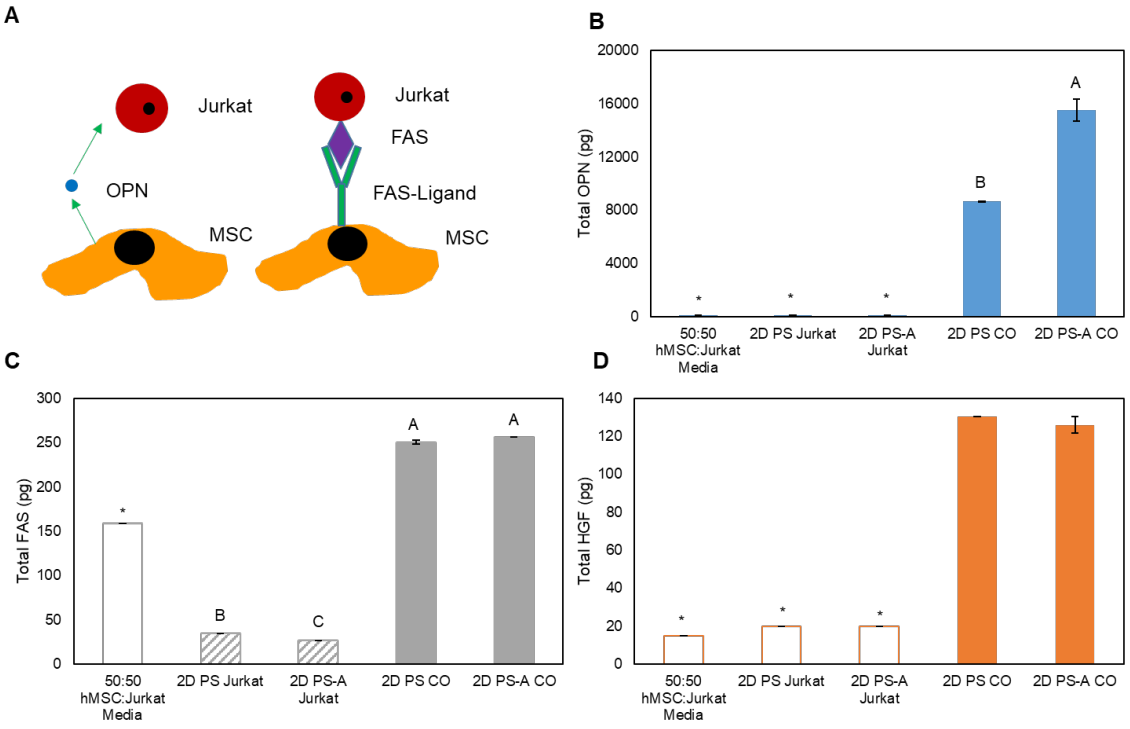

Figure 6.3 Quantification of inhibitory cytokines in media. A) A diagram of two interaction pathways for soluble analytes in the culture media, acting either through non-contact or direct cellular contact means. B) Total OPN content in media samples. 50:50 hMSC:Jurkat, PS monoculture, and PS-A monoculture samples were below the detection limit of the assay. C) Total FAS content in media samples. 50:50 hMSC media was below the detection limit of the assay. PS and PS-A monoculture samples are extrapolated and statistically different at $p < 0.05$. PS monoculture, PS-A monoculture, and PS-A coculture measures read as identical values. D) Total HGF content in media samples. 50:50 hMSC:Jurkat, PS monoculture, and PS-A monoculture samples were below the detection limit of the assay. PS 2D coculture measures read as identical values. B-D note: Groups with different letters indicate statistical differences ($p < 0.05$, data displayed as mean ± standard deviation, data shown in technical duplicate. Groups with different letters indicate statistical difference ($p < 0.05$) determined with a Tukey's multiple comparison test. Solid bars are within assay limits, extrapolated values are marked with hatched bars and noted where necessary. Samples below the detection limit of the assay which could not be extrapolated are set at the maximum possible value, marked with an open bar, and excluded from statistical analysis (marked with an '*').

6.3.4 Jurkats adhered to PS-A surfaces, clustering with themselves on PS

Imaging of the Jurkats (green) illustrates a few qualitative differences between the cultures and culture conditions. The PS-A surfaces appeared to have relatively uniform distribution of Jurkats (Figure 6.4 A), where they formed larger aggregates on PS surfaces (Figure 6.4 B).

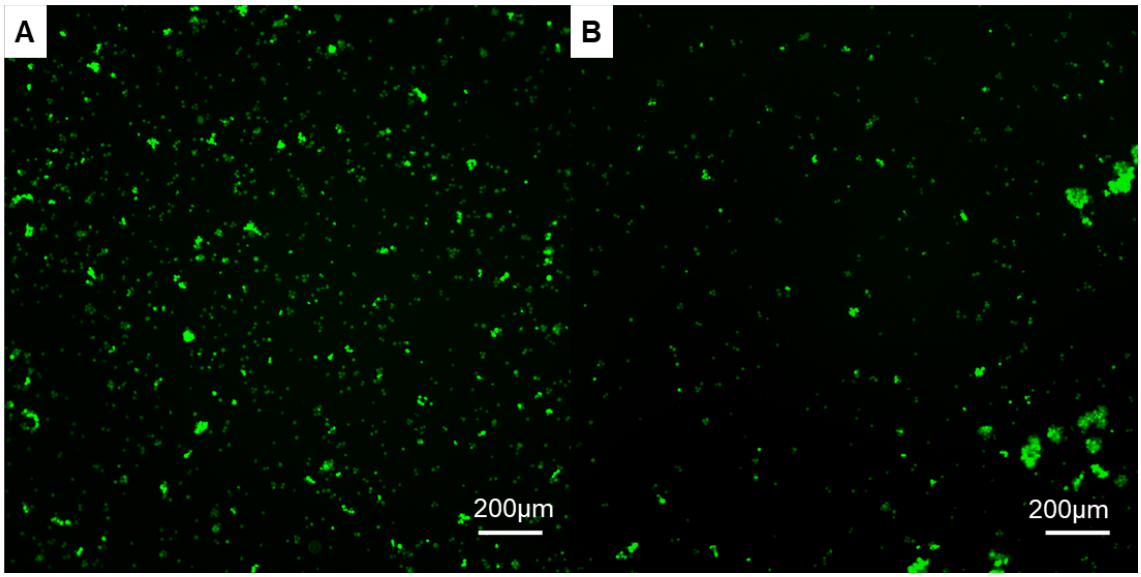

Figure 6.4 Fluorescent images of stained Jurkats. Jurkats appear to spread across PS-A surfaces with greater clustering observed on PS surfaces preferentially. A) PS-A surfaces in monoculture. B) PS surfaces in monoculture. Note: Scale bars are 200 µm, Jurkats are stained green

6.3.5 Jurkats are insensitive to pure dynamic culture

We found that several flow rates, spanning two orders of magnitude (0.21 mL/min, 2 mL/min, 10 mL/min, and 20 mL), with and without a MBS scaffold (Figure 6.5 A, B) did not affect Jurkat proliferation. Relative DNA content of dynamically cultured Jurkats without a scaffold showed no statistical differences between the groups ($p > 0.05$, Figure 6.5 C). Similarly, Jurkats cultured with the MBS were unaffected by dynamic culture (Figure 6.5 D). The introduction of the scaffold did not affect proliferation between the MBS containing and lacking studies as well (p-values 0.21 mL/min: 0.403, 2 mL/min: 0.797, 10 mL/min: 0.484, 20 mL/min: 0.08). Jurkats continued to proliferate under the dynamic culture condition independent of flow rate or scaffold presence.

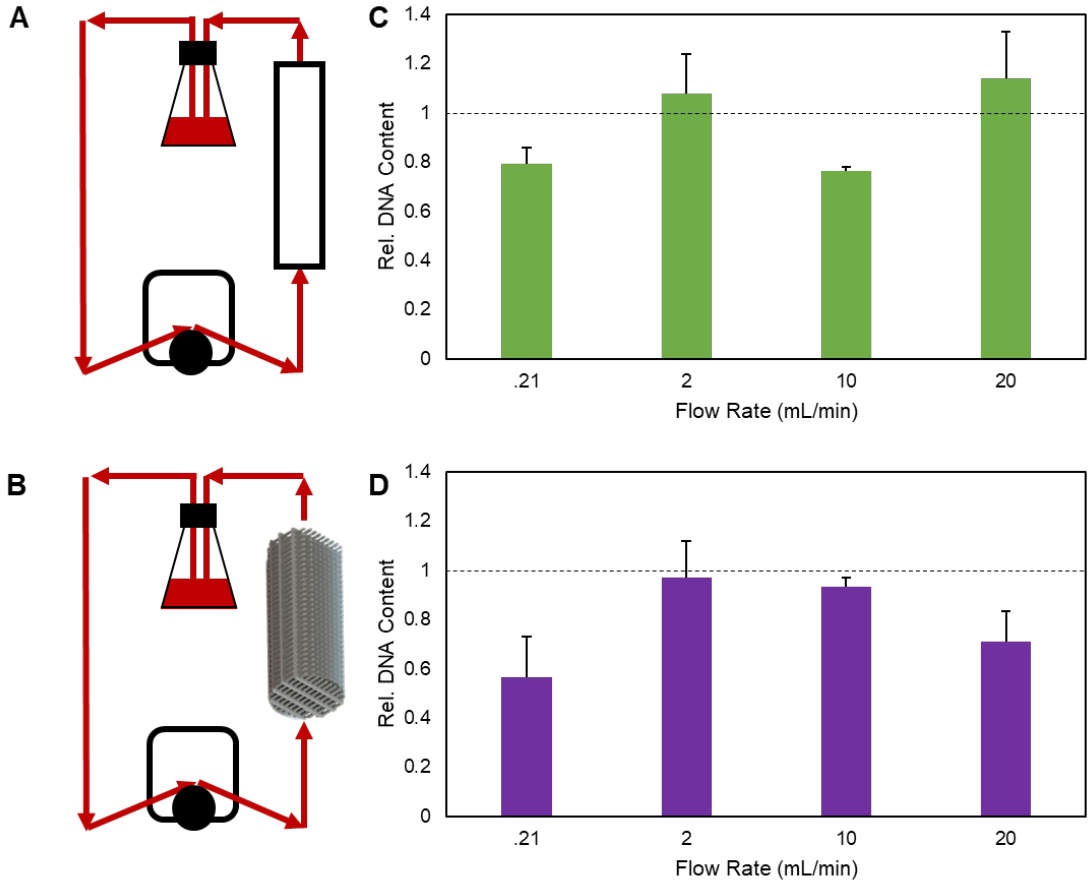

Figure 6.5 Bioreactor culture of Jurkats at a range of culture velocities. A) A diagram showing the empty bioreactor line and B) a bioreactor line with the MBS construct. The same diameters and approximate lengths of tubing and connections were used between lines. C) Relative DNA content of the tested bioreactor lines compared to applicable study controls. No significant differences were found between the groups. This indicates perfusion alone did not impact Jurkat proliferation. Note: 0.21 mL/min (1 RPM) and 20 mL/min n = 4, 10 mL/min n = 3, 2 mL/min n = 2. D). Relative DNA content of the tested bioreactor lines containing a scaffold compared to applicable study controls. Note: 0.21 mL/min (1 RPM) and 20 mL/min n = 3, 10 mL/min n = 4, 2 mL/min n = 2. T-tests between individual flow rates showed no significant differences ($p > 0.05$), indicating the introduction of the scaffold did not negatively impact the proliferation along. All data is shown as mean ± standard deviation.

6.3.6 Increasing hMSCs in bioreactor had moderate inhibitive effects on Jurkat proliferation

Using the bioreactor model to culture cells at specific culture ratios, we found some inhibitive effects when the culture ratio of hMSCs:Jurkats was varied from 1:1 to 1:50 (Figure 6.6 A) in our bioreactor culture (Figure 6.6 B). The 1:1 culture ratio was statistically lower than the 1:15 culture ratio, but not from other culture conditions ($p < 0.05$). The 1:50 culture ratio was statistically lower than then 1:15 and 1:10 culture conditions ($p < 0.05$).

Individual metabolites were analyzed for the 4 highest hMSC ratios (1:1, 1:5, 1:10, 1:15). IL-10 (< 1 pg/mL) and Fas-ligand (< 2 pg/mL) were both below the minimum value of their respective standard curves (data not shown). OPN content (Figure 6.6 C) was somewhat anti-correlated to hMSC quantity, with higher hMSC cultures generally showing lower total soluble OPN. This trend was not seen in the 1:15 culture condition. FAS (Figure 6.6 D) and HGF (Figure 6.6 E) showed similar trends, with the statistically greatest total soluble metabolite content seen in the 1:1 culture ratio media sample ($p < 0.01$).

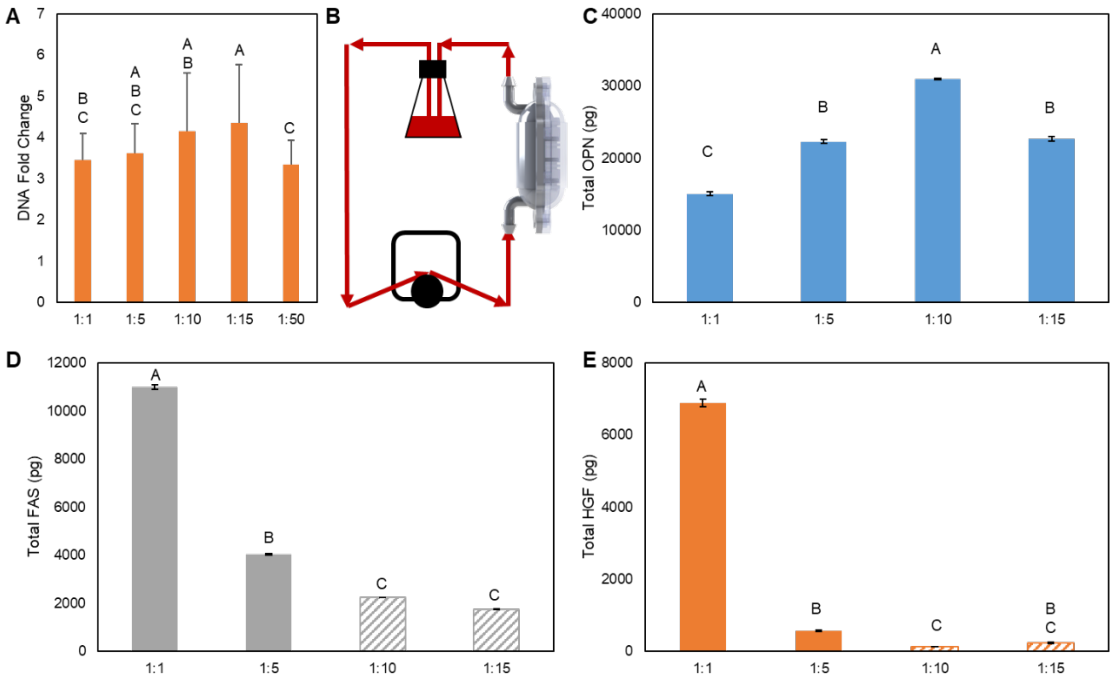

Figure 6.6 Bioreactor coculture and cytokine expression. A) DNA fold change to pre-seed Jurkats after 3 days of culture. hMSCs were seeded overnight on PS-A scaffolds to produce cell ratios of 1:1 (n = 2), 1:5 (n = 3), 1:10 (n = 3), 1:15 (n = 3), and 1:50 (n = 2) per line hMSCs:Jurkat. Each line chamber contained 3 scaffolds of hMSCs. Moderate proliferation inhibition was observed between the 1:1 and 1:15 culture ratios. B) Diagram of the bioreactor design. Media perfused the circuit into the chamber containing scaffolds. C) Total OPN content in media samples. D) Total FAS content in media samples. 1:10 and 1:15 media samples were below the detection limit of the assay, extrapolated and statistically different at $p < 0.05$. 1:10 measures read as identical values. E) Total HGF content in media samples. 1:10 and 1:15 media samples were below the detection limit of the assay and extrapolated. 1:5 and 1:15 samples found to be statistically different at $p < 0.05$. 1:10 measures read as identical values. Notes: A) Groups with different letters indicate statistical difference ($p < 0.05$), data displayed as mean ± standard deviation. C – E) Solid bars are within assay limits, extrapolated values are marked with hatched bars and noted where necessary, data shown in technical duplicate. Groups with different letters indicate statistical difference ($p < 0.01$) determined with a Tukey's multiple comparison test. Data displayed as mean ± standard deviation.

6.4 Discussion

By understanding how our culture platform performs with multiple cell types in coculture, we work towards deconstructing the bone marrow niche environment and develop a meaningful culture tool. First, we sought to determine the effect of culture substrate and coculture with hMSCs on Jurkats. A media formulation of 50:50 hMSC:Jurkat media was used, though further investigation may find a media formulation more beneficial to the culture, as media formulation impacts the expansion of similar (e.g. MNCs) cells.[416] Three day studies were used to assess differences during the typical expansion window for Jurkat cells to reach the maximum suggested confluence in culture. Jurkat proliferation was investigated on PS and PS-A surfaces. Under 2D and 3D static conditions, the culture ratio (based on initial seeding densities) was 1:6 hMSCs:Jurkats, and at 3D dynamic is was 1:32. Here we tried to isolate the effect of the underlying culture surface. Previous work has found that HSC are sensitive to culture surfaces, even as a non-adherent cell population.[417] This is potentially through differential protein adhesion and loss of biological activity by absorptive losses to the culture surface or through toxin leaching.[417] Polystyrene is well established as a non-cytotoxic culture material, through different surface treatments could cause differential adhesion of proteins.[379] As well, culturing with MSCs also works to bolster underlying surface effects with intercellular communication between the populations. Generally, it was observed that the Jurkat population proliferated more on the PS surfaces rather than the PS-A surfaces, independent of culture condition. This effect was not seen in dynamic monoculture suggesting flow forced the circulating cell population or solubilized protein to not adhere, influencing cell proliferation.

We observed that the hMSC-Jurkat interaction played a role in modulating Jurkat proliferation. Several molecules have been suggested to participate in this interaction. Fas and Fas-L cause activated T-lymphocyte apoptosis in murine models.[418] OPN has been observed to negatively regulate growth in the HSC niche, working to control population size.[406] IL-10 produced by hMSCs have been observed to inhibit T-lymphocyte activation through antigen presenting cells.[419] HGF from hMSCs has also been observed to suppress T-lymphocyte proliferation.[420] These molecules, or their subunits, range from 18-69 kDa.[421–425] Concentration differences between the culture conditions and the presence of protein bands within this range could mean that these proteins are present with different quantities available to act on the cells. With the lowest concentration on the PS-A surface, and greatest on the PS-A coculture surface, this suggests proteins may be interacting with the PS-A surface to deplete the protein in the media, while the MSCs could be working to boost the protein content. This helps to explain the inhibition seen with both the PS-A surfaces in both culture conditions. Analyzing the individual metabolites, we failed to detect any of the inhibitory cytokines in the base media formulation. The coculture media samples showed significantly ($p < 0.01$) greater quantities of OPN, Fas, and HGF, indicating the hMSCs are the source of these inhibitory molecules. This aligns with previous observations of the inhibitory effects of MSCs on T-lymphocytes.[426–430] With the variety of cytokines associated with MSCs,[431,432] other molecules could be acting as well.

However, this does not fully explain the observations made in Jurkat monoculture. We suspect that there are a few competing pathways at work. The Jurkat population appears to more readily adhere on the PS-A surface. These observations could mean that contact with the surface plays a role in limiting proliferation. The PS-A surface was seen to deplete protein from the media and could be working to adhere a greater fraction of cells as well. A contact inhibition mechanism could be acting to prevent Jurkat expansion where association with the PS-A surface slows proliferation. Further investigation into these contact and cell-mediated modulatory mechanisms could help provide a clearer understanding of the bone marrow niche, the associate immune functions, and development of targeted therapies for hematological malignancies.

By understanding the impact of the culture substrate and hMSC population in static and a single dynamic culture condition, we next investigated the effect of flow on the circulating Jurkat population. Both with and without a MBS present in the perfusion bioreactor assembly, no significant difference in relative DNA content was observed between the flow rates. This is significant as the circulating cell population needs to navigate the roller assembly of the perfusion pump and the tubing circuit, which could become more difficult at higher flow rates. It is possible that, at sufficiently high flow rates, cell damage from impacting the tubing during flow could lead to cell lysis or metabolic inhibition.[433,434] Previous studies have used Jurkat bioreactors to enhance proliferation, and proposed the mechanism was the breaking of cell aggregates that form.[435] Though we did not find significant changes in proliferation as compared to static cultures, the culture method is sufficient in supporting expansion of Jurkats across 2

orders of magnitude in flow rate and at two flow of conditions: with and without a scaffold.

Having established the Jurkat population is insensitive to flow rate with our perfusion driven culture, we looked to modulate Jurkat proliferation using the hMSC population at a single flow rate. Following similar hMSC:Jurkat culture ratios as performed in previous studies,[415,436] A general trend was observed where increasing the hMSC population size decreased Jurkat proliferation. This was not consistent across all culture rations, with the highest amount of hMSCs (1:1) only statistically different from the 1:15 ratio. At 3 days of culture, a previous group found a lack of proliferation inhibition from adipose derived hMSCs in culture ratios of 1:5 and 1:10.[436] While we used bone marrow derived hMSCs, the cell source or population characteristics could play a role in Jurkat modulation. Quantifying the Fas and HGF in the media found that in the highest (1:1) culture ratio had statistically greatest amount of these cytokines and generally decreasing quantities of with decreasing hMSC fraction. The correlation between these markers and population size explains the observed growth inhibition. The soluble OPN content appeared to be anti-correlated, suggesting this factor plays a less significant role.

6.5 Conclusions

In this chapter, we build on the successes with our culture model for expanding hMSCs by modulating Jurkat proliferation. These are necessary steps towards working with HSCs and developing the envisioned closed-loop bone marrow niche bioreactor. Here we demonstrate the utility of the closed loop culture system by knocking down proliferation in a cancer population. Jurkat cells remained insensitive to bioreactor flow rate, but

experienced inhibited growth when cultured above PS-A. The differences in protein content in the media suggests different signaling occurring between the mono and cocultures, while imaging suggests greater adhesion to the PS-A surface. Substrate contact inhibition could be acting to reduce proliferation. The increased measured content of FAS and HGF, and correlation with inhibited proliferation, suggests these soluble factors are expressed by hMSCs and work to inhibit proliferation. The utility of our model goes beyond recapitulating a cancerous niche environment. HSCs remain a difficult population to expand *in vitro*. With the evidence presented, our model stands as a rapid manufacturing solution to expanding primary human bone marrow and completing development of widely accepted bone marrow niche model.

Chapter 7: Conclusions and Future Directions

7.1 Summary

In this dissertation, we demonstrate a 3D printing and plasma functionalization strategy to develop complex substrates for *in vitro* cell growth. The work establishes a culture environment which facilitates protein adhesion and directs cell function in 2D, 3D, and dynamic culture environments. By taking care to engineer culture substrates with defined properties, we present a successful method for enhancing hMSC proliferation, directing osteogenic differentiation, and suppressing Jurkat expansion. Continued development of the model would see a method for expanding therapeutic cell populations for specific clinical targets, investigating mechanistic interactions within the bone marrow niche and a method to screen pharmaceuticals rapidly. Continued maturation of this technology would see a closed loop culture method for HSCs, working towards eliminating hematological malignancies.

The first objective of this work was to understand the surface properties which help to facilitate cell adhesion through surface properties and protein interactions. In chapter 4, we found that moderate water contact angles (50° - 55°) and complex oxygen species (carbonyl content of 6%) work to promote extracellular matrix protein adhesion (e.g. collagen consisted of 3.6% of the adhered protein from serum). With these adhered surface proteins, hMSCs are able to spread and interact with the surface, with greater spreading generally observed on the moderately hydrophilic surfaces. We suspect this spreading is acting through an actin related mechanism, as evidenced with an F-actin

inhibitor, and the surface properties work to maintain higher ratios of phenotypically expected hMSCs. With higher growth rates ($p < 0.05$) and continued expression of extracellular proteins, these surfaces were capable of supporting hMSCs modifying the surrounding culture environment. PS following the developed 3D printing process method lacked material degradation, ensuring maintenance of expected material properties. Additionally, the flexibility afforded with 3D printing allows for a wide range of internal scaffold architectures and overall geometries. Future investigation could interrogate the structure-cell function relationship. Lastly, we showed hMSCs were able to interact with 3D constructs, adhering, spreading, and expanding (with a p-value of 0.011 as compared to a NT scaffold) on and between the fibers. This shows that the hMSC population accepted the 3D oxygen-treated PS.

Having validated our printing and surface activation approach, the next objective of this work was to use surface properties to enhance hMSC proliferation and direct differentiation. In chapter 5, we started this by improving our treatment approach and found incorporating surface amines encouraged greater expansion of hMSCs in 2D, 3D, and 3D dynamic culture. After 7 days of dynamic culture, a total of 0.39 μg of DNA were found on the aminated scaffolds as compared to 0.15 μg and 0.12 μg of DNA for the non-treated and oxidized PS surfaces, respectively ($p < 0.05$). We also found that the aminated PS enhanced directed osteogenic differentiation by encouraging greater and earlier expression of osteogenic markers. For example, hMSCs cultured on aminated 3D scaffolds showed mRNA ΔΔCT of values for ALP of 4.78 as compared to 1.00 and 1.86 for the non-treated and oxidized PS 3D scaffolds at 8 days, respectively ($p < 0.05$).

Cumulatively, the presented data demonstrate a mechanism for enhancing hMSC proliferation and differentiation while retaining characteristics between 2D and 3D, further validating the culture system.

Having established our culture method predictably expands hMSCs understand static and dynamic conditions, in chapter 6 we explored the culture environment's impact on a non-adherent population. We found that a model T-lymphocyte cell line, Jurkats, were able to grow at a wide range (0.21 mL/min – 20 mL/min) of flow rates in monoculture without significant differences between the flow rates. Some inhibition of the culture was observed to be caused by the underlying surface properties. For example, under static 2D conditions, Jurkats were observed to increase 7.5x with the PS surface and 4.5x on the aminated PS surface ($p = 0.001$). We explored the impact the hMSC population had on the Jurkat cells and found that increasing the hMSC fraction had a moderate inhibitory effect on the Jurkats, with a 1:1 culture ratio allowing a 3.5x fold change of Jurkats but increasing the Jurkat fraction to 1:15 allowed 4.4x fold change ($p < 0.05$). We also explored differences in the culture media and found the PS-A culture conditions had significantly different ($p < 0.05$) amounts of protein between mono and coculture. The coculture condition was observed to have greater total amounts of HGF and Fas as compared to the monoculture condition ($p < 0.01$), and the greatest amount in the 1:1 dynamic culture ratio ($p < 0.01$). This helps to explain observed proliferation inhibition in coculture. We also observed surface interaction between the Jurkats in monoculture and found that Jurkats on PS-A culture tended to adhere to the aminated surfaces. Further investigation into the soluble and cell-contact mediated interactions would help further

develop the model. The steps taken here show promise with a multicellular system capable of supporting both adherent and circulating cells.

In conclusion, this work demonstrates a method for 3D printing PS to expand adherent and non-adherent cells. With an emphasis placed on the bone marrow niche, we exhibit that surface properties of our substrates direct the protein adhesion and ultimate response to the cultured cells. Using these surface properties, we enhance hMSC growth, osteogenic differentiation, and facilitate dynamic coculture. Understanding these competing factors will lead to the continued development of a bone marrow niche model and complements on-going research. The broader research community is actively seeking to develop meaningful models of this complex environment. A recent study sought to develop a 3D bone marrow adipose-tissue model. Using a silk scaffold, they found significantly different gene expression as compared to 2D culture and observed destructive effects on MSCs from cocultured myeloma cells.[437] Cancer models, such as this one, aim to better understand the mechanistic processes within the bone marrow niche and show promise as a basis for testing immunotherapies rapidly and investigating developed resistance without animal models.[438] Using decellularized scaffolds from xerographic sources (e.g. bovine) also provide an interesting alternative, with high maintenance of the cellular niche and HSC expansion reported.[439] However, using a purely natural biomaterial scaffold could pose challenges when scaled to clinically relevant lot sizes. Continued development of the work presented in this dissertation and engagement with the greater research community could ultimately work towards

developing a widely accepted synthetic standard model for this complex environment, working towards eradicating these detrimental hematological malignancies.

While several surface characteristics were surveyed during this thesis, additional properties could be playing roles in directing cell responses. Surface charging may be acting, either from the surface chemical modification made or as a consequence of substrate charging during plasma treatment. Surface charge could interact with amino acids, as several contain a base charge (negative: aspartic acid, glutamic acid; positive: lysine, arginine, histidine),[440] or dictate protein conformation during adhesion. As well, positively charged substrates have been reported to encourage osteogenic differentiation, increasing the expression of RUNX2, OPN, and OCN as compared to negatively or uncharged surfaces.[441] Further work would investigate the impact of substrate charge in the PS model presented.

Substrate stiffness was not investigated during this thesis with the base material kept constant. Stiff substrates (> 60 kPa) have been implicated in osteogenic differentiation on hydrogel substrates.[442,443] Polystyrene, even after oxidation, is significantly more stiff (e.g. > 1 GPa),[444] but not quite as stiff as bone (> 5 GPa).[445] Further biological mimicry and improvement of the model could be realized by investigating stiffness and texture; whether by generating softer materials to possibly aid in maintaining MSC multipotency or increasing stiffness to mimic the calcified environment, surface stiffness likely plays a role in the bone marrow niche development.[446] Manipulating the cytoskeleton by controlling the geometry / stiffness can activate intercellular signaling working to direct

hMSC fate.[399,442] Continued development of the model could see incorporating these aspects, where the research presented here is a starting point to building a cost effective model for niche generation towards clinical goals.

Clinically, enhancing our understanding of multicellular mechanistic interactions in the bone marrow niche are on-going. A hydrogel engraftment model focuses on the model's ability to support acute myeloid leukemia and shows promise as a means for observing less aggressive cancer subtypes.[447] However, the model relies on a soft hydrogel within a murine model. The model likely has higher maintenance costs as compared to a bioreactor and requires digesting the scaffold to completely to access the enclosed population. Further development of these models and incorporation of compounds could see continued improvement in expanding HSCs *ex vivo*. A novel compound (SR-1) has been shown to aid HSC expansion, with clinical infusions into patients possible, and future work planned to develop a single dosage strategy and understand the compound's impact within the niche.[448] A bone marrow niche model could potentially serve to understand these benchmarks before moving to human clinical trials.

The PS model developed through this dissertation could be improved with continued development of the 3D structure, surface properties, and bioreactor system. However, the knowledge gained presents a viable path for transforming PS from a 2D to a 3D culture substrate with implications on adherent and non-adherent cultures. We suspect the greatest theoretical phenomenon we found during the course of this work is the interconnectivity of various culture stressors. For example, the ability to increase early

osteogenic progression with the synergistic combination of 3D geometry and surface chemistry. These findings bring us to our biggest technological contribution in the field: transforming PS from a ubiquitous culture material to a targeted 3D dynamic culture material. We show that even this simple culture substrate can continue to be improved for specific applications. Continued investigation could see the model expanded to include additional tissue niches and cell types, improving the biomimicry of the cell environment with an easily translatable system for bioreactor culture.

7.2 Contributions

The work presented here has resulted in two first author review articles (one of which is a co-first), one first author research paper, and two first author manuscripts in preparation. My research is included in six additional publications, one first author manuscript in preparation, and has produced four provisional patent filings relating to three projects. This work was supported in part by a National Institute of Standards and Technology (70NANB15H274). The transformation of PS from a 2D to a 3D culture surface has significant implications on transforming standard tissue culture practices and improving biomimicry. The development presented here for custom rapidly manufactured culture scaffolds has implications on increasing the wealth of knowledge in directed cell culture and the fundamental processes that govern cell-material interactions.

7.3 Future directions

This dissertation focused on developing the base plasma treatment, 3D-printing, and bioreactor methods to culture hMSCs and a model non-adherent cell population (Jurkats) towards developing a bone marrow niche model. Future studies could begin with a

redesign of the bioreactor chamber to ease the assembly. While the base material for the chambers (Eshell 300) provides sufficient strength to assembly the structure, redesigning the chamber could ease assembly time and increase the scaffold size which can be accommodated. So long as the porosity of the printed PS scaffold is maintained, we do not expect the surface characteristics to diminish within the bulk of the printed object.

Redesigning the culture chamber could be accompanied by a study investigating the interaction between flow and scaffold geometry. There are a number of other patters, fiber diameters, and geometries which could be explored. These range from completely random to highly structured and ordered. Each of these brings a different element to replicating a niche environment and influencing intercellular signaling. Continued evolution of these patterns may require investigating additional means of delivering plasma to the interior of printed objects, either through a combination printing-plasma system or with a high flow plasma jet. One such investigation could center on a design of experiments method, determining the impact and interaction of parameters to rapidly study a range of scaffold geometries and flow rates. Building a model which looks at bioreactor properties (scaffold surface area, flow rate) and biological (DNA content, osteogenic markers, and multipotency markers) could see the development of bioreactor constructs for targeted applications. For example, looking at the structure function relationship under high shear stress could see to measure total calcification, OPN production, and other related osteogenic differentiation markers. In this dissertation, we investigated a single scaffold design and flow rate, though it is certainly possible different internal structures could produce different outcomes. Previous research has reported that

the curvature of a scaffold influences the distribution and growth kinetics of seeded cells.[449] Expanding this structure-function relationship to include flow rate and directed differentiation could be a next step for this bioreactor model.

To aid in bone marrow niche model development, future work could look to incorporate endothelial cells (e.g. human umbilical vein endothelial cells, HuVECs) in coculture within the model. Endothelial cells have previously been shown to enhance osteogenic markers and organizing a pre-vascular network.[450] Assessing osteogenic markers could look to see how the model progresses in development as a function of flow rate and/or geometry. We expect that increasing the flow rate would increase the development of osteogenic markers, while coculturing with endothelial cells would improving the biomimicry of the niche model. As well, in building towards the bone marrow niche model, assessing the expression of HSC modulatory cytokines in the culture media, such as IL-3, FLT3-L, TPO, SCF, IL-6, and VEGF would give an indication of the success of the MSCs in supporting HSCs in the model.[451] With the aim of expanding multipotent HSCs (i.e. Lin-Sca1+cKit+),[452] the non-adherent cell fraction would need to undergo flow cytometry analysis to understand the phenotype of the circulating population. Validation the model could see a viable multicellular test bed for pharmaceutical testing, an active pursuit proposed by others.[453]

A final proposed direction for this work seeks to develop a standardized test bed for modeling with HSCs. In this work we have shown we can generate amines on the surfaces of PS scaffolds. A method for conjugating stable cytokines to the PS surface

through a linker would be investigated, building on previous work in a hydrogel with covalently linked SCF.[454] The competing molecules and factors[455] within the complex niche would be the tunable biochemical markers incorporated into the test bed. Using a combinatorial, 3D printing-based, approach, concentration gradients and combinations of the small molecules would be deposited onto test substrates. The molecules would be bound to the substrate and observations made with seeded HSCs to assess the productivity of different biochemical combinations in maintaining the multilineage status. Using an imaging-based approach, correlating measured hematopoietic lineage markers to locations within the array would determine successful combinations. Increasing the complexity from a 2D substrate to a defined 3D architecture based on previous investigations would lead to the development of a surface chemically defined, geometry defined, perfusable scaffold for HSCs. Verification of the surface stability of the bound cytokines through aging testing, could see the development of a commercial or research tool with wide clinical appeal. Ultimately, the goal of narrowing and defining culture substrates would be used to bring HSCs into the clinic more broadly.

The background, new research, and future directions presented in this dissertation describe an approach to transform PS from a 2D to a 3D scaffold with defined surface properties for inclusion in dynamic culture models for coculture, aiming to improve the biomimicry of the culture environment. By defining the surface properties, understanding the protein interactions, and building the culture environment, a growth substrate can be built that supports multiple cell types in investigating mechanistic actions of adhered and circulating populations.

Appendix

Image Analysis Program and documentation

```
% ImageProcessingCells, reads in images, reads in size of images, sorts by stack location, opens an image of the cell dots (indicating the % cells locations), color separation, traces outlines, displays areas of cells and statistics of stack, assumes 1024x1024 images

% Read in directory of images, get list of all TIFF files in this directory, DIR returns as a structure array.

imagefiles = dir('*.tif');
nfiles = length(imagefiles);    % Number of files found
images = cell(nfiles,1);
disp('Files Found')
for ii = 1:nfiles
   currentfilename = imagefiles(ii).name;
   currentimage = imread(currentfilename);
   images{ii} = currentimage;
end
disp('Files Read')
% Sort stacks, all stacks will have a known number of images in stack e.g. a 4x4 stack will have 16 separate groups of images, separate by number of images and get maximum image projection for each group
rows = str2double(input('How many rows in set? ', 's'));
cols = str2double(input('How many columns in set? ', 's'));
pxl = str2double(input('What is the image resolution (pixels/um default 1.6516)? ','s'));
thu = str2double(input('What is your threshold area (um^2)? ', 's'));

grps = cell(rows*cols,1);
ngrps = length(grps);

% Convert threshold to pixels
thp = floor((pxl^2)*thu);

%Sort images, and read into maximum images for each images set, define variables for speed
zStack = nfiles/ngrps;
jj = 1;
grpsr = cell(rows*cols,1);
grpsb = cell(rows*cols,1);
grpsrt = cell(rows*cols,1);
grpsbt = cell(rows*cols,1);
hld = zeros(1024,1024,3);
maxImageHoldr = zeros(1024,1024,zStack);
maxImageHoldb = zeros(1024,1024,zStack);
cellarea = zeros(rows*cols,1);
```

```
for ii = 1:ngrps
    for kk = 1:zStack
        % Separate Colors (Blue, Green, Red)
        hld = images{jj};
        thr = graythresh(hld(:,:,1));
        thb = graythresh(hld(:,:,3));

        % Threshold out objects below the intensity threshold, tuned based on individual
images. 0-0.07 Typical.
        if thr < 0.000
            thr = 0.000;
        end

        if thb < 0.000
            thb = 0.000;
        end

        maxImageHoldr(:,:,kk) = imbinarize(hld(:,:,1),thr);
        maxImageHoldb(:,:,kk) = imbinarize(hld(:,:,3),thb);

        jj = jj + 1;

    end
    fprintf('Separated\n')
    % Maximum Image Projection
    grpsr{ii} = max(maxImageHoldr,[],3);
    grpsb{ii} = max(maxImageHoldb,[],3);

    % Threshold out objects below the area threshold
    grpsrt{ii} = bwareaopen(grpsr{ii},thp);
    grpsbt{ii} = bwareaopen(grpsb{ii},thp);
    fprintf('Projected and Thresholded\n')

    figure(ii)
    warning off
    imshowpair(grpsrt{ii},grpsbt{ii},'montage')
    warning on

    % Pull area information from each captured portion, first determine connected
components in the images
    cr = bwconncomp(grpsrt{ii});
    cb = bwconncomp(grpsbt{ii});

    % Find the area of those connected components
    ar = regionprops(cr,'Area');
```

```
    ab = regionprops(cb,'Area');

    % Number of detected nucleii
    nnucleii = length(ab);
    naru = length(ar);
    cella = 0;
    aru = cell(naru,1);
    abu = cell(nnucleii,1);

    for pp = 1:naru

        %Convert to um^2
        aru{pp} = ar(pp).Area./(pxl^2);

        % Area covered by Actin
        cella = cella + aru{pp};
    end

    %Vector computed containing the average area coverage in each stack
    cellarea(ii) = cella/nnucleii;

    fprintf('Layer %d of %d completed, area computed\n',ii,ngrps)
end

% Calculate statistics of stack
marea = mean(cellarea);
stdarea = std(cellarea);

fprintf('The mean of the stack is %d +/- %d.\n',marea,stdarea)
```

References

1. U.S. Cancer Statistics Working Group. United States Cancer Statistics: 1999–2014 Incidence and Mortality Web-based Report. Atlanta U.S. Dep. Heal. Hum. Serv. Centers Dis. Control Prev. Natl. Cancer Institute; 2017. [cited 2017 Aug 8].
2. Kim N, and Cho S-G. Clinical applications of mesenchymal stem cells. Korean J. Intern. Med. **28**, 387, 2013.
3. Kim DW, Chung YJ, Kim TG, Kim YL, and Oh IH. Cotransplantation of third-party mesenchymal stromal cells can alleviate single-donor predominance and increase engraftment from double cord transplantation. Blood. **103**, 1941, 2004.
4. Pittenger MF, Mackay AM, Beck SC, Jaiswal RK, Douglas R, Mosca JD, et al. Multilineage potential of adult human mesenchymal stem cells. Science. **284**, 143, 1999.
5. Mehrasa R, Vaziri H, Oodi A, Khorshidfar M, Nikogoftar M, Golpour M, et al. Mesenchymal stem cells as a feeder layer can prevent apoptosis of expanded hematopoietic stem cells derived from cord blood. Int. J. Mol. Cell. Med. **3**, 1, 2014.
6. Wagner JE, and Gluckman E. Umbilical Cord Blood Transplantation: The First 20 Years. Semin. Hematol. Elsevier Inc.; **47**, 3, 2010.
7. Horwitz EM, Prockop DJ, Fitzpatrick L a, Koo WW, Gordon PL, Neel M, et al. Transplantability and therapeutic effects of bone marrow-derived mesenchymal cells in children with osteogenesis imperfecta. Nat. Med. **5**, 309, 1999.
8. Gragert L, Eapen M, Williams E, Freeman J, Spellman S, Baitty R, et al. HLA Match Likelihoods for Hematopoietic Stem-Cell Grafts in the U.S. Registry. N. Engl. J. Med. **371**, 339, 2014.
9. de Lima M, McNiece I, Robinson SN, Munsell M, Eapen M, Horowitz M, et al. Cord-Blood Engraftment with Ex Vivo Mesenchymal-Cell Coculture. N. Engl. J. Med. **367**, 2305, 2012.
10. US National Library of Medicine. ClinicalTrials.gov. 2019.
11. Uccelli A, Moretta L, and Pistoia V. Mesenchymal stem cells in health and disease. Nat Rev Immunol. Nature Publishing Group; **8**, 726, 2008.
12. Ogawa M, and Article R. Differentiation and Proliferation of Hematopoietic Stem Cells. Blood. **81**, 2844, 1993.
13. Morrison SJ, and Scadden DT. The bone marrow niche for haematopoietic stem cells. Nature. **505**, 327, 2014.
14. Di Maggio N, Piccinini E, Jaworski M, Trumpp A, Wendt DJ, and Martin I. Toward modeling the bone marrow niche using scaffold-based 3D culture systems. Biomaterials. Elsevier Ltd; **32**, 321, 2011.
15. Rodríguez-Pardo V, and Vernot J. Mesenchymal stem cells promote a primitive phenotype CD34+c-kit+ in human cord blood-derived hematopoietic stem cells during ex vivo expansion. Cell. Mol. Biol. Lett. **18**, 2013.
16. Lau SX, Leong YY, Ng WH, Ng AWP, Ismail IS, Yusoff NM, et al. Human mesenchymal stem cells promote CD34 $^{+}$ hematopoietic stem cell proliferation with preserved red blood cell differentiation capacity. Cell Biol. Int. **41**, 697, 2017.
17. Moioli EK, Clark P a., Chen M, Dennis JE, Erickson HP, Gerson SL, et al. Synergistic actions of hematopoietic and mesenchymal stem/progenitor cells in vascularizing bioengineered tissues. PLoS One. **3**, 2008.
18. Bernardo ME, and Fibbe WE. Mesenchymal stromal cells and hematopoietic stem cell transplantation. Immunol. Lett. Elsevier B.V.; **168**, 215, 2015.
19. Fong ELS, Lamhamedi-Cherradi S-E, Burdett E, Ramamoorthy V, Lazar AJ, Kasper FK, et al. Modeling Ewing sarcoma tumors in vitro with 3D scaffolds. Proc. Natl. Acad. Sci. **110**, 6500, 2013.
20. Wang YI, Abaci HE, and Shuler ML. Microfluidic blood–brain barrier model provides in

vivo-like barrier properties for drug permeability screening. Biotechnol. Bioeng. **114**, 184, 2017.
21. Irhimeh MR, Fitton JH, Ko KH, Lowenthal RM, and Nordon RE. Formation of an adherent hematopoietic expansion culture using fucoidan. Ann. Hematol. **90**, 1005, 2011.
22. Stiehler M, Bünger C, Baatrup A, Lind M, Kassem M, and Mygind T. Effect of dynamic 3-D culture on proliferation, distribution, and osteogenic differentiation of human mesenchymal stem cells. J. Biomed. Mater. Res. Part A. **89**, 96, 2008.
23. Chastain SR, Kundu AK, Dhar S, Calvert JW, and Putnam AJ. Adhesion of mesenchymal stem cells to polymer scaffolds occurs via distinct ECM ligands and controls their osteogenic differentiation. J. Biomed. Mater. Res. Part A. **78A**, 73, 2006.
24. Dominici M, Le Blanc K, Mueller I, Slaper-Cortenbach I, Marini F, Krause D, et al. Minimal criteria for defining multipotent mesenchymal stromal cells. The International Society for Cellular Therapy position statement. Cytotherapy. Elsevier; **8**, 315, 2006.
25. Barker SL, and LaRocca PJ. Method of production and control of a commercial tissue culture surface. J. Tissue Cult. Methods. **16**, 151, 1994.
26. Lembong J, Lerman MJ, Kingsbury TJ, Civin CI, and Fisher JP. A Fluidic Culture Platform for Spatially Patterned Cell Growth, Differentiation, and Cocultures. Tissue Eng. Part A. **24**, 1715, 2018.
27. Zhao F, Vaughan TJ, and McNamara LM. Quantification of fluid shear stress in bone tissue engineering scaffolds with spherical and cubical pore architectures. Biomech. Model. Mechanobiol. Springer Berlin Heidelberg; **15**, 561, 2015.
28. Porter B, Zauel R, Stockman H, Guldberg R, and Fyhrie D. 3-D computational modeling of media flow through scaffolds in a perfusion bioreactor. J. Biomech. **38**, 543, 2005.
29. Bancroft GN, Sikavitsas VI, and Mikos AG. Technical Note: Design of a Flow Perfusion Bioreactor System for Bone Tissue-Engineering Applications. Tissue Eng. **9**, 549, 2003.
30. Godara P, McFarland CD, and Nordon RE. Design of bioreactors for mesenchymal stem cell tissue engineering. J. Chem. Technol. Biotechnol. **83**, 408, 2008.
31. Yeatts AB, and Fisher JP. Bone tissue engineering bioreactors: dynamic culture and the influence of shear stress. Bone. **48**, 171, 2011.
32. Zhao F, Chella R, and Ma T. Effects of shear stress on 3-D human mesenchymal stem cell construct development in a perfusion bioreactor system: Experiments and hydrodynamic modeling. Biotechnol. Bioeng. **96**, 584, 2007.
33. Yeatts AB, and Fisher JP. Tubular perfusion system for the long-term dynamic culture of human mesenchymal stem cells. Tissue Eng. Part C Methods. **17**, 337, 2011.
34. Ma T, Tsai A-C, and Liu Y. Biomanufacturing of human mesenchymal stem cells in cell therapy: Influence of microenvironment on scalable expansion in bioreactors. Biochem. Eng. J. Elsevier B.V.; **108**, 44, 2016.
35. Yeatts AB, Both SK, Yang W, Alghamdi HS, Yang F, Fisher JP, et al. In vivo bone regeneration using tubular perfusion system bioreactor cultured nanofibrous scaffolds. Tissue Eng. Part A. **20**, 139, 2014.
36. Derby B. Printing and Prototyping of Tissues and Scaffolds. Science. **338**, 921, 2012.
37. Rubin H. Altering bacteriological plastic petri dishes for tissue culture use. Public Heal. reports (Washington, D.C. 1896). **81**, 843, 1966.
38. Zeiger AS, Hinton B, and Van Vliet KJ. Why the dish makes a difference: quantitative comparison of polystyrene culture surfaces. Acta Biomater. **9**, 7354, 2013.
39. Hecht E. Optics. 3rd ed. Reading, MA: Addison-Wesley; 1998.
40. Teach WC, and Kiessling GC. Polystyrene. 1st ed. New York: Reinhold Publishing Corporation; 1960.
41. Scheirs J, and Priddy DB, editors. Modern Styrenic Polymers: Polystyrenes and Styrenic Copolymers. Chichester, UK: John Wiley & Sons, Ltd; 2003.

42. Utracki LA. History of commercial polymer alloys and blends (from a perspective of the patent literature). Polym. Eng. Sci. **35**, 2, 1995.
43. Razza F, Fieschi M, Innocenti FD, and Bastioli C. Compostable cutlery and waste management: An LCA approach. Waste Manag. Elsevier Ltd; **29**, 1424, 2009.
44. Wunderlich B, Bodily DM, and Kaplan MH. Theory and measurements of the glass-transformation interval of polystyrene. J. Appl. Phys. **35**, 95, 1964.
45. Gibbs JJH, and DiMarzio E a E. Nature of the Glass Transition and the Glassy State. J. Chem. Phys. **28**, 373, 1958.
46. Rieger J. The glass transition temperature of polystyrene. J. Therm. Anal. **46**, 965, 1996.
47. Jean YC, Zhang R, Cao H, Yuan J-P, Huang C-M, Nielsen B, et al. Glass transition of polystyrene near the surface studied by slow-positron-annihilation spectroscopy. Phys. Rev. B. **56**, R8459, 1997.
48. Gadegaard N, Mosler S, and Larsen NB. Biomimetic Polymer Nanostructures by Injection Molding. Macromol. Mater. Eng. **288**, 76, 2003.
49. Jansen KMB, Pantani R, and Titomanlio G. As-molded shrinkage measurements on polystyrene injection molded products. Polym. Eng. Sci. **38**, 254, 1998.
50. Ryan JA. Evolution of Cell Culture Surfaces. BioFiles. **3.8**, 8, 2008.
51. Young EWK, Berthier E, Guckenberger DJ, Sackmann E, Lamers C, Meyvantsson I, et al. Rapid prototyping of arrayed microfluidic systems in polystyrene for cell-based assays. Anal. Chem. **83**, 1408, 2011.
52. Lenhert S, Meier MB, Meyer U, Chi L, and Wiesmann HP. Osteoblast alignment, elongation and migration on grooved polystyrene surfaces patterned by Langmuir-Blodgett lithography. Biomaterials. **26**, 563, 2005.
53. Brown A, Burke GA, and Meenan BJ. Patterned cell culture substrates created by hot embossing of tissue culture treated polystyrene. J. Mater. Sci. Mater. Med. **24**, 2797, 2013.
54. Dusseiller MR, Schlaepfer D, Koch M, Kroschewski R, and Textor M. An inverted microcontact printing method on topographically structured polystyrene chips for arrayed micro-3-D culturing of single cells. Biomaterials. **26**, 5917, 2005.
55. Bhuthalingam R, Lim PQ, Irvine S, Agrawal A, Mhaisalkar P, An J, et al. A novel 3D printing method for cell alignment and differentiation. Int. J. Bioprinting. **1**, 57, 2015.
56. Sun L, Pereira D, Wang Q, Barata DB, Truckenmüller R, Li Z, et al. Controlling Growth and Osteogenic Differentiation of Osteoblasts on Microgrooved Polystyrene Surfaces. Engler AJ, editor. PLoS One. **11**, 1, 2016.
57. Nakamoto T, Wang X, Kawazoe N, and Chen G. Influence of micropattern width on differentiation of human mesenchymal stem cells to vascular smooth muscle cells. Colloids Surfaces B Biointerfaces. Elsevier B.V.; **122**, 316, 2014.
58. Wang N, Naruse K, Stamenovic D, Fredberg JJ, Mijailovich SM, Tolic-Norrelykke IM, et al. Mechanical behavior in living cells consistent with the tensegrity model. Proc. Natl. Acad. Sci. **98**, 7765, 2001.
59. Mathieu PS, and Loboa EG. Cytoskeletal and Focal Adhesion Influences on Mesenchymal Stem Cell Shape, Mechanical Properties, and Differentiation Down Osteogenic, Adipogenic, and Chondrogenic Pathways. Tissue Eng. Part B Rev. **18**, 436, 2012.
60. Yang N, Yang MK, Bi SX, Chen L, Zhu ZY, Gao YT, et al. Cells behaviors and genotoxicity on topological surface. Mater. Sci. Eng. C. **33**, 3465, 2013.
61. Bi S, Yang N, Yang M, He X, Chen L, Zhu Z, et al. Fabrication of polystyrene microscale porous substrate and its effects on HL-7702 cells behaviors. J. Biomed. Mater. Res. - Part A. **102**, 1518, 2014.
62. Horbett TA. The role of adsorbed proteins in animal cell adhesion. Colloids Surfaces B Biointerfaces. **2**, 225, 1994.
63. Tamada Y, and Ikada Y. Cell adhesion to plasma-treated polymer surfaces. Polymer. **34**,

2208, 1993.
64. Skarlatos SI, Rao R, and Kruth HS. Accelerated development of human monocyte-macrophages cultured on Plastek-C tissue culture dishes. J. Tissue Cult. Methods. **14**, 113, 1992.
65. Martin GR, and Rubin H. Effects of cell adhesion to the substratum on the growth of chick embryo fibroblasts. Exp. Cell Res. **85**, 319, 1974.
66. Amstein CF, and Hartman PA. Adaptation of plastic surfaces for tissue culture by glow discharge. J. Clin. Microbiol. **2**, 46, 1975.
67. Maroudas NG. Sulphonated polystyrene as an optimal substratum for the adhesion and spreading of mesenchymal cells in monovalent and divalent saline solutions. J. Cell. Physiol. **90**, 511, 1977.
68. Bentley KL, and Klebe RJ. Fibronectin binding properties of bacteriologic petri plates and tissue culture dishes. J. Biomed. Mater. Res. **19**, 757, 1985.
69. Brash JL, and Horbett TA. Proteins at Interfaces. J. Dispers. Sci. Technol. 1–23, 1995.
70. Iijima K, Suzuki R, Iizuka A, Ueno-Yokohata H, Kiyokawa N, and Hashizume M. Surface functionalization of tissue culture polystyrene plates with hydroxyapatite under body fluid conditions and its effect on differentiation behaviors of mesenchymal stem cells. Colloids Surfaces B Biointerfaces. **147**, 351, 2016.
71. Iijima K, Iizuka A, Suzuki R, Ueno-Yokohata H, Kiyokawa N, and Hashizume M. Effect of protein adsorption layers and solution treatments on hydroxyapatite deposition on polystyrene plate surfaces in simulated body fluids. J. Mater. Sci. Mater. Med. **28**, 193, 2017.
72. Curran JM, Chen R, and Hunt JA. Controlling the phenotype and function of mesenchymal stem cells in vitro by adhesion to silane-modified clean glass surfaces. Biomaterials. **26**, 7057, 2005.
73. Arifin MA, Mel M, Samsudin N, Hashim YZH, Salleh HM, Sopyan I, et al. Ultraviolet/ozone treated polystyrene microcarriers for animal cell culture. J. Chem. Technol. Biotechnol. **91**, 2607, 2016.
74. Grace JM, and Gerenser LJ. Plasma Treatment of Polymers. J. Dispers. Sci. Technol. **24**, 305, 2003.
75. Lee J-H, Kwon J-S, Kim Y-H, Choi E-H, Kim K-M, and Kim K-N. The effects of enhancing the surface energy of a polystyrene plate by air atmospheric pressure plasma jet on early attachment of fibroblast under moving incubation. Thin Solid Films. **547**, 99, 2013.
76. Kleinhans C, Barz J, Wurster S, Willig M, Oehr C, Müller M, et al. Ammonia plasma treatment of polystyrene surfaces enhances proliferation of primary human mesenchymal stem cells and human endothelial cells. Biotechnol. J. **8**, 327, 2013.
77. Ertel SI, Chilkoti A, Horbetti TA, and Ratner BD. Endothelial cell growth on oxygen-containing films deposited by radio-frequency plasmas: the role of surface carbonyl groups. J. Biomater. Sci. Polym. Ed. **3**, 163, 1992.
78. Tunma S, Inthanon K, Chaiwong C, Pumchusak J, Wongkham W, and Boonyawan D. Improving the attachment and proliferation of umbilical cord mesenchymal stem cells on modified polystyrene by nitrogen-containing plasma. Cytotechnology. **65**, 119, 2013.
79. Teare DOH, Emmison N, and Bradley RH. Cellular Attachment to Ultraviolet Ozone Modified Polystyrene Surfaces. Langmuir. **16**, 2818, 2000.
80. Nakayama Y, Takahagi T, Soeda F, Hatada K, Nagaoka S, Suzuki J, et al. XPS analysis of NH3 plasma-treated polystyrene films utilizing gas phase chemical modification. J. Polym. Sci. Part A Polym. Chem. **26**, 559, 1988.
81. Schamberger PC, Abes JI, and Gardella JA. Surface chemical studies of aging and solvent extraction effects on plasma-treated polystyrene. Colloids Surfaces B Biointerfaces. **3**,

203, 1994.
82. Dupont-Gillain CC, Nysten B, Hlady V, and Rouxhet PG. Atomic Force Microscopy and Wettability Study of Oxidized Patterns at the Surface of Polystyrene. J. Colloid Interface Sci. **220**, 163, 1999.
83. Van Kooten TG, Spijker HT, and Busscher HJ. Plasma-treated polystyrene surfaces: Model surfaces for studying cell-biomaterial interactions. Biomaterials. **25**, 1735, 2004.
84. Arima Y, and Iwata H. Effect of wettability and surface functional groups on protein adsorption and cell adhesion using well-defined mixed self-assembled monolayers. Biomaterials. **28**, 3074, 2007.
85. Curtis ASG, Forrester J V, Mclnnes C, and Lawrie F. Adhesion of Cells to Polystyrene Surfaces. J. Cell Biol. **97**, 1500, 1983.
86. Verdanova M, Sauerova P, Hempel U, and Hubalek M. Initial cell adhesion of three cell types in the presence and absence of serum proteins. Histochem. Cell Biol. Springer Berlin Heidelberg; **148**, 273, 2017.
87. Kondyurin A, Gan BK, Bilek MMM, Mizuno K, and McKenzie DR. Etching and structural changes of polystyrene films during plasma immersion ion implantation from argon plasma. Nucl. Instruments Methods Phys. Res. Sect. B Beam Interact. with Mater. Atoms. **251**, 413, 2006.
88. Lee Y, Han S, Lee J-H, Yoon J-H, Lim HE, and Kim K-J. Surface studies of plasma source ion implantation treated polystyrene. J. Vac. Sci. Technol. A Vacuum, Surfaces, Film. **16**, 1710, 1998.
89. Maroudas NG. Adhesion and spreading of cells on charged surfaces. J. Theor. Biol. Academic Press; **49**, 417, 1975.
90. Zhao Y, Tang S, Myung SW, Lu N, and Choi HS. Effect of washing on surface free energy of polystyrene plate treated by RF atmospheric pressure plasma. Polym. Test. **25**, 327, 2006.
91. Bruce RL, Weilnboeck F, Lin T, Phaneuf RJ, Oehrlein GS, Long BK, et al. Relationship between nanoscale roughness and ion-damaged layer in argon plasma exposed polystyrene films. J. Appl. Phys. **107**, 084310, 2010.
92. Biazar E, Heidari M, Asefnejad A, Asefnezhad A, and Montazeri N. The relationship between cellular adhesion and surface roughness in polystyrene modified by microwave plasma radiation. Int. J. Nanomedicine. **6**, 631, 2011.
93. Bonaccurso E, and Graf K. Nanostructuring Effect of Plasma and Solvent Treatment on Polystyrene. Langmuir. **20**, 11183, 2004.
94. Smirnov A V., Atkin VS, Gorbachev IA, Grebennikov AI, Sinev I V., and Simakov V V. Surface Modification of Polystyrene Thin Films by RF Plasma Treatment. Bionanoscience. BioNanoScience; **7**, 680, 2017.
95. Teixeira AI, Abrams GA, Bertics PJ, Murphy CJ, and Nealey PF. Epithelial contact guidance on well-defined micro- and nanostructured substrates. J. Cell Sci. **116**, 1881, 2003.
96. Weikart CM, and Yasuda HK. Modification , Degradation , and Stability of Polymeric Surfaces Treated with Reactive Plasmas. J. Polym. Sci. Part A Polym. Chem. **38**, 3028, 2000.
97. Onyiriuka EC, Hersch LS, and Hertl W. Solubilization of corona discharge- and plasma-treated polystyrene. J. Colloid Interface Sci. **144**, 98, 1991.
98. Tourovskaia A, Barber T, Wickes BT, Hirdes D, Grin B, Castner DG, et al. Micropatterns of Chemisorbed Cell Adhesion-Repellent Films Using Oxygen Plasma Etching and Elastomeric Masks. Langmuir. **19**, 4754, 2003.
99. Mitchell SA, Emmison N, and Shard AG. Spatial control of cell attachment using plasma micropatterned polymers. Surf. Interface Anal. **33**, 742, 2002.

100. Detrait E, Lhoest J-B, Knoops B, Bertrand P, and van den Bosch de Aguilar P. Orientation of cell adhesion and growth on patterned heterogeneous polystyrene surface. J. Neurosci. Methods. **84**, 193, 1998.
101. Doherty KG, Oh J-S, Unsworth P, Bowfield A, Sheridan CM, Weightman P, et al. Polystyrene Surface Modification for Localized Cell Culture Using a Capillary Dielectric Barrier Discharge Atmospheric-Pressure Microplasma Jet. Plasma Process. Polym. **10**, 978, 2013.
102. Yu Q, Zhang Y, Chen H, Zhou F, Wu Z, Huang H, et al. Protein adsorption and cell adhesion/detachment behavior on dual-responsive silicon surfaces modified with poly(N-isopropylacrylamide)-block-polystyrene copolymer. Langmuir. **26**, 8582, 2010.
103. Beaulieu I, Geissler M, and Mauzeroll J. Oxygen plasma treatment of polystyrene and zeonor: Substrates for adhesion of patterned cells. Langmuir. **25**, 7169, 2009.
104. Ando A, Asano T, Urisu T, and Hamaguchi S. Micro-pattern formation of extracellular matrix (ECM) layers by atmospheric-pressure plasmas and cell culture on the patterned ECMs. J. Phys. D. Appl. Phys. **44**, 482002, 2011.
105. Davies J, Nunnerley CS, Brisley AC, Sunderland RF, Edwards JC, Krüger P, et al. Argon plasma treatment of polystyrene microtiter wells. Chemical and physical characterisation by contact angle, ToF-SIMS, XPS and STM. Colloids Surfaces A Physicochem. Eng. Asp. **174**, 287, 2000.
106. Ramsey W, Hertl W, Nowlan E, and Binkowski N. Surface treatments and cell attachment. Vitr. Cell. Dev. Biol. **20**, 802, 1984.
107. De Geyter N, Morent R, Desmet T, Trentesaux M, Gengembre L, Dubruel P, et al. Plasma modification of polylactic acid in a medium pressure DBD. Surf. Coatings Technol. **204**, 3272, 2010.
108. Dowling DP, Miller IS, Ardhaoui M, and Gallagher WM. Effect of Surface Wettability and Topography on the Adhesion of Osteosarcoma Cells on Plasma-modified Polystyrene. J. Biomater. Appl. **26**, 327, 2011.
109. Ulman A. Formation and Structure of Self-Assembled Monolayers. Chem. Rev. **96**, 1533, 1996.
110. Kim M, Schmitt SK, Choi JW, Krutty JD, and Gopalan P. From self-assembled monolayers to coatings: Advances in the synthesis and nanobio applications of polymer brushes. Polymers (Basel). **7**, 1346, 2015.
111. Okano T, Yamada N, Sakai H, and Sakurai Y. A novel recovery system for cultured cells using plasma-treated polystyrene dishes grafted with poly(N-isopropylacrylamide). J. Biomed. Mater. Res. **27**, 1243, 1993.
112. Nishida K, Yamato M, Hayashida Y, Watanabe K, Maeda N, Watanabe H, et al. Functional bioengineered corneal epithellial sheet grafts from corneal stem cells expanded ex vivo on a temperature-responsive cell culture surface. Transplantation. **77**, 379, 2004.
113. Shimizu T, Yamato M, Isoi Y, Akutsu T, Setomaru T, Abe K, et al. Fabrication of pulsatile cardiac tissue grafts using a novel 3-dimensional cell sheet manipulation technique and temperature-responsive cell culture surfaces. Circ. Res. **90**, e40, 2002.
114. Chen Y, Gao Q, Wan H, Yi J, Wei Y, and Liu P. Surface modification and biocompatible improvement of polystyrene film by Ar, O2 and Ar + O2 plasma. Appl. Surf. Sci. **265**, 452, 2013.
115. Zammatteo N, Girardeaux C, Delforge D, Pireaux JJ, and Remacle J. Amination of polystyrene microwells: application to the covalent grafting of DNA probes for hybridization assays. Anal. Biochem. **236**, 85, 1996.
116. Jana NR, and Ying JY. Synthesis of Functionalized Au Nanoparticles for Protein Detection. Adv. Mater. **20**, 430, 2008.
117. Wang L, Bao J, Wang L, Zhang F, and Li Y. One-Pot Synthesis and Bioapplication of

Amine-Functionalized Magnetite Nanoparticles and Hollow Nanospheres. Chem. - A Eur. J. **12**, 6341, 2006.
118. Gale DK, Gutu T, Jiao J, Chang C-H, and Rorrer GL. Photoluminescence Detection of Biomolecules by Antibody-Functionalized Diatom Biosilica. Adv. Funct. Mater. **19**, 926, 2009.
119. Yang X, Zhu L-W, Wan L-S, Zhang J, and Xu Z-K. Surface functionalization of cross-linked polystyrene microspheres via thiol–ene "click" reaction and assembly in honeycomb films for lectin recognition. J. Mater. Res. **28**, 1, 2013.
120. Renault JP, Bernard A, Bietsch A, Michel B, Bosshard HR, Delamarche E, et al. Fabricating arrays of single protein molecules on glass using microcontact printing. J. Phys. Chem. B. **107**, 703, 2003.
121. Hattori K, Sugiura S, and Kanamori T. On-chip cell culture on a microarray of extracellular matrix with surface modification of poly(dimethylsiloxane). Biotechnol. J. **5**, 463, 2010.
122. Alom Ruiz S, and Chen CS. Microcontact printing: A tool to pattern. Soft Matter. **3**, 168, 2007.
123. Pfleger BF, Pitera DJ, Smolke CD, and Keasling JD. Combinatorial engineering of intergenic regions in operons tunes expression of multiple genes. Nat. Biotechnol. **24**, 1027, 2006.
124. Papin JA, Stelling J, Price ND, Klamt S, Schuster S, and Palsson BO. Comparison of network-based pathway analysis methods. Trends Biotechnol. **22**, 400, 2004.
125. Uyar T, and Besenbacher F. Electrospinning of uniform polystyrene fibers: The effect of solvent conductivity. Polymer (Guildf). **49**, 5336, 2008.
126. Kolesky DB, Homan KA, Skylar-Scott MA, and Lewis JA. Three-dimensional bioprinting of thick vascularized tissues. Proc. Natl. Acad. Sci. U. S. A. **113**, 3179, 2016.
127. Holmes B, Zhu W, Li J, Lee JD, and Zhang LG. Development of Novel Three-Dimensional Printed Scaffolds for Osteochondral Regeneration. Tissue Eng. Part A. **21**, 403, 2015.
128. Ozbolat IT, and Hospodiuk M. Current advances and future perspectives in extrusion-based bioprinting. Biomaterials. **76**, 321, 2016.
129. Leber J, Barekzai J, Blumenstock M, Pospisil B, Salzig D, and Czermak P. Microcarrier choice and bead-to-bead transfer for human mesenchymal stem cells in serum-containing and chemically defined media. Process Biochem. **59**, 255, 2017.
130. Choi SH, Kim YH, Hebisch M, Sliwinski C, Lee S, D'Avanzo C, et al. A three-dimensional human neural cell culture model of Alzheimer's disease. Nature. Nature Publishing Group; **515**, 274, 2014.
131. Vanderburgh J, Sterling JA, and Guelcher SA. 3D Printing of Tissue Engineered Constructs for In Vitro Modeling of Disease Progression and Drug Screening. Ann. Biomed. Eng. **45**, 164, 2017.
132. Chambers KF, Mosaad EMO, Russell PJ, Clements JA, and Doran MR. 3D cultures of prostate cancer cells cultured in a novel high-throughput culture platform are more resistant to chemotherapeutics compared to cells cultured in monolayer. PLoS One. **9**, 2014.
133. Ball O, Nguyen B-NB, Placone JK, and Fisher JP. 3D Printed Vascular Networks Enhance Viability in High-Volume Perfusion Bioreactor. Ann. Biomed. Eng. **44**, 3435, 2016.
134. Nguyen B-NB, Ko H, Moriarty RA, Etheridge JM, and Fisher JP. Dynamic Bioreactor Culture of High Volume Engineered Bone Tissue. Tissue Eng. Part A. **22**, 263, 2016.
135. Zhao J, Griffin M, Cai J, Li S, Bulter PEM, and Kalaskar DM. Bioreactors for tissue engineering: An update. Biochem. Eng. J. **109**, 268, 2016.
136. Nargang TM, Brockmann L, Nikolov PM, Schild D, Helmer D, Keller N, et al. Liquid

polystyrene: a room-temperature photocurable soft lithography compatible pour-and-cure-type polystyrene. Lab Chip. **14**, 2698, 2014.
137. Chan CY, Goral VN, DeRosa ME, Huang TJ, and Yuen PK. A polystyrene-based microfluidic device with threedimensional interconnected microporous walls for perfusion cell culture. Biomicrofluidics. **8**, 2014.
138. Dias MR, Fernandes PR, Guedes JM, and Hollister SJ. Permeability analysis of scaffolds for bone tissue engineering. J. Biomech. **45**, 938, 2012.
139. dos Santos FF, Andrade PZ, da Silva CL, and Cabral JMS. Bioreactor design for clinical-grade expansion of stem cells. Biotechnol. J. **8**, 644, 2013.
140. Rumpler M, Woesz A, Dunlop JWC, van Dongen JT, and Fratzl P. The effect of geometry on three-dimensional tissue growth. J. R. Soc. Interface. **5**, 1173, 2008.
141. Knychala J, Bouropoulos N, Catt CJ, Katsamenis OL, Please CP, and Sengers BG. Pore geometry regulates early stage human bone marrow cell tissue formation and organisation. Ann. Biomed. Eng. **41**, 917, 2013.
142. Jarusuwannapoom T, Hongrojjanawiwat W, Jitjaicham S, Wannatong L, Nithitanakul M, Pattamaprom C, et al. Effect of solvents on electro-spinnability of polystyrene solutions and morphological appearance of resulting electrospun polystyrene fibers. Eur. Polym. J. **41**, 409, 2005.
143. Boudriot U, Dersch R, Greiner A, and Wendorff JH. Electrospinning Approaches Toward Scaffold Engineering-A Brief Overview. Artif. Organs. **30**, 785, 2006.
144. Yang F, Murugan R, Wang S, and Ramakrishna S. Electrospinning of nano/micro scale poly(l-lactic acid) aligned fibers and their potential in neural tissue engineering. Biomaterials. **26**, 2603, 2005.
145. Sun T, Mai S, Norton D, Haycock JW, Ryan AJ, and MacNeil S. Self-organization of skin cells in three-dimensional electrospun polystyrene scaffolds. Tissue Eng. **11**, 1023, 2005.
146. Leong MF, Lu HF, Lim TC, Du C, Ma NKL, and Wan ACA. Electrospun polystyrene scaffolds as a synthetic substrate for xeno-free expansion and differentiation of human induced pluripotent stem cells. Acta Biomater. Acta Materialia Inc.; **46**, 266, 2016.
147. Luo Y, Nartker S, Miller H, Hochhalter D, Wiederoder M, Wiederoder S, et al. Surface functionalization of electrospun nanofibers for detecting E. coli O157:H7 and BVDV cells in a direct-charge transfer biosensor. Biosens. Bioelectron. **26**, 1612, 2010.
148. Yoo HS, Kim TG, and Park TG. Surface-functionalized electrospun nanofibers for tissue engineering and drug delivery. Adv. Drug Deliv. Rev. Elsevier B.V.; **61**, 1033, 2009.
149. Casper CL, and Stephens JS. Controlling Surface Morphology of Electrospun Polysterene Fibers: Effect of Humidity and Molecular Weight in Electrospinning Process. Macromolecules. **37**, 573, 2004.
150. Pai CL, Boyce MC, and Rutledge GC. Morphology of porous and wrinkled fibers of polystyrene electrospun from dimethylformamide. Macromolecules. **42**, 2102, 2009.
151. Beyler CL, and Hirschler MM. Thermal Decomposition of Polymers. SFPE Handb. Fire Prot. Eng. 2nd. Quincy, Mass: National Fire Projection Association; 110–31, 1995.
152. Gross BC, Anderson KB, Meisel JE, McNitt MI, and Spence DM. Polymer Coatings in 3D-Printed Fluidic Device Channels for Improved Cellular Adherence Prior to Electrical Lysis. Anal. Chem. **87**, 6335, 2015.
153. Caicedo-Carvajal CE, Liu Q, Remache Y, Goy A, and Suh KS. Cancer Tissue Engineering: A Novel 3D Polystyrene Scaffold for In Vitro Isolation and Amplification of Lymphoma Cancer Cells from Heterogeneous Cell Mixtures. J. Tissue Eng. **2011**, 362326, 2011.
154. Bartnikowski M, Klein TJ, Melchels FPW, and Woodruff MA. Effects of scaffold architecture on mechanical characteristics and osteoblast response to static and perfusion bioreactor cultures. Biotechnol. Bioeng. **111**, 1440, 2014.

155. Cioffi M, Küffer J, Ströbel S, Dubini G, Martin I, and Wendt D. Computational evaluation of oxygen and shear stress distributions in 3D perfusion culture systems: Macro-scale and micro-structured models. J. Biomech. **41**, 2918, 2008.
156. Guo T, Yu L, Lim CG, Goodley AS, Xiao X, Placone JK, et al. Effect of Dynamic Culture and Periodic Compression on Human Mesenchymal Stem Cell Proliferation and Chondrogenesis. Ann. Biomed. Eng. **44**, 2103, 2016.
157. Reinwald Y, Leonard KHLL, Henstock JR, Whiteley JP, Osborne JM, Waters SL, et al. Evaluation of the growth environment of a hydrostatic force bioreactor for preconditioning of tissue-engineered constructs. Tissue Eng. Part C Methods. **21**, 1, 2015.
158. Zhao F, Pathi P, Grayson W, Xing Q, Locke BR, and Ma T. Effects of oxygen transport on 3-D human mesenchymal stem cell metabolic activity in perfusion and static cultures: Experiments and mathematical model. Biotechnol. Prog. **21**, 1269, 2005.
159. Osiecki MJ, Michl TD, Kul Babur B, Kabiri M, Atkinson K, Lott WB, et al. Packed Bed Bioreactor for the Isolation and Expansion of Placental-Derived Mesenchymal Stromal Cells. PLoS One. **10**, 1, 2015.
160. Varani J, Josephs S, and Hillegas WJ. Human diploid fibroblast growth on polystyrene microcarriers in aggregates. Cytotechnology. **22**, 111, 1996.
161. Loffredo F, Mauro ADG Del, Burrasca G, La Ferrara V, Quercia L, Massera E, et al. Ink-jet printing technique in polymer/carbon black sensing device fabrication. Sensors Actuators, B Chem. **143**, 421, 2009.
162. Paine AJ, Luymes W, and McNulty J. Dispersion polymerization of styrene in polar solvents. 6. Influence of reaction parameters on particle size and molecular weight in poly(N-vinylpyrrolidone)-stabilized reactions. Macromolecules. **23**, 3104, 1990.
163. Hervy M, Weber JL, Pecheul M, Dolley-Sonneville P, Henry D, Zhou Y, et al. Long Term Expansion of Bone Marrow-Derived hMSCs on Novel Synthetic Microcarriers in Xeno-Free, Defined Conditions. Pant AB, editor. PLoS One. **9**, 1, 2014.
164. Lunov O, Syrovets T, Loos C, Nienhaus GU, Mailänder V, Landfester K, et al. Amino-Functionalized Polystyrene Nanoparticles Activate the NLRP3 Inflammasome in Human Macrophages. ACS Nano. **5**, 9648, 2011.
165. Fan Y, Zhang F, and Tzanakakis ES. Engineering Xeno-Free Microcarriers with Recombinant Vitronectin, Albumin and UV Irradiation for Human Pluripotent Stem Cell Bioprocessing. ACS Biomater. Sci. Eng. **3**, 1510, 2017.
166. Salzig D. Enzymatic Detachment of Therapeutic Mesenchymal Stromal Cells Grown on Glass Carriers in a Bioreactor. Open Biomed. Eng. J. **7**, 147, 2013.
167. Zhang P, Dou H, Li W, Tao K, Xing B, and Sun K. Fabrication of Fluorescent and Magnetic Multifunctional Polystyrene Microbeads with Carboxyl Ends. Chem. Lett. **36**, 1458, 2007.
168. Kye EJ, Kim S-J, Park MH, Moon HJ, Ryu KH, and Jeong B. Differentiation of Tonsil-Tissue-Derived Mesenchymal Stem Cells Controlled by Surface-Functionalized Microspheres in PEG-Polypeptide Thermogels. Biomacromolecules. **15**, 2180, 2014.
169. Wang X-Y, Pichl C, Gabor F, and Wirth M. A novel cell-based microfluidic multichannel setup—impact of hydrodynamics and surface characteristics on the bioadhesion of polystyrene microspheres. Colloids Surfaces B Biointerfaces. **102**, 849, 2013.
170. Sánchez-Martín RM, Alexander L, and Bradley M. Multifunctionalized biocompatible microspheres for sensing. Ann. N. Y. Acad. Sci. **1130**, 207, 2008.
171. Zauner W, Farrow NA, and Haines AM. In vitro uptake of polystyrene microspheres: effect of particle size, cell line and cell density. J. Control. Release. **71**, 39, 2001.
172. Kalogianni DP, Litos IK, Christopoulos TK, and Ioannou PC. Dipstick-type biosensor for visual detection of DNA with oligonucleotide-decorated colored polystyrene microspheres as reporters. Biosens. Bioelectron. **24**, 1811, 2009.

173. Pappo J, Ermak TH, and Steger HJ. Monoclonal antibody-directed targeting of fluorescent polystyrene microspheres to Peyer's patch M cells. Immunology. **73**, 277, 1991.
174. Dorie MJ, Kallman RF, Rapacchietta DF, Van Antwerp D, and Huang YR. Migration and internalization of cells and polystyrene microspheres in tumor cell spheroids. Exp. Cell Res. **141**, 201, 1982.
175. Fan Y, Hsiung M, Cheng C, and Tzanakakis ES. Facile engineering of xeno-free microcarriers for the scalable cultivation of human pluripotent stem cells in stirred suspension. Tissue Eng. Part A. **20**, 1, 2013.
176. Kehoe DE, Jing D, Lock LT, and Tzanakakis ES. Scalable stirred-suspension bioreactor culture of human pluripotent stem cells. Tissue Eng. Part A. **16**, 405, 2010.
177. Santos F dos, Andrade PZ, Abecasis MM, Gimble JM, Chase LG, Campbell AM, et al. Toward a Clinical-Grade Expansion of Mesenchymal Stem Cells from Human Sources: A Microcarrier-Based Culture System Under Xeno-Free Conditions. Tissue Eng. Part C Methods. **17**, 1201, 2011.
178. Tengvall P, Jansson E, Askendal A, Thomsen P, and Gretzer C. Preparation of multilayer plasma protein films on silicon by EDC/NHS coupling chemistry. Colloids Surfaces B Biointerfaces. **28**, 261, 2003.
179. US National Library of Medicine. ClinicalTrials.gov. ClinicalTrials.gov. 2018 [cited 2018 Feb 26].
180. US Food and Drug Administration. 510(k) Premarket Notification. 510 Premarket Notif. 2018 [cited 2018 May 4].
181. Cui H, Nowicki M, Fisher JP, and Zhang LG. 3D Bioprinting for Organ Regeneration. Adv. Healthc. Mater. **6**, 2017.
182. Turner BN, Strong R, and Gold SA. A review of melt extrusion additive manufacturing processes: I. Process design and modeling. Rapid Prototyp. J. **20**, 192, 2014.
183. Melchels FPW, Feijen J, and Grijpma DW. A review on stereolithography and its applications in biomedical engineering. Biomaterials. Elsevier Ltd; **31**, 6121, 2010.
184. Zhou X, Hou Y, and Lin J. A review on the processing accuracy of two-photon polymerization. AIP Adv. **5**, 030701, 2015.
185. Shirazi SFS, Gharehkhani S, Mehrali M, Yarmand H, Metselaar HSC, Adib Kadri N, et al. A review on powder-based additive manufacturing for tissue engineering: Selective laser sintering and inkjet 3D printing. Sci. Technol. Adv. Mater. **16**, 2015.
186. Gokuldoss PK, Kolla S, and Eckert J. Additive manufacturing processes: Selective laser melting, electron beam melting and binder jetting-selection guidelines. Materials (Basel). **10**, 2017.
187. Goyanes A, Buanz ABM, Basit AW, and Gaisford S. Fused-filament 3D printing (3DP) for fabrication of tablets. Int. J. Pharm. **476**, 88, 2014.
188. Skowyra J, Pietrzak K, and Alhnan MA. Fabrication of extended-release patient-tailored prednisolone tablets via fused deposition modelling (FDM) 3D printing. Eur. J. Pharm. Sci. **68**, 11, 2015.
189. Goyanes A, Chang H, Sedough D, Hatton GB, Wang J, Buanz A, et al. Fabrication of controlled-release budesonide tablets via desktop (FDM) 3D printing. Int. J. Pharm. **496**, 414, 2015.
190. Khaled SA, Burley JC, Alexander MR, and Roberts CJ. Desktop 3D printing of controlled release pharmaceutical bilayer tablets. Int. J. Pharm. Elsevier B.V.; **461**, 105, 2014.
191. Goyanes A, Buanz ABM, Hatton GB, Gaisford S, and Basit AW. 3D printing of modified-release aminosalicylate (4-ASA and 5-ASA) tablets. Eur. J. Pharm. Biopharm. **89**, 157, 2015.
192. Boetker J, Water JJ, Aho J, Arnfast L, Bohr A, and Rantanen J. Modifying release characteristics from 3D printed drug-eluting products. Eur. J. Pharm. Sci. Elsevier B.V.;

90, 47, 2016.
193. Sadia M, Sośnicka A, Arafat B, Isreb A, Ahmed W, Kelarakis A, et al. Adaptation of pharmaceutical excipients to FDM 3D printing for the fabrication of patient-tailored immediate release tablets. Int. J. Pharm. **513**, 659, 2016.
194. Pietrzak K, Isreb A, and Alhnan MA. A flexible-dose dispenser for immediate and extended release 3D printed tablets. Eur. J. Pharm. Biopharm. Elsevier B.V.; **96**, 380, 2015.
195. Khaled SA, Burley JC, Alexander MR, Yang J, and Roberts CJ. 3D printing of tablets containing multiple drugs with defined release profiles. Int. J. Pharm. **494**, 643, 2015.
196. Melocchi A, Parietti F, Maroni A, Foppoli A, Gazzaniga A, and Zema L. Hot-melt extruded filaments based on pharmaceutical grade polymers for 3D printing by fused deposition modeling. Int. J. Pharm. **509**, 255, 2016.
197. Alhijjaj M, Belton P, and Qi S. An investigation into the use of polymer blends to improve the printability of and regulate drug release from pharmaceutical solid dispersions prepared via fused deposition modeling (FDM) 3D printing. Eur. J. Pharm. Biopharm. **108**, 111, 2016.
198. Lim SH, Chia SMY, Kang L, and Yap KYL. Three-Dimensional Printing of Carbamazepine Sustained-Release Scaffold. J. Pharm. Sci. **105**, 2155, 2016.
199. Zieverink J. FDA Approves the First 3D Printed Drug Product. Aprecia Pharm. Co. 2015.
200. Zipdose Technology. [cited 2019 Mar 13].
201. Holländer J, Genina N, Jukarainen H, Khajeheian M, Rosling A, Mäkilä E, et al. Three-Dimensional Printed PCL-Based Implantable Prototypes of Medical Devices for Controlled Drug Delivery. J. Pharm. Sci. **105**, 2665, 2016.
202. Genina N, Holländer J, Jukarainen H, Mäkilä E, Salonen J, and Sandler N. Ethylene vinyl acetate (EVA) as a new drug carrier for 3D printed medical drug delivery devices. Eur. J. Pharm. Sci. Elsevier B.V.; **90**, 53, 2016.
203. Sandler N, Salmela I, Fallarero A, Rosling A, Khajeheian M, Kolakovic R, et al. Towards fabrication of 3D printed medical devices to prevent biofilm formation. Int. J. Pharm. **459**, 62, 2014.
204. Antoni D, Burckel H, Josset E, and Noel G. Three-Dimensional Cell Culture: A Breakthrough in Vivo. Int. J. Mol. Sci. **16**, 5517, 2015.
205. Liu X, Liu R, Cao B, Ye K, Li S, Gu Y, et al. Subcellular cell geometry on micropillars regulates stem cell differentiation. Biomaterials. Elsevier Ltd; **111**, 27, 2016.
206. Alias MA, and Buenzli PR. Modeling the Effect of Curvature on the Collective Behavior of Cells Growing New Tissue. Biophys. J. Biophysical Society; **112**, 193, 2017.
207. Aizawa Y, Owen SC, and Shoichet MS. Polymers used to influence cell fate in 3D geometry: New trends. Prog. Polym. Sci. **37**, 645, 2012.
208. Lerman MJ, Lembong J, Muramoto S, Gillen G, and Fisher JP. The Evolution of Polystyrene as a Cell Culture Material. Tissue Eng. Part B Rev. **24**, 359, 2018.
209. Castilho M, Dias M, Gbureck U, Groll J, Fernandes P, Pires I, et al. Fabrication of computationally designed scaffolds by low temperature 3D printing. Biofabrication. **5**, 2013.
210. Roohani-Esfahani S-I, Newman P, and Zreiqat H. Design and Fabrication of 3D printed Scaffolds with a Mechanical Strength Comparable to Cortical Bone to Repair Large Bone Defects. Sci. Rep. **6**, 19468, 2016.
211. Leukers B, Gülkan H, Irsen SH, Milz S, Tille C, Seitz H, et al. Biocompatibility of ceramic scaffolds for bone replacement made by 3D printing. Materwiss. Werksttech. **36**, 781, 2005.
212. Taboas JM, Maddox RD, Krebsbach PH, and Hollister SJ. Indirect solid free form fabrication of local and global porous, biomimetic and composite 3D polymer-ceramic

scaffolds. Biomaterials. **24**, 181, 2003.
213. Wallace J, Wang MO, Thompson P, Busso M, Belle V, Mammoser N, et al. Validating continuous digital light processing (cDLP) additive manufacturing accuracy and tissue engineering utility of a dye-initiator package. Biofabrication. **6**, 2014.
214. Huang TQ, Qu X, Liu J, and Chen S. 3D printing of biomimetic microstructures for cancer cell migration. Biomed. Microdevices. **16**, 127, 2014.
215. Hollister SJ. Porous scaffold design for tissue engineering. Nat Mater. **4**, 518, 2005.
216. Alvarez-Barreto JF, and Sikavitsas VI. Improved mesenchymal stem cell seeding on RGD-modified poly(L-lactic acid) scaffolds using flow perfusion. Macromol. Biosci. **7**, 579, 2007.
217. Alvarez-Barreto JF, Linehan SM, Shambaugh RL, and Sikavitsas VI. Flow perfusion improves seeding of tissue engineering scaffolds with different architectures. Ann. Biomed. Eng. **35**, 429, 2007.
218. Wendt D, Marsano A, Jakob M, Heberer M, and Martin I. Oscillating perfusion of cell suspensions through three-dimensional scaffolds enhances cell seeding efficiency and uniformity. Biotechnol. Bioeng. **84**, 205, 2003.
219. Grayson WL, Bhumiratana S, Cannizzaro C, Chao P-HG, Lennon DP, Caplan AI, et al. Effects of Initial Seeding Density and Fluid Perfusion Rate on Formation of Tissue-Engineered Bone. Tissue Eng. Part A. **11**, 1809, 2008.
220. Michael Shin, Yoshimoto H, and Vacanti JP. In Vivo Bone Tissue Engineering Using Mesenchymal Stem Cells on a Novel Electrospun Nanofibrous Scaffold. Tissue Eng. **10**, 33, 2004.
221. Yang J, Cao C, Wang W, Tong X, Shi D, Wu F, et al. Proliferation and osteogenesis of immortalized bone marrow-derived mesenchymal stem cells in porous polylactic glycolic acid scaffolds under perfusion culture. J. Biomed. Mater. Res. A. **92**, 817, 2010.
222. Mygind T, Stiehler M, Baatrup A, Li H, Zou X, Flyvbjerg A, et al. Mesenchymal stem cell ingrowth and differentiation on coralline hydroxyapatite scaffolds. Biomaterials. **28**, 1036, 2007.
223. Grayson WL, Frohlich M, Yeager K, Bhumiratana S, Chan ME, Cannizzaro C, et al. Engineering anatomically shaped human bone grafts. Proc. Natl. Acad. Sci. **107**, 3299, 2010.
224. Janssen FW, van Dijkhuizen-Radersma R, Van Oorschot A, Oostra J, de Bruijn JD, and Van Blitterswijk CA. Human tissue-engineered bone produced in clinically relevant amounts using a semi-automated perfusion bioreactor system: a preliminary study. J. Tissue Eng. Regen. Med. **4**, n/a, 2009.
225. Sikavitsas VI, Bancroft GN, Holtorf HL, Jansen JA, and Mikos AG. Mineralized matrix deposition by marrow stromal osteoblasts in 3D perfusion culture increases with increasing fluid shear forces. Proc. Natl. Acad. Sci. **100**, 14683, 2003.
226. Datta N, Pham QP, Sharma U, Sikavitsas VI, Jansen JA, and Mikos AG. In vitro generated extracellular matrix and fluid shear stress synergistically enhance 3D osteoblastic differentiation. Proc. Natl. Acad. Sci. **103**, 2488, 2006.
227. Sikavitsas VI, Bancroft GN, Lemoine JJ, Liebschner MAK, Dauner M, and Mikos AG. Flow perfusion enhances the calcified matrix deposition of marrow stromal cells in biodegradable nonwoven fiber mesh scaffolds. Ann. Biomed. Eng. **33**, 63, 2005.
228. Bancroft GN, Sikavitsas VI, van den Dolder J, Sheffield TL, Ambrose CG, Jansen JA, et al. Fluid flow increases mineralized matrix deposition in 3D perfusion culture of marrow stromal osteoblasts in a dose-dependent manner. Proc. Natl. Acad. Sci. **99**, 12600, 2002.
229. Gerecht-Nir S, Cohen S, and Itskovitz-Eldor J. Bioreactor cultivation enhances the efficiency of human embryoid body (hEB) formation and differentiation. Biotechnol. Bioeng. **86**, 493, 2004.

230. Yeatts AB, Geibel EM, Fears FF, and Fisher JP. Human mesenchymal stem cell position within scaffolds influences cell fate during dynamic culture. Biotechnol. Bioeng. **109**, 2381, 2012.
231. Ferlin KM, Prendergast ME, Miller ML, Kaplan DS, and Fisher JP. Influence of 3D printed porous architecture on mesenchymal stem cell enrichment and differentiation. Acta Biomater. Acta Materialia Inc.; **32**, 161, 2016.
232. Qian X, Nguyen HN, Song MM, Hadiono C, Ogden SC, Hammack C, et al. Brain-Region-Specific Organoids Using Mini-bioreactors for Modeling ZIKV Exposure. Cell. **165**, 1238, 2016.
233. El-Ali J, Sorger PK, and Jensen KF. Cells on chips. Nature. **442**, 403, 2006.
234. Amin R, Knowlton S, Hart A, Yenilmez B, Ghaderinezhad F, Katebifar S, et al. 3D-printed microfluidic devices. Biofabrication. IOP Publishing; **8**, 022001, 2016.
235. Alessandri K, Feyeux M, Gurchenkov B, Delgado C, Trushko A, Krause K-H, et al. A 3D printed microfluidic device for production of functionalized hydrogel microcapsules for culture and differentiation of human Neuronal Stem Cells (hNSC). Lab Chip. **16**, 1593, 2016.
236. Morgan AJL, Hidalgo San Jose L, Jamieson WD, Wymant JM, Song B, Stephens P, et al. Simple and Versatile 3D Printed Microfluidics Using Fused Filament Fabrication. Wu M-H, editor. PLoS One. **11**, e0152023, 2016.
237. Knowlton S, Yu CH, Ersoy F, Emadi S, Khademhosseini A, and Tasoglu S. 3D-printed microfluidic chips with patterned, cell-laden hydrogel constructs. Biofabrication. **8**, 025019, 2016.
238. Ong LJY, Islam A, Dasgupta R, Iyer NG, Leo HL, and Toh YC. A 3D printed microfluidic perfusion device for multicellular spheroid cultures. Biofabrication. **9**, 2017.
239. Lin H, Lozito TP, Alexander PG, Gottardi R, and Tuan RS. Stem cell-based microphysiological osteochondral system to model tissue response to interleukin-1B. Mol. Pharm. **11**, 2203, 2014.
240. Stampfl J, Baudis S, Heller C, Liska R, Neumeister A, Kling R, et al. Photopolymers with tunable mechanical properties processed by laser-based high-resolution stereolithography. J. Micromechanics Microengineering. **18**, 125014, 2008.
241. Weiß T, Hildebrand G, Schade R, and Liefeith K. Two-photon polymerization for microfabrication of three-dimensional scaffolds for tissue engineering application. Eng. Life Sci. **9**, 384, 2009.
242. Costello CM, Phillipsen MB, Hartmanis LM, Kwasnica MA, Chen V, Hackam D, et al. Microscale Bioreactors for in situ characterization of GI epithelial cell physiology. Sci. Rep. **7**, 12515, 2017.
243. Kuo CY, Eranki A, Placone JK, Rhodes KR, Aranda-Espinoza H, Fernandes R, et al. Development of a 3D Printed, Bioengineered Placenta Model to Evaluate the Role of Trophoblast Migration in Preeclampsia. ACS Biomater. Sci. Eng. **2**, 1817, 2016.
244. Mota C, Danti S, D'Alessandro D, Trombi L, Ricci C, Puppi D, et al. Multiscale fabrication of biomimetic scaffolds for tympanic membrane tissue engineering. Biofabrication. **7**, 2015.
245. Balakrishnan S, Suma MS, Raju SR, Bhargav SDB, Arunima S, Das S, et al. A Scalable Perfusion Culture System with Miniature Peristaltic Pumps for Live-Cell Imaging Assays with Provision for Microfabricated Scaffolds. Biores. Open Access. **4**, 343, 2015.
246. Alessandri K, Andrique L, Feyeux M, Bikfalvi A, Nassoy P, and Recher G. All-in-one 3D printed microscopy chamber for multidimensional imaging, the UniverSlide. Sci. Rep. **7**, 42378, 2017.
247. Tang Q, Piard C, Lin J, Nan K, Guo T, Caccamese J, et al. Imaging stem cell distribution, growth, migration, and differentiation in 3-D scaffolds for bone tissue engineering using

mesoscopic fluorescence tomography. Biotechnol. Bioeng. 257, 2017.
248. Yi H-G, Lee H, and Cho D-W. 3D Printing of Organs-On-Chips. Bioengineering. **4**, 10, 2017.
249. Bhatia SN, and Ingber DE. Microfluidic organs-on-chips. Nat. Biotechnol. Nature Publishing Group; **32**, 760, 2014.
250. Ronaldson-Bouchard K, and Vunjak-Novakovic G. Organs-on-a-Chip: A Fast Track for Engineered Human Tissues in Drug Development. Cell Stem Cell. Cell Press; **22**, 310, 2018.
251. Meer AD van der, and Berg A van den. Organs-on-chips: breaking the in vitro impasse. Integr. Biol. **4**, 461, 2012.
252. Huh D, Hamilton GA, and Ingber DE. From 3D cell culture to organs-on-chips. Trends Cell Biol. **21**, 745, 2011.
253. Hao S, Ha L, Cheng G, Wan Y, Xia Y, Sosnoski DM, et al. A Spontaneous 3D Bone-On-a-Chip for Bone Metastasis Study of Breast Cancer Cells. Small. **14**, 1702787, 2018.
254. Grix T, Ruppelt A, Thomas A, Amler A-K, Noichl B, Lauster R, et al. Bioprinting Perfusion-Enabled Liver Equivalents for Advanced Organ-on-a-Chip Applications. Genes. **9**, 176, 2018.
255. Costa PF, Albers HJ, Linssen JEA, Middelkamp HHT, van der Hout L, Passier R, et al. Mimicking arterial thrombosis in a 3D-printed microfluidic in vitro vascular model based on computed tomography angiography data. Lab Chip. Royal Society of Chemistry; **17**, 2785, 2017.
256. Singh M, Tong Y, Webster K, Cesewski E, Haring AP, Laheri S, et al. 3D printed conformal microfluidics for isolation and profiling of biomarkers from whole organs. Lab Chip. Royal Society of Chemistry; **17**, 2561, 2017.
257. Li X, Brooks JC, Hu J, Ford KI, and Easley CJ. 3D-templated, fully automated microfluidic input/output multiplexer for endocrine tissue culture and secretion sampling. Lab Chip. Royal Society of Chemistry; **17**, 341, 2017.
258. Cooke MN, Fisher JP, Dean D, Rimnac C, and Mikos AG. Use of stereolithography to manufacture critical-sized 3D biodegradable scaffolds for bone ingrowth. J. Biomed. Mater. Res. **64B**, 65, 2003.
259. Seitz H, Rieder W, Irsen S, Leukers B, and Tille C. Three-dimensional printing of porous ceramic scaffolds for bone tissue engineering. J. Biomed. Mater. Res. - Part B Appl. Biomater. **74**, 782, 2005.
260. Habibovic P, Gbureck U, Doillon CJ, Bassett DC, van Blitterswijk CA, and Barralet JE. Osteoconduction and osteoinduction of low-temperature 3D printed bioceramic implants. Biomaterials. **29**, 944, 2008.
261. Zhang S, Cheng X, Yao Y, Wei Y, Han C, Shi Y, et al. Porous niobium coatings fabricated with selective laser melting on titanium substrates: Preparation, characterization, and cell behavior. Mater. Sci. Eng. C. **53**, 50, 2015.
262. Roskies M, Jordan JO, Fang D, Abdallah MN, Hier MP, Mlynarek A, et al. Improving PEEK bioactivity for craniofacial reconstruction using a 3D printed scaffold embedded with mesenchymal stem cells. J. Biomater. Appl. **31**, 132, 2016.
263. Khalyfa A, Vogt S, Weisser J, Grimm G, Rechtenbach A, Meyer W, et al. Development of a new calcium phosphate powder-binder system for the 3D printing of patient specific implants. J. Mater. Sci. Mater. Med. **18**, 909, 2007.
264. Sa M-W, Nguyen B-NB, Moriarty RA, Kamalitdinov T, Fisher JP, and Kim JY. Fabrication and evaluation of 3D printed BCP scaffolds reinforced with ZrO 2 for bone tissue applications. Biotechnol. Bioeng. **115**, 989, 2018.
265. Shim J-H, Yoon M-C, Jeong C-M, Jang J, Jeong S-I, Cho D-W, et al. Efficacy of rhBMP-2 loaded PCL/PLGA/ β -TCP guided bone regeneration membrane fabricated by 3D

printing technology for reconstruction of calvaria defects in rabbit. Biomed. Mater. **9**, 065006, 2014.
266. Esposito Corcione C, Gervaso F, Scalera F, Montagna F, Maiullaro T, Sannino A, et al. 3D printing of hydroxyapatite polymer-based composites for bone tissue engineering. J. Polym. Eng. **37**, 741, 2017.
267. Liu A, Xue G, Sun M, Shao H, Ma C, Gao Q, et al. 3D Printing Surgical Implants at the clinic: A Experimental Study on Anterior Cruciate Ligament Reconstruction. Sci. Rep. **6**, 21704, 2016.
268. Kao CT, Lin CC, Chen YW, Yeh CH, Fang HY, and Shie MY. Poly(dopamine) coating of 3D printed poly(lactic acid) scaffolds for bone tissue engineering. Mater. Sci. Eng. C. Elsevier B.V.; **56**, 165, 2015.
269. Mozdzen LC, Rodgers R, Banks JM, Bailey RC, and Harley BAC. Increasing the strength and bioactivity of collagen scaffolds using customizable arrays of 3D-printed polymer fibers. Acta Biomater. **33**, 25, 2016.
270. Araujo Borges R, Choudhury D, and Zou M. 3D printed PCU/UHMWPE polymeric blend for artificial knee meniscus. Tribol. Int. **122**, 1, 2018.
271. Trachtenberg JE, Placone JK, Smith BT, Fisher JP, and Mikos AG. Extrusion-based 3D printing of poly(propylene fumarate) scaffolds with hydroxyapatite gradients. J. Biomater. Sci. Polym. Ed. **28**, 532, 2017.
272. Guo T, Ringel JP, Lim CG, Bracaglia LG, Noshin M, Baker HB, et al. Three dimensional extrusion printing induces polymer molecule alignment and cell organization within engineered cartilage. J. Biomed. Mater. Res. Part A. **106**, 2190, 2018.
273. Steffen A, Klaiber S, Katzbach R, Nitsch S, Koing I, and Frenzel H. The Psychosocial Consequences of Reconstruction of Severe Ear Defects or Third-Degree Microtia With Rib Cartilage. Aesthetic Surg. J. **28**, 404, 2008.
274. Silva DN, Gerhardt de Oliveira M, Meurer E, Meurer MI, Lopes da Silva JV, and Santa-Bárbara A. Dimensional error in selective laser sintering and 3D-printing of models for craniomaxillary anatomy reconstruction. J. Cranio-Maxillofacial Surg. **36**, 443, 2008.
275. Chen J, Zhang Z, Chen X, Zhang C, Zhang G, and Xu Z. Design and manufacture of customized dental implants by using reverse engineering and selective laser melting technology. J. Prosthet. Dent. **112**, 1088, 2014.
276. Wiria FE, Shyan JYM, Lim PN, Wen FGC, Yeo JF, and Cao T. Printing of Titanium implant prototype. Mater. Des. **31**, S101, 2010.
277. Monaco C, Evangelisti E, Scotti R, Mignani G, and Zucchelli G. A fully digital approach to replicate peri-implant soft tissue contours and emergence profile in the esthetic zone. Clin. Oral Implants Res. **27**, 1511, 2016.
278. Tamimi F, Torres J, Al-Abedalla K, Lopez-Cabarcos E, Alkhraisat MH, Bassett DC, et al. Osseointegration of dental implants in 3D-printed synthetic onlay grafts customized according to bone metabolic activity in recipient site. Biomaterials. **35**, 5436, 2014.
279. Msallem B, Beiglboeck F, Honigmann P, Jaquiéry C, and Thieringer F. Craniofacial Reconstruction by a Cost-Efficient Template-Based Process Using 3D Printing. Plast. Reconstr. Surg. - Glob. Open. **5**, e1582, 2017.
280. Cohen A, Laviv A, Berman P, Nashef R, and Abu-Tair J. Mandibular reconstruction using stereolithographic 3-dimensional printing modeling technology. Oral Surgery, Oral Med. Oral Pathol. Oral Radiol. Endodontology. **108**, 661, 2009.
281. Shao H, Sun M, Zhang F, Liu A, He Y, Fu J, et al. Custom Repair of Mandibular Bone Defects with 3D Printed Bioceramic Scaffolds. J. Dent. Res. **97**, 68, 2018.
282. Ackland DC, Robinson D, Redhead M, Lee PVS, Moskaljuk A, and Dimitroulis G. A personalized 3D-printed prosthetic joint replacement for the human temporomandibular joint: From implant design to implantation. J. Mech. Behav. Biomed. Mater. **69**, 404,

2017.
283. Sumida T, Otawa N, Kamata Y, Kamakura S, Mtsushita T, Kitagaki H, et al. Custom-made titanium devices as membranes for bone augmentation in implant treatment: Clinical application and the comparison with conventional titanium mesh. J. Cranio-Maxillofacial Surg. **43**, 2183, 2015.
284. Ang TH, Sultana FSA, Hutmacher DW, Wong YS, Fuh JYH, Mo XM, et al. Fabrication of 3D chitosan-hydroxyapatite scaffolds using a robotic dispensing system. Mater. Sci. Eng. C. **20**, 35, 2002.
285. He Y, Xue G, and Fu J. Fabrication of low cost soft tissue prostheses with the desktop 3D printer. Sci. Rep. **4**, 6973, 2015.
286. Lee JS, Hong JM, Jung JW, Shim JH, Oh JH, and Cho DW. 3D printing of composite tissue with complex shape applied to ear regeneration. Biofabrication. **6**, 2014.
287. Zopf DA, Mitsak AG, Flanagan CL, Wheeler M, Green GE, and Hollister SJ. Computer Aided–Designed, 3-Dimensionally Printed Porous Tissue Bioscaffolds for Craniofacial Soft Tissue Reconstruction. Otolaryngol. Neck Surg. **152**, 57, 2015.
288. Rodriguez MJ, Brown J, Giordano J, Lin SJ, Omenetto FG, and Kaplan DL. Silk based bioinks for soft tissue reconstruction using 3-dimensional (3D) printing with in vitro and in vivo assessments. Biomaterials. **117**, 105, 2017.
289. Placone JK, Navarro J, Laslo GW, Lerman MJ, Gabard AR, Herendeen GJ, et al. Development and Characterization of a 3D Printed, Keratin-Based Hydrogel. Ann. Biomed. Eng. **45**, 1, 2016.
290. Kuo C-Y, Wilson E, Fuson A, Gandhi N, Monfaredi R, Jenkins A, et al. Repair of Tympanic Membrane Perforations with Customized Bioprinted Ear Grafts Using Chinchilla Models. Tissue Eng. Part A. **24**, 527, 2018.
291. Hong S, Sycks D, Chan HF a., Lin S, Lopez GP, Guilak F, et al. 3D Printing: 3D Printing of Highly Stretchable and Tough Hydrogels into Complex, Cellularized Structures. Adv. Mater. **27**, 4034, 2015.
292. Highley CB, Rodell CB, and Burdick JA. Direct 3D Printing of Shear-Thinning Hydrogels into Self-Healing Hydrogels. Adv. Mater. **27**, 5075, 2015.
293. Miller JS, Stevens KR, Yang MT, Baker BM, Nguyen DHT, Cohen DM, et al. Rapid casting of patterned vascular networks for perfusable engineered three-dimensional tissues. Nat. Mater. **11**, 768, 2012.
294. Kolesky DB, Truby RL, Gladman AS, Busbee TA, Homan KA, and Lewis JA. 3D bioprinting of vascularized, heterogeneous cell-laden tissue constructs. Adv. Mater. **26**, 3124, 2014.
295. Lee VK, Kim DY, Ngo H, Lee Y, Seo L, Yoo SS, et al. Creating perfused functional vascular channels using 3D bio-printing technology. Biomaterials. **35**, 8092, 2014.
296. Lee VK, Lanzi AM, Ngo H, Yoo SS, Vincent PA, and Dai G. Generation of multi-scale vascular network system within 3D hydrogel using 3D bio-printing technology. Cell. Mol. Bioeng. **7**, 460, 2014.
297. Jia W, Gungor-Ozkerim PS, Zhang YS, Yue K, Zhu K, Liu W, et al. Direct 3D bioprinting of perfusable vascular constructs using a blend bioink. Biomaterials. **106**, 58, 2016.
298. National Center for Health Statistics. Health, United States, 2016: With Chartbook on Long-term Trends in Health. Trends Heal. Hyattsville, MD; 2017.
299. Bracaglia LG, Messina M, Winston S, Kuo CY, Lerman M, and Fisher JP. 3D Printed Pericardium Hydrogels to Promote Wound Healing in Vascular Applications. Biomacromolecules. **18**, 3802, 2017.
300. Hockaday LA, Kang KH, Colangelo NW, Cheung PYC, Duan B, Malone E, et al. Rapid 3D printing of anatomically accurate and mechanically heterogeneous aortic valve hydrogel scaffolds. Biofabrication. **4**, 2012.

301. Melchiorri AJ, Hibino N, Best CA, Yi T, Lee YU, Kraynak CA, et al. 3D-Printed Biodegradable Polymeric Vascular Grafts. Adv. Healthc. Mater. **5**, 319, 2016.
302. L'Heureux N, McAllister TN, and de la Fuente LM. Tissue-Engineered Blood Vessel for Adult Arterial Revascularization. N. Engl. J. Med. **357**, 1451, 2007.
303. Schmidt CE, and Baier JM. Acellular vascular tissues: natural biomaterials for tissue repair and tissue engineering. Biomaterials. **21**, 2215, 2000.
304. Schierholz JM, and Beuth J. Implant infections: A haven for opportunistic bacteria. J. Hosp. Infect. **49**, 87, 2001.
305. Benrashid E, McCoy CC, Youngwirth LM, Kim J, Manson RJ, Otto JC, et al. Tissue engineered vascular grafts: Origins, development, and current strategies for clinical application. Methods. **99**, 13, 2016.
306. Anderson PA. Clinical Applications of 3D Printing. Spine (Phila. Pa. 1976). **42**, S30, 2017.
307. Mcmenamin PG, Quayle MR, Mchenry CR, and Adams JW. The production of anatomical teaching resources using three-dimensional (3D) printing technology. Anat. Sci. Educ. **7**, 479, 2014.
308. Tam MDBS, Laycock SD, Brown JRI, and Jakeways M. 3D Printing of an Aortic Aneurysm to Facilitate Decision Making and Device Selection for Endovascular Aneurysm Repair in Complex Neck Anatomy. J. Endovasc. Ther. **20**, 863, 2013.
309. Weinstock P, Prabhu SP, Flynn K, Orbach DB, and Smith E. Optimizing cerebrovascular surgical and endovascular procedures in children via personalized 3D printing. J. Neurosurg. Pediatr. **16**, 584, 2015.
310. Mobbs RJ, Coughlan M, Thompson R, Iii CES, and Phan K. Pathologies : Case Report. **26**, 513, 2017.
311. Kruse ALD, Luebbers HT, Grätz KW, and Obwegeser J a. Factors influencing survival of free-flap in reconstruction for cancer of the head and neck: a literature review. Microsurgery. **30**, 242, 2010.
312. Ebert LC, Thali MJ, and Ross S. Getting in touch-3D printing in Forensic Imaging. Forensic Sci. Int. **211**, 1, 2011.
313. Di Prima M, Coburn J, Hwang D, Kelly J, Khairuzzaman A, and Ricles L. Additively manufactured medical products – the FDA perspective. 3D Print. Med. 3D Printing in Medicine; **2**, 1, 2015.
314. Coburn JC, and Grant GT. 3D Printing in Medicine. Et al.: Rybicki FJ, Grant GT, editors. 3D Print. Med. A Pract. Guid. Med. Prof. Cham: Springer International Publishing; 97–111, 2017.
315. Rankin TM, Giovinco NA, Cucher DJ, Watts G, Hurwitz B, and Armstrong DG. Three-dimensional printing surgical instruments: Are we there yet? J. Surg. Res. Elsevier Inc; **189**, 193, 2014.
316. Soares da Costa D, Márquez-Posadas M del C, Araujo AR, Yang Y, Merino S, Groth T, et al. Adhesion of Adipose-Derived Mesenchymal Stem Cells to Glycosaminoglycan Surfaces with Different Protein Patterns. ACS Appl. Mater. Interfaces. **7**, 10034, 2015.
317. Shukla A, Slater JH, Culver JC, Dickinson ME, and West JL. Biomimetic Surface Patterning Promotes Mesenchymal Stem Cell Differentiation. ACS Appl. Mater. Interfaces. **8**, 21883, 2016.
318. Kumar A, Lau W, and Starly B. Human Mesenchymal Stem Cells Expansion on Three-Dimensional (3D) Printed Poly-Styrene (PS) Scaffolds in a Perfusion Bioreactor. Procedia CIRP. **65**, 115, 2017.
319. Curran JM, Chen R, and Hunt JA. The guidance of human mesenchymal stem cell differentiation in vitro by controlled modifications to the cell substrate. Biomaterials. **27**, 4783, 2006.

320. Keselowsky BG, Collard DM, and García AJ. Surface chemistry modulates fibronectin conformation and directs integrin binding and specificity to control cell adhesion. J. Biomed. Mater. Res. Part A. **66A**, 247, 2003.
321. Xu LC, and Siedlecki CA. Effects of surface wettability and contact time on protein adhesion to biomaterial surfaces. Biomaterials. **28**, 3273, 2007.
322. McFarland CD, Thomas CH, DeFilippis C, Steele JG, and Healy KE. Protein adsorption and cell attachment to patterned surfaces. J. Biomed. Mater. Res. **49**, 200, 2000.
323. Ostuni E, Chen CS, Ingber DE, and Whitesides GM. Selective Deposition of Proteins and Cells in Arrays of Microwells. Langmuir. **17**, 2828, 2001.
324. Richter B, Hahn V, Bertels S, Claus TK, Wegener M, Delaittre G, et al. Guiding Cell Attachment in 3D Microscaffolds Selectively Functionalized with Two Distinct Adhesion Proteins. Adv. Mater. **29**, 1, 2017.
325. Kuo C-Y, Guo T, Cabrera-Luque J, Arumugasaamy N, Bracaglia L, Garcia-Vivas A, et al. Placental basement membrane proteins are required for effective cytotrophoblast invasion in a three-dimensional bioprinted placenta model. J. Biomed. Mater. Res. Part A. **106**, 1476, 2018.
326. Cox J, and Mann M. MaxQuant enables high peptide identification rates, individualized p.p.b.-range mass accuracies and proteome-wide protein quantification. Nat. Biotechnol. **26**, 1367, 2008.
327. Resutek L, and Hsieh AH. The vacuolated morphology of chordoma cells is dependent on cytokeratin intermediate filaments. J. Cell. Physiol. **234**, 3458, 2019.
328. Goddette DW, and Frieden C. Actin polymerization. The mechanism of action of cytochalasin D. J. Biol. Chem. **261**, 15974, 1986.
329. Casella JF, Flanagan MD, and Lin S. Cytochalasin D inhibits actin polymerization and induces depolymerization of actin filaments formed during platelet shape change. Nature. **293**, 302, 1981.
330. Drygiannakis AI, Papathanasiou AG, and Boudouvis AG. On the connection between dielectric breakdown strength, trapping of charge, and contact angle saturation in electrowetting. Langmuir. **25**, 147, 2009.
331. Digilov R. Charge-induced modification of contact angle: The secondary electrocapillary effect. Langmuir. **16**, 6719, 2000.
332. Baujard-Lamotte L, Noinville S, Goubard F, Marque P, and Pauthe E. Kinetics of conformational changes of fibronectin adsorbed onto model surfaces. Colloids Surfaces B Biointerfaces. **63**, 129, 2008.
333. Stern J, Weil-Malherbe H, and Green RH. The effects and the fate of malononitrile and related compounds in animals tissues. Biochem. J. **52**, 114, 1952.
334. Tidwell CD, Castner DG, Golledge SL, Ratner BD, Meyer K, Hagenhoff B, et al. Static time-of-flight secondary ion mass spectrometry and x-ray photoelectron spectroscopy characterization of adsorbed albumin and fibronectin films. Surf. Interface Anal. **31**, 724, 2001.
335. Ho Y-C, Huang F-M, and Chang Y-C. Cytotoxicity of formaldehyde on human osteoblastic cells is related to intracellular glutathione levels. J. Biomed. Mater. Res. Part B Appl. Biomater. **83B**, 340, 2007.
336. Vroman L, Adams AL, Fischer GC, and Munoz PC. Interaction of high molecular weight kininogen, factor XII, and fibrinogen in plasma at interfaces. Blood. **55**, 156, 1980.
337. Liu W, Zhan J, Su Y, Wu T, Wu C, Ramakrishna S, et al. Effects of plasma treatment to nanofibers on initial cell adhesion and cell morphology. Colloids Surfaces B Biointerfaces. **113**, 101, 2014.
338. Athanassiou G, and Deligianni D. Adhesion strength of individual human bone marrow cells to fibronectin. Integrin beta1-mediated adhesion. J. Mater. Sci. Mater. Med. **12**, 965,

2001.
339. Hirsh SL, McKenzie DR, Nosworthy NJ, Denman JA, Sezerman OU, and Bilek MMM. The Vroman effect: Competitive protein exchange with dynamic multilayer protein aggregates. Colloids Surfaces B Biointerfaces. Elsevier B.V.; **103**, 395, 2013.
340. Latour R. Biomaterials: Protein–Surface Interactions. Et al.: Wnek GE, Bowlin GL, editors. Encycl. Biomater. Biomed. Eng. Second Ed. - Four Vol. Set. 2. CRC Press; 270–84, 2005.
341. Ruoslahti E, and Pierschbacher MD. New perspectives in cell adhesion: RGD and integrins. Science. **238**, 491, 1987.
342. Salasznyk RM, Williams WA, Boskey A, Batorsky A, and Plopper GE. Adhesion to vitronectin and collagen I promotes osteogenic differentiation of human mesenchymal stem cells. J. Biomed. Biotechnol. **1**, 24, 2004.
343. Linsley C, Wu B, and Tawil B. The Effect of Fibrinogen, Collagen Type I, and Fibronectin on Mesenchymal Stem Cell Growth and Differentiation into Osteoblasts. Tissue Eng. Part A. **19**, 1416, 2013.
344. Li B, Moshfegh C, Lin Z, Albuschies J, and Vogel V. Mesenchymal stem cells exploit extracellular matrix as mechanotransducer. Sci. Rep. **3**, 1, 2013.
345. Tsai K-S, Kao S-Y, Wang C-Y, Wang Y-J, Wang J-P, and Hung S-C. Type I collagen promotes proliferation and osteogenesis of human mesenchymal stem cells via activation of ERK and Akt pathways. J. Biomed. Mater. Res. Part A. **94A**, 673, 2010.
346. Asakura S, Hurley RW, Skorstengaard K, Ohkubo I, and Mosher DF. Inhibition of cell adhesion by high molecular weight kininogen. J Cell Biol. **116**, 465, 1992.
347. Stannard AK, Riddell DR, Sacre SM, Tagalakis AD, Langer C, Von Eckardstein A, et al. Cell-derived Apolipoprotein E (ApoE) Particles Inhibit Vascular Cell Adhesion Molecule-1 (VCAM-1) Expression in Human Endothelial Cells. J. Biol. Chem. **276**, 46011, 2001.
348. Bost F, Diarra-Mehrpour M, and Martin JP. Inter-alpha-trypsin inhibitor proteoglycan family--a group of proteins binding and stabilizing the extracellular matrix. Eur. J. Biochem. **252**, 339, 1998.
349. Ocklind C, Forsum U, and Obrink B. Cell surface localization and tissue distribution of a hepatocyte cell-cell adhesion glycoprotein (cell-CAM 105). J. Cell Biol. **96**, 1168, 1983.
350. Eidelman S, Damsky CH, Wheelock MJ, and Damjanov I. Expression of the cell-cell adhesion glycoprotein cell-CAM 120/80 in normal human tissues and tumors. Am. J. Pathol. **135**, 101, 1989.
351. Zoellner H, Höfler M, Beckmann R, Hufnagl P, Vanyek E, Bielek E, et al. Serum albumin is a specific inhibitor of apoptosis in human endothelial cells. J. Cell Sci. **109**, 2571, 1996.
352. Law RHP, Zhang Q, McGowan S, Buckle AM, Silverman GA, Wong W, et al. An overview of the serpin superfamily. Genome Biol. **7**, 1, 2006.
353. Borth W. Alpha 2-macroglobulin, a multifunctional binding protein with targeting characteristics. FASEB J. **6**, 3345, 1992.
354. Sallenave JMJ-M. Antimicrobial activity of antiproteinases. Biochem. Soc. Trans. Portland Press Limited; **30**, 111, 2002.
355. Castellano AC, Barteri M, Castagnola M, Bianconi A, Borghi E, and Dellalonga S. Structure-Function Relationship in the Serotransferrin: The Role of the pH on the Conformational Change and the Metal Ions Release. Biochem. Biophys. Res. Commun. **198**, 646, 1994.
356. White P, and Cooke N. The multifunctional properties and characteristics of vitamin D-binding protein. Trends Endocrinol. Metab. **11**, 320, 2000.
357. Pappano AJ, and Gil Wier W. Overview of the Circulation and Blood. Cardiovasc. Physiol. 10th. Philadelphia: Elisevier, Inc.; 1–9, 2013.
358. Mizejewski GJ. Alpha-fetoprotein structure and function: relevance to isoforms, epitopes,

and conformational variants. Exp. Biol. Med. **226**, 377, 2001.
359. Lee MH, Ducheyne P, Lynch L, Boettiger D, and Composto RJ. Effect of biomaterial surface properties on fibronectin- α5β1integrin interaction and cellular attachment. Biomaterials. **27**, 1907, 2006.
360. Lestelius M, Liedberg B, and Tengvall P. In Vitro Plasma Protein Adsorption on ω-Functionalized Alkanethiolate Self-Assembled Monolayers. Langmuir. **13**, 5900, 1997.
361. Xu Z, and Grassian VH. Bovine Serum Albumin Adsorption on TiO_2 Nanoparticle Surfaces: Effects of pH and Coadsorption of Phosphate on Protein–Surface Interactions and Protein Structure. J. Phys. Chem. C. **121**, 21763, 2017.
362. Anselme K, Ploux L, and Ponche A. Cell/Material Interfaces: Influence of Surface Chemistry and Surface Topography on Cell Adhesion. J. Adhes. Sci. Technol. **24**, 831, 2010.
363. Krampera M, Galipeau J, Shi Y, Tarte K, and Sensebe L. Immunological characterization of multipotent mesenchymal stromal cells—The International Society for Cellular Therapy (ISCT) working proposal. Cytotherapy. **15**, 1054, 2013.
364. Silva WA, Covas DT, Panepucci RA, Proto-Siqueira R, Siufi JLC, Zanette DL, et al. The profile of gene expression of human marrow mesenchymal stem cells. Stem Cells. **21**, 661, 2003.
365. Veevers-Lowe J, Ball SG, Shuttleworth A, and Kielty CM. Mesenchymal stem cell migration is regulated by fibronectin through a5 b1-integrin-mediated activation of PDGFR- and potentiation of growth factor signals. J. Cell Sci. **124**, 1288, 2011.
366. Olivares-Navarrete R, Rodil SE, Hyzy SL, Dunn GR, Almaguer-Flores A, Schwartz Z, et al. Role of integrin subunits in mesenchymal stem cell differentiation and osteoblast maturation on graphitic carbon-coated microstructured surfaces. Biomaterials. **51**, 69, 2015.
367. Mann BK, Tsai AT, Scott-Burden T, and West JL. Modification of surfaces with cell adhesion peptides alters extracellular matrix deposition. Biomaterials. **20**, 2281, 1999.
368. Fox TG, and Flory PJ. Second-order transition temperatures and related properties of polystyrene. I. Influence of molecular weight. J. Appl. Phys. **21**, 581, 1950.
369. Dimarzio EA, and Gibbs JH. Molecular interpretation of glass temperature depression by plasticizers. J. Polym. Sci. Part A Gen. Pap. **1**, 1417, 1963.
370. Lee H, and Archer LA. Functionalizing polymer surfaces by field-induced migration of copolymer additives - Role of shear fields. Polym. Eng. Sci. **42**, 1568, 2002.
371. Mei Y, Saha K, Bogatyrev SR, Yang J, Hook AL, Kalcioglu ZI, et al. Combinatorial development of biomaterials for clonal growth of human pluripotent stem cells. Nat. Mater. Nature Publishing Group; **9**, 768, 2010.
372. Guo L, Kawazoe N, Fan Y, Ito Y, Tanaka J, Tateishi T, et al. Chondrogenic differentiation of human mesenchymal stem cells on photoreactive polymer-modified surfaces. Biomaterials. **29**, 23, 2008.
373. Griffin MF, Ibrahim A, Seifalian AM, Butler PEM, Kalaskar DM, and Ferretti P. Chemical group-dependent plasma polymerisation preferentially directs adipose stem cell differentiation towards osteogenic or chondrogenic lineages. Acta Biomater. **50**, 450, 2017.
374. Phillips JE, Petrie TA, Creighton FP, and García AJ. Human mesenchymal stem cell differentiation on self-assembled monolayers presenting different surface chemistries. Acta Biomater. Acta Materialia Inc.; **6**, 12, 2010.
375. Mwale F, Wang HT, Nelea V, Luo L, Antoniou J, and Wertheimer MR. The effect of glow discharge plasma surface modification of polymers on the osteogenic differentiation of committed human mesenchymal stem cells. Biomaterials. **27**, 2258, 2006.
376. Müller P, Bulnheim U, Diener A, Lüthen F, Teller M, Klinkenberg ED, et al. Calcium

phosphate surfaces promote osteogenic differentiation of mesenchymal stem cells. J. Cell. Mol. Med. **12**, 281, 2008.
377. Guo L, Kawazoe N, Hoshiba T, Tateishi T, Chen G, and Zhang X. Osteogenic differentiation of human mesenchymal stem cells on chargeable polymer-modified surfaces. J. Biomed. Mater. Res. - Part A. **87**, 903, 2008.
378. Benoit DSW, Schwartz MP, Durney AR, and Anseth KS. Small functional groups for controlled differentiation of hydrogel-encapsulated human mesenchymal stem cells. Nat. Mater. **7**, 816, 2008.
379. Lerman MJ, Muramoto S, Arumugasaamy N, Order M Van, Lembong J, Gerald AG, et al. Development of surface functionalization strategies for 3D-printed polystyrene constructs. J. Biomed. Mater. Res. Part B Appl. Biomater. 1, 2019.
380. Diaz-Gomez L, Smith BT, Kontoyiannis PD, Bittner SM, Melchiorri AJ, and Mikos AG. Multimaterial Segmented Fiber Printing for Gradient Tissue Engineering. Tissue Eng. Part C Methods. **25**, 12, 2019.
381. Trachtenberg JE, Placone JK, Smith BT, Piard CM, Santoro M, Scott DW, et al. Extrusion-Based 3D Printing of Poly(propylene fumarate) in a Full-Factorial Design. ACS Biomater. Sci. Eng. **2**, 1771, 2016.
382. Yang Z, Schmitt JF, and Lee EH. Immunohistochemical Analysis of Human Mesenchymal Stem Cells Differentiating into Chondrogenic, Osteogenic, and Adipogenic Lineages. Methods Mol. Biol. 353–66, 2011.
383. Gregory CA, Grady Gunn W, Peister A, and Prockop DJ. An Alizarin red-based assay of mineralization by adherent cells in culture: comparison with cetylpyridinium chloride extraction. Anal. Biochem. **329**, 77, 2004.
384. Brennan MÁ, Renaud A, Gamblin A, D'Arros C, Nedellec S, Trichet V, et al. 3D cell culture and osteogenic differentiation of human bone marrow stromal cells plated onto jet-sprayed or electrospun micro-fiber scaffolds. Biomed. Mater. **10**, 045019, 2015.
385. Patel DB, Luthers CR, Lerman MJ, Fisher JP, and Jay SM. Enhanced extracellular vesicle production and ethanol-mediated vascularization bioactivity via a 3D-printed scaffold-perfusion bioreactor system. Acta Biomater. Acta Materialia Inc.; 1, 2018.
386. McCoy RJ, and O'Brien FJ. Influence of Shear Stress in Perfusion Bioreactor Cultures for the Development of Three-Dimensional Bone Tissue Constructs: A Review. Tissue Eng. Part B Rev. **16**, 587, 2010.
387. Steele JG, McFarland C, Dalton BA, Johnson G, Evans MD, Howlett CR, et al. Attachment of human bone cells to tissue culture polystyrene and to unmodified polystyrene: the effect of surface chemistry upon initial cell attachment. J. Biomater. Sci. Polym. Ed. **5**, 245, 1993.
388. Sagvolden G, Giaever I, and Feder J. Characteristic Protein Adhesion Forces on Glass and Polystyrene Substrates by Atomic Force Microscopy. Langmuir. **14**, 5984, 1998.
389. Lubarsky G V., Browne MM, Mitchell SA, Davidson MR, and Bradley RH. The influence of electrostatic forces on protein adsorption. Colloids Surfaces B Biointerfaces. **44**, 56, 2005.
390. Ulrich D, Van Rietbergen B, Weinans H, and Rüegsegger P. Finite element analysis of trabecular bone structure: A comparison of image-based meshing techniques. J. Biomech. **31**, 1187, 1998.
391. Boespflug G, Maire M, De Crescenzo G, Lerouge S, and Wertheimer MR. Characterization and comparison of N-, O-, and N+O-functionalized polymer surfaces for efficient (HUVEC) endothelial cell colonization. Plasma Process. Polym. **14**, 1, 2017.
392. Hoshiba T, Yoshikawa C, and Sakakibara K. Characterization of Initial Cell Adhesion on Charged Polymer Substrates in Serum-Containing and Serum-Free Media. Langmuir. **34**, 4043, 2018.

393. Syromotina DS, Surmenev RA, Surmeneva MA, Boyandin AN, Epple M, Ulbricht M, et al. Oxygen and ammonia plasma treatment of poly(3-hydroxybutyrate) films for controlled surface zeta potential and improved cell compatibility. Mater. Lett. Elsevier; **163**, 277, 2016.
394. Finke B, Luethen F, Schroeder K, Mueller PD, Bergemann C, Frant M, et al. The effect of positively charged plasma polymerization on initial osteoblastic focal adhesion on titanium surfaces. Biomaterials. **28**, 4521, 2007.
395. Wilson CJ, Clegg RE, Leavesley DI, and Pearcy MJ. Mediation of Biomaterial–Cell Interactions by Adsorbed Proteins: A Review. Tissue Eng. **11**, 1, 2005.
396. Bergemann C, Quade A, Kunz F, Ofe S, Klinkenberg E-D, Laue M, et al. Ammonia Plasma Functionalized Polycarbonate Surfaces Improve Cell Migration Inside an Artificial 3D Cell Culture Module. Plasma Process. Polym. **9**, 261, 2012.
397. Battiston KG, McBane JE, Labow RS, and Santerre JP. Differences in protein binding and cytokine release from monocytes on commercially sourced tissue culture polystyrene. Acta Biomater. Acta Materialia Inc.; **8**, 89, 2012.
398. Hass R, Kasper C, Böhm S, and Jacobs R. Different populations and sources of human mesenchymal stem cells (MSC): A comparison of adult and neonatal tissue-derived MSC. Cell Commun. Signal. BioMed Central Ltd; **9**, 12, 2011.
399. Kilian K a, Bugarija B, Lahn BT, and Mrksich M. Geometric cues for directing the differentiation of mesenchymal stem cells. Proc. Natl. Acad. Sci. **107**, 4872, 2010.
400. Wysokinski D, Pawlowska E, and Blasiak J. RUNX2: A Master Bone Growth Regulator That May Be Involved in the DNA Damage Response. DNA Cell Biol. **34**, 305, 2015.
401. Galindo M, Pratap J, Young DW, Hovhannisyan H, Im H-J, Choi J-Y, et al. The Bone-specific Expression of Runx2 Oscillates during the Cell Cycle to Support a G 1 -related Antiproliferative Function in Osteoblasts. J. Biol. Chem. **280**, 20274, 2005.
402. Birmingham E, Niebur GL, Mchugh PE, Shaw G, Barry FP, and McNamara LM. Osteogenic differentiation of mesenchymal stem cells is regulated by osteocyte and osteoblast cells in a simplified bone niche. Eur. Cells Mater. **23**, 13, 2012.
403. Park B-W, Kang E-J, Byun J-H, Son M-G, Kim H-J, Hah Y-S, et al. In vitro and in vivo osteogenesis of human mesenchymal stem cells derived from skin, bone marrow and dental follicle tissues. Differentiation. Elsevier; **83**, 249, 2012.
404. Becquart P, Cruel M, Hoc T, Sudre L, Pernelle K, Bizios R, et al. Human mesenchymal stem cell responses to hydrostatic pressure and shear stress. Eur. Cells Mater. **31**, 160, 2016.
405. Magin AS, Körfer NR, Partenheimer H, Lange C, Zander A, and Noll T. Primary Cells as Feeder Cells for Coculture Expansion of Human Hematopoietic Stem Cells from Umbilical Cord Blood—A Comparative Study. Stem Cells Dev. **18**, 173, 2009.
406. Stier S, Ko Y, Forkert R, Lutz C, Neuhaus T, Grünewald E, et al. Osteopontin is a hematopoietic stem cell niche component that negatively regulates stem cell pool size. J. Exp. Med. **201**, 1781, 2005.
407. Majumdar MK, Thiede MA, Haynesworth SE, Bruder SP, and Gerson SL. Human Marrow-Derived Mesenchymal Stem Cells (MSCs) Express Hematopoietic Cytokines and Support Long-Term Hematopoiesis When Differentiated Toward Stromal and Osteogenic Lineages. J. Hematother. Stem Cell Res. **9**, 841, 2000.
408. Vaidya A, and Kale VP. TGF-β signaling and its role in the regulation of hematopoietic stem cells. Syst. Synth. Biol. Springer Netherlands; **9**, 1, 2015.
409. Palsson BO, Paek SH, Schwartz RM, Palsson M, Lee GM, Silver S, et al. Expansion of human bone marrow progenitor cells in a high cell density continuous perfusion system. Biotechnology. **11**, 368, 1993.
410. Schneider U, Schwenk HU, and Bornkamm G. Characterization of EBV-genome negative

"null" and "T" cell lines derived from children with acute lymphoblastic leukemia and leukemic transformed non-Hodgkin lymphoma. Int. J. cancer. **19**, 621, 1977.
411. Seita J, and Weissman IL. Hematopoietic stem cell: Self-renewal versus differentiation. Wiley Interdiscip. Rev. Syst. Biol. Med. **2**, 640, 2010.
412. Reikvam H, Brenner AK, Hagen KM, Liseth K, Skrede S, Hatfield KJ, et al. The cytokine-mediated crosstalk between primary human acute myeloid cells and mesenchymal stem cells alters the local cytokine network and the global gene expression profile of the mesenchymal cells. Stem Cell Res. **15**, 530, 2015.
413. Benvenuto F, Ferrari S, Gerdoni E, Gualandi F, Frassoni F, Pistoia V, et al. Human Mesenchymal Stem Cells Promote Survival of T Cells in a Quiescent State. Stem Cells. **25**, 1753, 2007.
414. Atsuta I, Liu S, Miura Y, Akiyama K, Chen C, An Y, et al. Mesenchymal stem cells inhibit multiple myeloma cells via the Fas/Fas ligand pathway. Stem Cell Res. Ther. **4**, 1, 2013.
415. Ramasamy R, Lam EWF, Soeiro I, Tisato V, Bonnet D, and Dazzi F. Mesenchymal stem cells inhibit proliferation and apoptosis of tumor cells: Impact on in vivo tumor growth. Leukemia. **21**, 304, 2007.
416. Sandstrom CE, Collins PC, McAdams TA, Bender JG, Papoutsakis ET, and Miller WM. Comparison of Whole Serum-Deprived Media for Ex Vivo Expansion of Hematopoietic Progenitor Cells from Cord Blood and Mobilized Peripheral Blood Mononuclear Cells. J. Hematother. **5**, 461, 1996.
417. Laluppa JA, McAdams TA, Papoutsakis ET, and Miller WM. Culture materials affect ex vivo expansion of hematopoietic progenitor cells. J. Biomed. Mater. Res. **36**, 347, 1997.
418. Akiyama K, Chen C, Wang D, Xu X, Qu C, Yamaza T, et al. Mesenchymal-stem-cell-induced immunoregulation involves FAS-ligand-/FAS-mediated T cell apoptosis. Cell Stem Cell. **10**, 544, 2012.
419. Beyth S, Borovsky Z, Mevorach D, Liebergall M, Gazit Z, Aslan H, et al. Human mesenchymal stem cells alter antigen-presenting cell maturation and induce T-cell unresponsiveness. Blood. **105**, 2214, 2005.
420. Di Nicola M, Carlo-Stella C, Magni M, Milanesi M, Longoni PD, Matteucci P, et al. Human bone marrow stromal cells suppress T-lymphocyte proliferation induced by cellular or nonspecific mitogenic stimuli. Blood. **99**, 3838, 2002.
421. Matsumoto K, and Nakamura T. Hepatocyte growth factor: molecular structure, roles in liver regeneration, and other biological functions. Crit. Rev. Oncog. **3**, 27, 1992.
422. Moore KW, Johnson KE, Mosmann TR, Roncarolo MG, Fiorentino DF, Kastelein R, et al. Isolation and expression of human cytokine synthesis inhibitory factor cDNA clones: homology to Epstein-Barr virus open reading frame BCRFI. Proc. Natl. Acad. Sci. **88**, 1172, 2006.
423. Oehm A, Behrmann I, Falk W, Pawlita M, Maier G, Klas C, et al. Purification and molecular cloning of the APO-1 cell surface antigen, a member of the tumor necrosis factor/nerve growth factor receptor superfamily. Sequence identity with the Fas antigen. J. Biol. Chem. **267**, 10709, 1992.
424. Scuderi P, Schneider P, Terskikh A, Bodmer J-L, Mattmann C, Peitsch MC, et al. Characterization of Fas (Apo-1, CD95)-Fas Ligand Interaction. J. Biol. Chem. **272**, 18827, 2002.
425. Rangaswami H, Bulbule A, and Kundu GC. Osteopontin: Role in cell signaling and cancer progression. Trends Cell Biol. **16**, 79, 2006.
426. Richard M-J, Bensa J-C, Favrot M-C, Plumas J, Chaperot L, and Molens J-P. Mesenchymal stem cells induce apoptosis of activated T cells. Leukemia. **19**, 1597, 2005.
427. Ramasamy R, Tong CK, Seow HF, Vidyadaran S, and Dazzi F. The immunosuppressive

effects of human bone marrow-derived mesenchymal stem cells target T cell proliferation but not its effector function. Cell. Immunol. **251**, 131, 2008.
428. Rasmusson I, Ringdén O, Sundberg B, and Le Blanc K. Mesenchymal stem cells inhibit lymphocyte proliferation by mitogens and alloantigens by different mechanisms. Exp. Cell Res. **305**, 33, 2005.
429. Dennis J, Koç ON, Laughlin MJ, Maitra B, Haynesworth SE, Gjini K, et al. Human mesenchymal stem cells support unrelated donor hematopoietic stem cells and suppress T-cell activation. Bone Marrow Transplant. **33**, 597, 2004.
430. Tse WT, Pendleton JD, Beyer WM, Egalka MC, and Guinan EC. Suppression of allogeneic T-cell proliferation by human marrow stromal cells: implications in transplantation. Transplantation. **75**, 389, 2003.
431. Kilroy GE, Foster SJ, Wu X, Ruiz J, Sherwood S, Heifetz A, et al. Cytokine profile of human adipose-derived stem cells: Expression of angiogenic, hematopoietic, and pro-inflammatory factors. J. Cell. Physiol. **212**, 702, 2007.
432. Ostanin AA, Petrovskii YL, Shevela EY, and Chernykh ER. Multiplex Analysis of Cytokines, Chemokines, Growth Factors, MMP-9 and TIMP-1 Produced by Human Bone Marrow, Adipose Tissue, and Placental Mesenchymal Stromal Cells. Bull. Exp. Biol. Med. **151**, 133, 2011.
433. Collins PC, Miller WM, and Papoutsakis ET. Stirred culture of peripheral and cord blood hematopoietic cells offers advantages over traditional static systems for clinically relevant applications. Biotechnol. Bioeng. **59**, 534, 1998.
434. Chittur KK, Mcintire L V., and Rich RR. Shear Stress Effects on Human T Cell Function. Biotechnol. Prog. **4**, 89, 1988.
435. Li M, Chin L-Y, Shukor S, Tamayo A, Maus M V., and Parekkadan B. Closed loop bioreactor system for the ex vivo expansion of human T cells. Cytotherapy. **21**, 76, 2019.
436. Niri NM, Jaberipour M, Razmkhah M, Ghaderi a, and Habibagahi M. Mesenchymal stem cells do not suppress lymphoblastic leukemic cell line proliferation. Iran. J. Immunol. **6**, 186, 2009.
437. Fairfield H, Falank C, Farrell M, Vary C, Boucher JM, Driscoll H, et al. Development of a 3D bone marrow adipose tissue model. Bone. **118**, 77, 2019.
438. Braham MVJ, Minnema MC, Aarts T, Sebestyen Z, Straetemans T, Vyborova A, et al. Cellular immunotherapy on primary multiple myeloma expanded in a 3D bone marrow niche model. Oncoimmunology. **7**, e1434465, 2018.
439. Bianco JER, Rosa RG, Congrains-Castillo A, Joazeiro PP, Waldman SD, Weber JF, et al. Characterization of a novel decellularized bone marrow scaffold as an inductive environment for hematopoietic stem cells. Biomater. Sci. Royal Society of Chemistry; 2019.
440. Campbell NA, Reece JB, Urry LA, Cain ML, Wasserman SA, Minorsky P V., et al. Chapter Five: The Structure and Function of Large Biological Molecules. Biology (Basel). 8th. Pearson; 2008.
441. Li J, Mou X, Qiu J, Wang S, Wang D, Sun D, et al. Surface Charge Regulation of Osteogenic Differentiation of Mesenchymal Stem Cell on Polarized Ferroelectric Crystal Substrate. Adv. Healthc. Mater. **4**, 998, 2015.
442. Sun M, Chi G, Xu J, Tan Y, Xu J, Lv S, et al. Extracellular matrix stiffness controls osteogenic differentiation of mesenchymal stem cells mediated by integrin α5. Stem Cell Res. Ther. Stem Cell Research & Therapy; **9**, 52, 2018.
443. Xu J, Sun M, Tan Y, Wang H, Wang H, Li P, et al. Effect of matrix stiffness on the proliferation and differentiation of umbilical cord mesenchymal stem cells. Differentiation. **96**, 30, 2017.
444. Lubarsky G V., Davidson MR, and Bradley RH. Elastic modulus, oxidation depth and

adhesion force of surface modified polystyrene studied by AFM and XPS. Surf. Sci. **558**, 135, 2004.
445. Zysset PK, Edward Guo X, Edward Hoffler C, Moore KE, and Goldstein SA. Elastic modulus and hardness of cortical and trabecular bone lamellae measured by nanoindentation in the human femur. J. Biomech. **32**, 1005, 1999.
446. Gvaramia D, Müller E, Müller K, Atallah P, Tsurkan M, Freudenberg U, et al. Combined influence of biophysical and biochemical cues on maintenance and proliferation of hematopoietic stem cells. Biomaterials. **138**, 108, 2017.
447. Gribben J, Hamilton A, Mian SA, Passaro D, Abarrategi A, Foster K, et al. Versatile humanized niche model enables study of normal and malignant human hematopoiesis. J. Clin. Invest. **127**, 543, 2017.
448. Wagner JE, Brunstein CG, Boitano AE, DeFor TE, McKenna D, Sumstad D, et al. Phase I/II Trial of StemRegenin-1 Expanded Umbilical Cord Blood Hematopoietic Stem Cells Supports Testing as a Stand-Alone Graft. Cell Stem Cell. Elsevier Inc.; **18**, 144, 2016.
449. Bidan CM, Kommareddy KP, Rumpler M, Kollmannsberger P, Fratzl P, and Dunlop JWC. Geometry as a Factor for Tissue Growth: Towards Shape Optimization of Tissue Engineering Scaffolds. Adv. Healthc. Mater. **2**, 186, 2013.
450. Rouwkema J, Boer J De, and Blitterswijk CA Van. Endothelial Cells Assemble into a 3-Dimensional Prevascular Network in a Bone Tissue Engineering Construct. Tissue Eng. **12**, 2685, 2006.
451. Chi Y, Jin Y, He Z, and Yu T. Detection of cytokines in supernatant from hematopoietic stem/progenitor cells co-cultured with mesenchymal stem cells and endothelial progenitor cells. Cell Tissue Bank. **15**, 397, 2014.
452. Mahadik BP, Bharadwaj NAK, Ewoldt RH, and Harley BAC. Regulating dynamic signaling between hematopoietic stem cells and niche cells via a hydrogel matrix. Biomaterials. **125**, 54, 2017.
453. Leisten I, Kramann R, Ventura Ferreira MS, Bovi M, Neuss S, Ziegler P, et al. 3D co-culture of hematopoietic stem and progenitor cells and mesenchymal stem cells in collagen scaffolds as a model of the hematopoietic niche. Biomaterials. **33**, 1736, 2012.
454. Mahadik BP, Pedron Haba S, Skertich LJ, and Harley BAC. The use of covalently immobilized stem cell factor to selectively affect hematopoietic stem cell activity within a gelatin hydrogel. Biomaterials. **67**, 297, 2015.
455. Kumar S, and Geiger H. HSC Niche Biology and HSC Expansion Ex Vivo. Trends Mol. Med. **23**, 799, 2017.